Dissertation presented to the Instituto Tecnológico de Aeronáutica, in partial fulfillment of the requirements for the degree of Master of Science in the Graduate Program of Physics, Field of Atomic and Molecular Physics.

Daniel Schwalbe Koda

ELECTRONIC PROPERTIES AND BAND ALIGNMENTS OF 2D CRYSTALS AND THEIR VAN DER WAALS HETEROSTRUCTURES

Dissertation approved in its final version by signatories below:

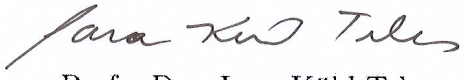

Profa. Dra. Lara Kühl Teles

Advisor

Prof. Dr. Pedro Teixeira Lacava

Dean for Graduate Education and Research

Campo Montenegro
São José dos Campos, SP - Brazil
2017

Cataloging-in Publication Data
Documentation and Information Division

Koda, Daniel Schwalbe
Electronic properties and band alignments of 2D crystals and their van der Waals heterostructures / Daniel Schwalbe Koda.
São José dos Campos, 2017.
119f.

Dissertation of Master of Science – Course of Physics. Area of Atomic and Molecular Physics – Instituto Tecnológico de Aeronáutica, 2017. Advisor: Profa. Dra. Lara Kühl Teles.

1. Grafeno. 2. Semicondutores. 3. Estruturas bidimensionais. 4. Teoria do funcional da densidade. 5. Heteroestruturas de van der Waals. 6. Física. I. Instituto Tecnológico de Aeronáutica. II. Title.

BIBLIOGRAPHIC REFERENCE

KODA, Daniel Schwalbe. **Electronic properties and band alignments of 2D crystals and their van der Waals heterostructures**. 2017. 119f. Dissertation of Master of Science – Instituto Tecnológico de Aeronáutica, São José dos Campos.

CESSION OF RIGHTS

AUTHOR'S NAME: Daniel Schwalbe Koda
PUBLICATION TITLE: Electronic properties and band alignments of 2D crystals and their van der Waals heterostructures.
PUBLICATION KIND/YEAR: Dissertation / 2017

Daniel Schwalbe Koda
R. Prof. Assis Gonçalves, 710, Ap. 34
80.620-250 – Curitiba–PR

ELECTRONIC PROPERTIES AND BAND ALIGNMENTS OF 2D CRYSTALS AND THEIR VAN DER WAALS HETEROSTRUCTURES

Daniel Schwalbe Koda

Thesis Committee Composition:

Prof. Dr.	Homero Santiago Maciel	Chairperson	-	ITA
Profa. Dra.	Lara Kühl Teles	Advisor	-	ITA
Prof. Dr.	Luiz Fernando de Araujo Ferrão	Member	-	ITA
Prof. Dr.	Adalberto Fazzio	External Member	-	USP
Prof. Dr.	Francisco Bolivar Correto Machado	Internal Substitute	-	ITA
Profa. Dra.	Cecília de Carvalho Castro e Silva	External Substitute	-	Mackgraphe

ITA

To my beloved sister, Andréia, for our eternal and unwavering friendship.

Acknowledgments

First of all, I thank my professors for the patience and knowledge. To my advisor, Prof. Lara Kühl Teles, thank you for the precious support, guidance and friendship. To Prof. Marcelo Marques, for the fruitful discussions and zest. To Prof. Friedhelm Bechstedt, for the excellent collaboration and for being such a hardworking inspiration to me. To Prof. Jürgen Furthmüller and Dr. Lars Matthes, for the help with the use of VASP and many scripts.

My journey had also the company of many colleagues and friends. I thank my fellows from the Group of Semiconductor Materials and Nanotechnology, in particular to Ivan Guilhon, Filipe Matusalém, Bruno Lucatto and Antônio Marques, for the nice collaborations and time spent together. I also thank the many friends from ITA, for all the enthusiasm and support in my course.

I also hold in much esteem the opportunity to study at ITA. I acknowledge its Institution, professors and employees in bringing me so far. I offer a special thanks to ITA's Library and everyone who works there, for the encouragement in the last years. Financial support have been provided by CAPES and ITA T-61, and computational resources have been provided by the National Laboratory of Scientific Computing (LNCC/MCTI, Brazil), via the SDumont supercomputer, to whom I am grateful.

Finally, I acknowledge my family and friends for always being with me. To my parents, Carla and Humberto, for all the learning, life and love. To my sister, Andréia, for being my best friend ever. To my grandmother Mitiko, for the phenomenal inspiration you are. To my aunt Denise and my cousin Holly, for the kindness and affection. To my godfather, Antônio, for lending me your ears, eyes and shoulders. To my close friends, thank you for the brightness you bring to my life.

"Sapere aude! Habe Mut, dich deines eigenen Verstandes zu bedienen."
— Immanuel Kant

Resumo

O avanço científico de cristais bidimensionais (2D) como o grafeno e seus análogos levou ao desenvolvimento de um novo paradigma na física do estado sólido. Por meio da combinação de suas propriedades em heteroestruturas de van der Waals, não apenas novas aplicações tecnológicas são possíveis, como também o estudo de fenômenos físicos de interfaces. Propriedades únicas nestes empilhamentos surgem por meio de rotações, pressões, hibridizações e deformações.

Acompanhando a crescente evolução experimental destes sistemas, este trabalho de mestrado baseia-se teoricamente para modelar e simular o contato entre materiais 2D em heteroestruturas verticais por meio do emprego da mecânica quântica e teoria do funcional da densidade. Em primeiro lugar, um método foi desenvolvido para prever e realizar simulações destes empilhamentos 2D, levando em conta a eficiência computacional e a criação de sistemas realísiticos. A técnica, denominada "método das redes coincidentes", apresentou excelente concordância com outros dados teóricos e experimentais. Quando aplicado a um banco de dados de 30 cristais 2D, mais de 700 combinações de baixo custo computacional foram encontradas.

A aplicação do método apresenta uma série de sistemas de interesse para simulações *ab initio*. Os primeiros exemplos apresentados são sistemas com HfS_2, ZrS_2 e MoS_2, cujas estabilidades e propriedades eletrônicas no contato interfacial foram estudadas. Em seguida, rotações foram impostas a bicamadas de hBN/$MoSe_2$ e seus efeitos em propriedades eletrônicas são analisados. Interfaces com fosforeno, $MoSe_2$ e WSe_2 também foram investigadas. Os efeitos da interação de van der Waals sobre as propriedades estruturais e eletrônicas das bicamadas mostraram-se significativos, aumentando o gap do fosforeno e levando a hibridizações entre as camadas. Alinhamentos de bandas e gaps foram modulados por meio do contato, pressão externa e campos elétricos. Finalmente, a validade da regra de Anderson é questionada pela análise detalhada de dez sistemas bicamada. Casos nos quais esta regra falha são analisados, e uma teoria é proposta para explicar estas discrepâncias. Esse trabalho tem importância na investigação de alinhamentos de bandas e fenômenos físicos de interfaces bidimensionais com aplicações em dispositivos eletrônicos e optoeletrônicos.

Abstract

The scientific advance of two-dimensional (2D) crystals such as graphene and its analogous has developed a new paradigm in solid state physics. By combining their properties in van der Waals heterostructures, not only technological applications are possible, but also the study of physical phenomena in 2D interfaces. Unique properties arise in these stackings by rotation, pressure, hybridization and deformations.

Accompanying the growing experiments of these systems, this masters dissertation is theoretically-based to model and simulate the contact of 2D materials in vertical heterostructures by employing quantum mechanics and density functional theory. First of all, a method was developed to predict and perform simulations of 2D stacks, taking into account computational cost and the creation of realistic systems. The technique, named "coincidence lattice method", is in agreement with other theoretical and experimental data. When applied to a database of 30 2D crystals, more than 700 low-computational cost combinations are found.

The application of the method presents a series of interesting systems for *ab initio* simulations. The first examples are systems with HfS_2, ZrS_2 and MoS_2, whose stabilities and electronic properties in the interfacial contact are studied. Then, interlayer twists are imposed to hBN/$MoSe_2$ heterobilayers and their effects in the heterostructure electronic properties are analyzed. Interfaces with phosphorene, $MoSe_2$ and WSe_2 are also investigated. Effects of van der Waals interaction on structural and electronic properties of the bilayers are significant, opening the phosphorene gap and leading to hybridization between layers. Band alignments and gaps are modulated by contact, external pressure and electric field. Finally, the validity of the Anderson rule is questioned by a comprehensive analysis of ten bilayer systems. Cases in which this rule fails are analyzed, and a theory is proposed to explain these discrepancies. This work is important in the investigation of band alignments and physical phenomena in 2D interfaces with applications to electronic and optoelectronic devices.

List of Figures

List of Tables

List of Abbreviations and Acronyms

1BZ	First Brillouin zone
2D	Two-dimensional
CBM	Conduction band minimum
CBO	Conduction band offset
DFT	Density Functional Theory
DOS	Density of States
ENCUT	Plane-waves energy cutoff
FET	Field effect transistor
GGA	Generalized-Gradient Approximation
Gr	Graphene
hBN	Hexagonal boron nitride
HF	Hartree-Fock
LDA	Local Density Approximation
LED	Light emitting diode
MOSFET	Metal-oxide-semiconductor field effect transistor
Ph	Phosphorene
QP	Quasiparticle
TFET	Tunneling field-effect transistor
TMDC	Transition Metal Dichalcogenide
VASP	Vienna *Ab-initio* Simulation Package
VBM	Valence band maximum
VBO	Valence band offset
vdW	van der Waals
XC	Exchange-correlation

List of Symbols

$\mathbf{a}_i$	Direct Bravais lattice vector
$\mathbf{b}_i$	Reciprocal lattice vector/Second Bravais lattice vector
$\tilde{D}_{ij}$	Projection element of n as function of $\tilde{n}$
D^1_{ij}	Projection element of n as function of n^1
$\tilde{D}^1_{ij}$	Projection element of n as function of $\tilde{n}^1$
e	Electron charge
e_c	Density of correlation energy
e_x	Density of exchange energy
e_{xc}	Density of exchange and correlation energy
E	Energy
E_c	Correlation energy
E_F	Fermi energy
E_x	Exchange energy
E_{xc}	Exchange and correlation energy
$\mathbf{G}$	Vector of the reciprocal lattice
$\hat{H}$	Hamiltonian operator
$\hat{\tilde{H}}$	Hamiltonian operator acting on a pseudo-function
h	Planck constant
$\hbar$	Reduced Planck constant
k_B	Boltzmann constant
k_F	Fermi wavevector
$\hat{I}$	Identity operator
i	Imaginary number, equal to $\sqrt{-1}$
$\hat{M}$	Transformation matrix
m	Mass of the particle associated to the wavefunction ψ
m_e	Electron mass
m_i	Integer number ($i \in \mathbb{Z}$)
n	Electronic density
$\tilde{n}$	Pseudo-electronic density
n^1	Electronic density of the real function at the atomic site

$\tilde{n}^1$	Pseudo-electronic density of the real function at the atomic site
N_i	Integer number ($i \in \mathbb{N}$)
$\mathbf{r}$	Position of an arbitrary point in space
r_c	Radius of a sphere centered at an atomic site
$\mathbf{R}$	Vector of the direct lattice
$\mathbf{R}_k$	Position of the nucleus from atom k
S	Unit cell area
$\hat{T}$	Kinetic energy operator
T_0	Kinetic energy of non-interacting electrons
$\hat{\mathcal{T}}$	Transformation that relates pseudo-wavefunctions to wavefunctions
U_0	Potential energy of non-interacting electrons
$\hat{V}$	Potential energy operator
$\hat{V}_{\text{ef}}$	Effective potential energy operator
V	Potential energy function
V_{ee}	Electron-electron interaction potential
V_{ext}	External potential
V_H	Hartree potential
V_{KS}	Kohn-Sham potential
V_{xc}	Exchange and correlation potential
x	Position/direction x
y	Position/direction y
z	Position/direction z
ϵ_i	Lagrange multipliers ($i \in \mathbb{N}$)
ε_0	Vacuum electric permittivity
ε	Strain applied to a material
$\hat{\Sigma}_X$	Fock operator
φ	Temporal part of a wavefunction
ϕ	Wavefunction; Kohn-Sham orbitals; Hartree-Fock orbitals
Φ	Kohn-Sham wavefunction
ψ	Spacial part of a wavefunction
ψ_i	Wavefunction i from a basis of orbitals
Ψ	Wavefunction (spacial and temporal parts)
Ψ^*	Complex-conjugated of the Ψ wavefunction
$\tilde{\Psi}$	Pseudo-wavefunction
Ψ^1	Real wavefunction at the atomic site
$\tilde{\Psi}^1$	Pseudo-wavefunction at the atomic site
$\|\Psi\rangle$	Wavefunction (ket, in Dirac's notation)
$\langle\Psi\|$	Wavefunction dual (bra, in Dirac's notation)
$\langle A\rangle_\psi$	Expected value of the $\hat{A}$ operator on ψ

$\mathbb{R}$	Real numbers set
∇_j	Gradient operator in j coordinates
∇^2	Laplacian operator

Contents

1 Introduction

1.1 Motivation

Since 2004, the scientific world faces a new paradigm in materials science with the introduction of graphene, the first atom-thick two-dimensional (2D) crystal structure obtained from the exfoliation of graphite (NOVOSELOV *et al.*, 2004). For their experiments with this structure, the Physics Nobel Laureates (2010) Andre Geim and Konstantin Novoselov leveraged a scientific vanguard to study disruptive features offered by this 2D crystal (GEIM; NOVOSELOV, 2007). Among the outstanding properties displayed by graphene, it is possible to enumerate its: zero effective mass and ballistic transport at room temperature (MOROZOV *et al.*, 2008; MAYOROV *et al.*, 2011), which allows electric current densities six times larger than in copper; Young's modulus of 1 TPa and breaking strength of 42 N m^{-1} (LEE *et al.*, 2008), making it the stronger material known; excellent thermal conductivity, on the order of 5000 W/mK (BALANDIN *et al.*, 2008); impermeability to gases (BUNCH *et al.*, 2008); and several others.

Although it holds great potential for electronics, graphene is a zero-gap semiconductor. The lack of control over charge carriers renders graphene inappropriate to build logic gates, since it is impossible to switch this material on and off without destroying some of its useful properties (SCHWIERZ, 2010; SCHWIERZ, 2013). Therefore, the development of 2D electronics and optoelectronics still has lots of challenges to face before becoming scalable.

Graphene, however, is not the only 2D crystal available nowadays (XU *et al.*, 2013; BUTLER *et al.*, 2013; MAS-BALLESTE *et al.*, 2011). Among the most popular 2D crystals is hexagonal boron nitride (hBN). Its insulating properties in a monolayer crystal are used for enhanced dielectrics (DEAN *et al.*, 2010), interface decoupling (VERBITSKIY *et al.*, 2015), avoidance of chemical degradation (MAYOROV *et al.*, 2011) and tunneling barrier (AMET *et al.*, 2012). The huge band gap is also promising for ultraviolet optoelectronic devices (PAKDEL *et al.*, 2014) and band alignment engineering (KING *et al.*, 2014).

Another group of widely studied and interesting materials are transition metal dichalcogenides (TMDCs). Their unique electronic properties include layer-dependent band gap

in the visible spectrum, which allows band engineering for field-effect transistors (FET) and flexible and transparent optoelectronic devices (JARIWALA *et al.*, 2014; WANG *et al.*, 2012). Molybdenum dichalcogenides are notorious examples of useful semiconducting compounds for electronic devices. FET fabricated with MoS_2 have displayed a current on/off ratio as high as 10^8 and low power consumption (RADISAVLJEVIC *et al.*, 2011) while photosensitive devices have shown improved response when compared with graphene (YIN *et al.*, 2011). Molybdenum diselenide ($MoSe_2$), on the other hand, exhibit a direct optical band gap of 1.55 eV, which is close to the optimal value for solar cells applications (TONGAY *et al.*, 2012). Moreover, FET manufactured with $MoSe_2$ have also been reported, displaying properties such as high temperature dependence (LARENTIS *et al.*, 2012) and low noise (DAS *et al.*, 2015).

A fourth important example among trending 2D crystals is the monolayer black phosphorus, named phosphorene (Ph). This buckled single-layer crystal with a rectangular Bravais lattice is strongly anisotropic (FEI; YANG, 2014) and has an on-off ratio up to 10,000 (LIU *et al.*, 2014). Furthermore, black phosphorus has a direct band gap depending on the number of layers and up to 1.51 eV in the monolayer case (QIAO *et al.*, 2014). This crystal suggests application in solar cells, photosensors and atomically-thin transistors.

Different semiconductors can be assembled to take advantage of the amalgamated properties. In the case of 2D materials, one efficient way of doing this is by stacking the layers to form van der Waals (vdW) heterostructures (GEIM; GRIGORIEVA, 2013). The wide library of 2D crystals and the absence of lattice-matching constraints on vdW stacks broaden possibilities for novel devices based on interface modulation, such as hBN-based quantum wells (DUFFERWIEL *et al.*, 2015; WITHERS *et al.*, 2015). In general, heterojunctions are crucial elements in modern electronic, photonic, optoelectronic and photovoltaic semiconductor technologies (KROEMER, 2001; TSAI *et al.*, 2014). The electronic properties from each side of the interface can come in three different configurations (see Fig. 1.1) and determine the joint behavior of the junction. For instance, photovoltaic action for electron and hole separation requires type-II heterostructures (KITTEL, 2004) for light-harvesting (SONG *et al.*, 2000), while light-emitting diodes benefit from a type-I band alignment (KITTEL, 2004) for a high emission efficiency (WALTEREIT *et al.*, 2000). Vertical tunneling field effect transistors (TFETs) may count on (nearly) broken-gap alignment, or type-III (KITTEL, 2004), for better performance (YAN *et al.*, 2015).

vdW heterostructures based on atomically thin 2D crystals are fundamentally different and more flexible than those based on conventional covalently bonded semiconductor interfaces. Their arrangement can be made with almost arbitrary order and orientation (GEIM; GRIGORIEVA, 2013). The lack of strong bonds between vdW materials enables for high-quality interfaces without the constraint of atomically precise commensurability (CHHOWALLA *et al.*, 2013; LEE *et al.*, 2014; ARGENTERO *et al.*, 2017). These

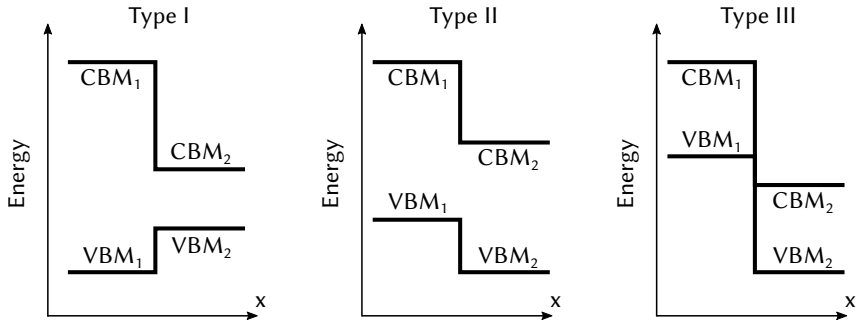

FIGURE 1.1 – Band alignments for semiconductor heterojunctions. For each material (1 or 2) on the interface, the valence band maximum (VBM) and conduction band minimum (CBM) are shown.

characteristics make vdW heterostructures promising to the future of electronics and optoelectronics.

Up to now, however, no theory has been developed to fully describe the band alignments in vdW-bonded crystals. Therefore, this dissertation tackles a main question on the understanding of vdW heterostructures: how do band alignments and band offsets, which determine any heterojunction, behave on such interfaces? To handle this question from a theoretical perspective, we break this investigation into four subquestions: (i) how to simulate vdW heterostructures using *ab initio* calculations with low computational cost and realistic modeling? (ii) How do stacking and rotation influence the electronic properties of vdW interfaces? (iii) How does external perturbations, such as pressure and electric field tune the interface properties and band alignments? And (iv) what are the underlying rules for band alignments in these interfaces, and do the electron affinity rule apply for such contacts?

In this work, we present a systematic work on 2D crystals and their vdW heterostructures to answer these questions. From the development of a mathematical method to simulate these systems to comprehensive analysis of their electronic properties, we push the boundaries of our current understanding of band alignments on 2D crystals and vdW heterojunctions.

1.2 Objectives

This dissertation aims to provide theoretical descriptions of monolayer 2D systems and their vdW heterostructures using mathematical models and first-principles calculations. We propose ourselves to supply reliable and systematic content on structural and electronic properties of these systems. We also try to explain phenomena arising in these interfaces using current physical and chemical theory, emphasizing the importance of theoretical predictions to develop new technology.

1.3 Structure

This dissertation is structured as follows, according to the sequence of its chapters:

1. **Introduction**, in which the context of 2D materials and vdW heterostructures is presented, as well as the problems to be tackled and goals to be reached in this dissertation;

2. **Theoretical methodology**, which describes the theoretical principles used in this work, from topics on quantum mechanics to the density functional theory. The coincidence lattice method, which provides a method to predict favorable vdW heterostructures, is also presented;

3. **Prediction of coincidence lattices**, which provides a benchmark of 2D monolayers, a validation of the coincidence lattice method and favorable combinations for studying electronic properties and band alignments of vdW heterostructures;

4. **Influences of stacking and rotation on band alignments**, in which the coincidence lattice method is employed to understand the influences of stacking of lattice-matched and -mismatched HfS_2, ZrS_2 and MoS_2 heterobilayers on their electronic properties. The effects of the interlayer twist on electronic and structural properties of hBN/$MoSe_2$ heterostructures are also studied;

5. **Influences of external perturbations on band alignments**, in which stacks of phosphorene combined with $MoSe_2$ and WSe_2 are studied and a series of novel phenomena due to stacking and external effects are demonstrated. Furthermore, band offsets are tuned by external perturbations;

6. **Validity of the Anderson rule**, which presents a comprehensive analysis of band alignments for ten heterocombinations of 2D crystals with tin dichalcogenides. Then, the application of the Anderson rule to vdW heterostructures is questioned, and a theory to describe failures of the model is proposed;

7. **Conclusions**, which summarize the results found, positioning them in the scientific context of this work.

2 Theoretical methodology

In this chapter, fundamental concepts to be used in this dissertation are introduced. We start from concepts on quantum mechanics and solid state physics, which are the founding stones for this work. Then, the Hartree-Fock approximation and the Density Functional Theory are introduced as the main tools of electronic structure calculations.

2.1 Schrödinger equation

The foundation of the entire quantum mechanics is the Schrödinger equation and a set of postulates (PIZA, 2009; SAKURAI; NAPOLITANO, 2013). Its description relates the temporal evolution of a wavefunction according to its conditions. These latter are described by means of a hamiltonian operator $\hat{H}$ containing the entire dynamics of the system. Therefore, the Schrödinger's equation is described in its operator format,[1]

$$\hat{H}\Psi = i\hbar\frac{\partial}{\partial t}\Psi, \tag{2.1}$$

where Ψ is a wavefunction subject to the normalization

$$\int_{\mathbb{R}^3} \Psi^*(\mathbf{r},t)\Psi(\mathbf{r},t)d^3r = 1. \tag{2.2}$$

Eq. (2.1) can be rewritten as function of the kinetic ($\hat{T}$) and potential ($\hat{V}$) energy operators,

$$(\hat{T} + \hat{V})\Psi = i\hbar\frac{\partial}{\partial t}\Psi. \tag{2.3}$$

Considering a time-independent potential, the problem can be solved using the separation of variables

$$\Psi(\mathbf{r},t) = \psi(\mathbf{r})\varphi(t), \tag{2.4}$$

[1]The spacial and temporal dependency of the wavefunctions is sometimes implicit to avoid notation overload.

leading to an equation with a only spatial or temporal dependency, as described by the eigenvalues spatial equation

$$(\hat{T} + \hat{V})\psi = \left(-\frac{\hbar^2}{2m}\nabla^2 + \hat{V}\right)\psi = E\psi, \tag{2.5}$$

and the temporal equation

$$i\hbar\frac{\partial}{\partial t}\varphi = E\varphi. \tag{2.6}$$

Equation (2.5) allows us to find the eigenstates of the hamiltonian $\hat{H}$, while Eq. (2.6) determines the dynamics of the wavefunctions evolution.

Expected values for observables in a quantum mechanical system can be made by integrating the wavefunction ψ in $\mathbb{R}^3$. For a generic operator $\hat{A}$,

$$\langle A\rangle_\psi = \int \psi^*(\mathbf{r})\hat{A}\psi(\mathbf{r})d^3r, \tag{2.7}$$

or, using the Dirac notation,

$$\langle A\rangle = \langle\psi|\hat{A}|\psi\rangle. \tag{2.8}$$

2.2 Bloch theorem

By applying the Schrödinger equation to an electron in a solid, it is possible to obtain its behavior, essential to the Solid State Physics. By definition, crystals are ordered and periodic arrangements of atoms. This ordering is described by a Bravais lattice (ASHCROFT; MERMIN, 1976),

$$\mathbf{R} = m_1\mathbf{a}_1 + m_2\mathbf{a}_2 + m_3\mathbf{a}_3, \tag{2.9}$$

with $\mathbf{a}_i$ vectors in $\mathbb{R}^3$ and m_i integer numbers. The vectors $\mathbf{a}_i$ enclose a region in $\mathbb{R}^3$ defined as the crystal unit cell. It has all information of the periodic crystal and is at least one period of it.

The position of the atoms in the crystal is described by an atomic basis. Therefore, it is possible to mathematically replicate a unit cell with atoms in well-defined positions in all space, thus defining an infinite crystalline solid. In this case, the potential felt by the

electron obeys

$$V(\mathbf{r}) = V(\mathbf{r} + \mathbf{R}). \tag{2.10}$$

The electron wavefunction in this periodic potential is given by the Bloch theorem (ASHCROFT; MERMIN, 1976),

$$\psi_{n\mathbf{k}}(\mathbf{r}) = e^{i\mathbf{k}\cdot\mathbf{r}} u_{n\mathbf{k}}(\mathbf{r}), \tag{2.11}$$

where $\mathbf{k}$ is the wavevector, n the band index and $u_{n\mathbf{k}}(\mathbf{r})$ is a function with the periodicity of the Bravais lattice, that is,

$$u_{n\mathbf{k}}(\mathbf{r}) = u_{n\mathbf{k}}(\mathbf{r} + \mathbf{R}). \tag{2.12}$$

Consequently, the wavefunction has the property

$$\psi_{n\mathbf{k}}(\mathbf{r} + \mathbf{R}) = e^{i\mathbf{k}\cdot\mathbf{R}} \psi_{n\mathbf{k}}(\mathbf{r}). \tag{2.13}$$

An interpretation can be assigned to these results. Eigenstates of the hamiltonian operator associate a wavevector $\mathbf{k}$ for each wavefunction $\mathbf{k}$ that obeys the periodicity given by Eq. (2.13).

To allow for the analysis of an infinite solid from the finite solid limit, it is useful to impose some boundary conditions to the wavefunctions. Usually, Born-von Karman boundary conditions are adopted by its periodicity treatment in arbitrarily larger volumes. These conditions require that

$$\psi(\mathbf{r} + N_i\mathbf{a}_i) = \psi(\mathbf{r}),\ i = 1,2,3, \tag{2.14}$$

where N_i are integer numbers related to the number of unit cells in the direction of the vector $\mathbf{a}_i$. The total number N of primitive cells on the finite crystal with the Born-von Karman conditions is

$$N = N_1 N_2 N_3. \tag{2.15}$$

According to Eq. (2.13), we should have

$$\psi_{n\mathbf{k}}(\mathbf{r} + N_i\mathbf{a}_i) = e^{i\mathbf{k}\cdot N_i\mathbf{a}_i} \psi_{n\mathbf{k}}(\mathbf{r}), \tag{2.16}$$

that is,

$$e^{i\mathbf{k}\cdot N_i\mathbf{a}_i} = 1. \tag{2.17}$$

A way to satisfy the Eq. (2.17) is to define a set of vectors $\mathbf{b}_i$ given by

$$\begin{cases} \mathbf{b}_1 = 2\pi \frac{\mathbf{a}_2\times\mathbf{a}_3}{\mathbf{a}_1\cdot(\mathbf{a}_2\times\mathbf{a}_3)} \\ \mathbf{b}_2 = 2\pi \frac{\mathbf{a}_3\times\mathbf{a}_1}{\mathbf{a}_1\cdot(\mathbf{a}_2\times\mathbf{a}_3)} \\ \mathbf{b}_3 = 2\pi \frac{\mathbf{a}_1\times\mathbf{a}_2}{\mathbf{a}_1\cdot(\mathbf{a}_2\times\mathbf{a}_3)} \end{cases}, \tag{2.18}$$

The linear combination $\mathbf{G}$ of these vectors,

$$\mathbf{G} = n_1\mathbf{b}_1 + n_2\mathbf{b}_2 + n_3\mathbf{b}_3. \tag{2.19}$$

defines the reciprocal lattice of the crystal. Therefore, Bloch wavevectors $\mathbf{k}$ are given by

$$\mathbf{k} = \sum_{i=1}^{3} \frac{m_i}{N_i}\mathbf{b}_i, \tag{2.20}$$

satisfying Eq. (2.17).

Reciprocal lattice vectors given by (2.18) are analogous to those from the direct lattice of Eq. (2.9). It is possible to understand the former as a Fourier series to the discrete space of the latter. Therefore, it is natural that the reciprocal lattice (2.19) is periodic and has a primitive cell. The smallest cell of the reciprocal lattice and centered at the point (0,0,0) is called first Brillouin zone (1BZ).

For 2D materials, the solid is treated as if one of the direct lattice vectors is much larger than the others, asymptotically leading to the 2D case. In this case, one of the reciprocal lattice vectors would have norm close to zero and its 1BZ would be 2D as well.

A Fourier analysis is now possible, using the wavefunctions from Eqs. (2.11) and (2.12),

$$\psi_{n\mathbf{k}} = e^{i\mathbf{k}\cdot\mathbf{r}} \sum_{\mathbf{G}} c_{n\mathbf{k}} e^{i\mathbf{G}\cdot\mathbf{r}}. \tag{2.21}$$

In this case, the wavefunction $\psi_{n\mathbf{k}}$ was decomposed in a series of plane waves with momenta given by vectors $\mathbf{G}$ of the reciprocal lattice. The kinetic energy of a plane wave is calculated by

$$\frac{-\hbar^2}{2m}\nabla^2 e^{i\mathbf{G}\cdot\mathbf{r}} = \frac{-\hbar^2 G^2}{2m} e^{i\mathbf{G}\cdot\mathbf{r}}. \tag{2.22}$$

To obtain a computationally feasible approximation, it is necessary to truncate the Fourier series from Eq. (2.21). In general, this is made by truncating the vectors $\mathbf{G}$ describing the basis of ψ in Eq. (2.22) up to a maximum plane waves kinetic energy. As higher energy components represent faster oscillations, adequate descriptions for macroscopic systems such as solids can be obtained by this truncation. The criterion to determine this limit, however, has to be derived from convergence analysis of the wavefunction under study.

2.3 Hartree-Fock approximation

Up to now, only the problem of an electron in a periodic potential was treated. When considering an atomic, molecular or solid system, the complexity increases. For an interacting many-body system with the Coulomb potential, the hamiltonian is

$$\hat{H} = \hat{T} + \hat{V} + \hat{V}_{\text{int}}, \tag{2.23}$$

where $\hat{T}$ and $\hat{V}$ are the operators given by the sum of the kinetic and Coulomb potential energy of all particles, respectively, and $\hat{V}_{\text{int}}$ is the interacting energy between particles. If we consider the mass of the atomic nuclei much larger than those from electrons, it is possible to approximate a solid by fixing the atomic nuclei. Then, the kinetic energy of the wavefunction is solely due to electrons. This also simplifies the repulsion between nuclei and allow us to fix the Coulomb potential of the atom as an external potential $\hat{V}_{\text{ext}}$ acting towards the electrons. With this simplification, called Born-Oppenheimer approximation (ASHCROFT; MERMIN, 1976), the hamiltonian of the many-body system is written as

$$\hat{H} = \underbrace{-\frac{\hbar^2}{2m_e}\sum_j \nabla_j^2}_{\hat{T}} + \underbrace{\sum_j V_{\text{ext}}(\mathbf{r}_j)}_{\hat{V}} + \underbrace{\frac{1}{2}\frac{e^2}{4\pi\varepsilon_0}\sum_j\sum_{k\neq j}\frac{1}{|\mathbf{r}_j - \mathbf{r}_k|}}_{\hat{V}_{\text{int}}}. \tag{2.24}$$

From this point on, it is useful to employ atomic units to the description of the equations. Conveniently, we adopt

$$\frac{1}{4\pi\varepsilon_0} = e = \hbar = m_e = 1. \tag{2.25}$$

In the Hartree system of units, the quantities from Eq. (2.25) are dimensionless. The length unit is the Bohr radius (0,529 Å), the speed of light is the inverse of the fine structure constant (approximately 1/137) and energies are given in Hartree, with 1 H = 27.2114 eV = $4.359 \cdot 10^{-18}$ J. The convenience of this system of units lies in the absence of small

constants such as $\hbar$ in calculations — which is useful in computational representations of the floating-point values — and in the simplified notation we obtain. Therefore, Eq. (2.24) is rewritten as

$$\hat{H} = -\frac{1}{2}\sum_j \nabla_j^2 + \sum_j V_{\text{ext}}(\mathbf{r}_j) + \frac{1}{2}\sum_j \sum_{k\neq j} \frac{1}{|\mathbf{r}_j - \mathbf{r}_k|}, \tag{2.26}$$

which, for the Coulomb potential, is equivalent to

$$\hat{H} = -\frac{1}{2}\sum_j \nabla_j^2 + \sum_j \sum_k \frac{Z_k}{|\mathbf{r}_j - \mathbf{R}_k|} + \frac{1}{2}\sum_j \sum_{k\neq j} \frac{1}{|\mathbf{r}_j - \mathbf{r}_k|}, \tag{2.27}$$

where Z_k is the charge of the atomic nucleus indexed by k, with $\mathbf{R}_k$ its respective position.

From the given hamiltonian, it is possible, in principle, to solve the Schrödinger equation. However, when one observes Eq. (2.27), it is seen that a system with N electrons, each one described by a vector $\mathbf{r}_j$ in $\mathbb{R}^3$, has a Schrödinger equation dependent of $3N$ coordinates. Since the number of parameters necessary to solve the equation scales exponentially with the number of coordinates, the problem quickly turns to be unfeasible. Furthermore, the electron-electron interaction is not determined in an analytical manner, which further the complexity of the Schrödinger equation.

To work around these problems, more approximations can be made. A first one is the Hartree-Fock (HF) approximation (PARR, 1980). It is based on the variational principle of quantum mechanics, which states that if ψ is the ground state of the hamiltonian operator, then

$$\langle\psi|\hat{H}|\psi\rangle \leq \langle\phi|\hat{H}|\phi\rangle, \tag{2.28}$$

for all wavefunctions ϕ. The search for the ground state, therefore, can be done by minimizing the expected value of the energy, as in Eq. (2.28). Usually, this is made possible using trial functions ψ_α and minimizing the expected value of the hamiltonian with respect to the parameter α.

The HF approximation supposes a family of wavefunctions Φ satisfying the properties of a fermionic or bosonic system. In the case of fermions, such as electrons, this wavefunction is antisymmetric when the spin is included. Therefore, the exchange of two particles leads

only to a 180° phase shift. In the HF method, Φ is described by a Slater determinant,

$$\Phi(\mathbf{r}_1\sigma_1,\ldots,\mathbf{r}_N\sigma_N) = \frac{1}{\sqrt{N!}}\det\begin{pmatrix} \phi_1(\mathbf{r}_1)\sigma_1(\chi_1) & \ldots & \phi_1(\mathbf{r}_N)\sigma_1(\chi_N) \\ \vdots & & \vdots \\ \phi_N(\mathbf{r}_1)\sigma_N(\chi_1) & \ldots & \phi_N(\mathbf{r}_N)\sigma_N(\chi_N) \end{pmatrix}, \tag{2.29}$$

where ϕ_i form a set of orthonormal orbitals. Based on this family of functions, the expected value of the hamiltonian is minimized. To do so, the Lagrange multipliers method is employed to the space of functions ϕ_i. Mathematically, this requires a functional derivative of the Schrödinger equation with respect to the trial function given by (2.29),

$$\frac{\delta}{\delta\phi_i^*}\left[\langle\Phi|\hat{H}|\Phi\rangle - \sum_j \epsilon_j\left(\langle\phi_j|\phi_j\rangle - 1\right)\right] = 0, \tag{2.30}$$

where ϵ_j are the Lagrange multipliers of the problem. Applying the hamiltonian from Eq. (2.27) in the Schrödinger equation and further development of the Eq. (2.30) allows us to obtain an expression to the electronic interaction. This leads us to the Hartree-Fock equations, which consist in a system of differential equations similar to the Schrödinger equation, given by

$$\left[-\frac{\nabla^2}{2} + V_{\text{ext}}(\mathbf{r}) + V_H(\mathbf{r}) + \hat{\Sigma}_X\right]\phi_i = \epsilon_i\phi_i, \tag{2.31}$$

where the electron-electron interaction is divided into a classic contribution V_H, the Hartree term, with

$$V_H(\mathbf{r}) = \sum_j \int \frac{|\phi_j(\mathbf{r}',\sigma)|^2}{|\mathbf{r}-\mathbf{r}'|}d^3r' = \sum_j \int \frac{n(\mathbf{r}')}{|\mathbf{r}-\mathbf{r}'|}d^3r', \tag{2.32}$$

and a quantum contribution $\hat{\Sigma}_X$, the Fock term, with

$$\hat{\Sigma}_X\phi_i = -\sum_j \int \frac{\phi_i(\mathbf{r}',\sigma)\phi_j^*(\mathbf{r}',\sigma)\phi_j(\mathbf{r},\sigma)}{|\mathbf{r}-\mathbf{r}'|}d^3r'. \tag{2.33}$$

Equation (2.32) can be written in terms of the electronic density $n(\mathbf{r})$, while Eq. (2.33) can be only expressed in terms of orbitals ϕ_i. The slow part of this method consists in the calculation of these contributions, also known as the exchange expression. Since the algorithm is of order $\mathcal{O}(N^2)$, the computational complexity is high in this method.

The HF method allows us to iteratively solve the problem. A first trial is given by

the superposition of orbitals of interest to define Eq. (2.29). Then, the Hartree and Fock operators are constructed based on Eqs. (2.32) and (2.33). From this point on, the problem is reduced to a matrix diagonalization, in which the new eigenstates ϕ_i satisfying the HF equations should be found. Once these eigenstates are found, the Hartree and Fock operators can be constructed again, and the procedure can be repeated. This cycle is known as the self-consistent cycle, and is useful for the numeric convergence of the problem. In general, stopping criteria have to be defined to halt the self-consistent cycle. Some possibilities are the variation of the total energy of the eigenvalues between two iterations.

As a first approximation, the HF method is surprisingly useful. Most popular in quantum chemistry due to its approach using wavefunctions and orbitals, it reasonably describes atomic and molecular systems. However, significant deviations are found when comparing the theoretical results with measurements, since the Slater determinant is not able to adequately describe the complete wavefunction. By definition, the Slater determinant does not represent the correlation between electrons, that is, the Coulomb repulsion one electron imparts on the other. This is due to the local dependency of each orbital ϕ_i.

2.4 Density Functional Theory

In quantum mechanics, the wavefunction of a system is enough to describe it completely. The HF method has shown a perspective to solve many-body problems using an approximation to the wavefunction and solving a system of differential equations in a self-consistent manner. This method, however, has main disadvantages regarding high computational efforts and the absence of correlation effects.

In 1964, Walter Kohn and Pierre Hohenberg proposed a theory that immediately shifted this paradigm in quantum mechanics. Instead of depending solely on the wavefunction, the Density Functional Theory (DFT) proves that properties of physical systems, such as total energy, are functionals of the electronic density $n(\mathbf{r})$ of the ground state. Therefore, there is a mapping between a three-variable function $n(\mathbf{r})$ to a real number, which is a quantity of interest. Furthermore, the DFT presents an exact derivation for the calculation of these properties. Although an analytical and closed theory for the DFT is not yet available, studies are still being made in this line to improve the description of electronic systems.

It is immediately evident that making calculations with a real function of three variables is much simpler than solve differential equations with $3N$-variable systems. The improvement in terms of computational effort and accuracy renders DFT a good alternative to the HF procedure, specially when the systems under investigation are solids.

2.4.1 Hohenberg-Kohn theorems

The theorems of Hohenberg-Kohn determine the exactness of DFT (HOHENBERG; KOHN, 1964). In the first theorem, it is shown that there is an injection between the electronic density $n(\mathbf{r})$ of the ground state and a potential up to a constant. In other words, given an electronic density of the ground state, it is possible to find a family of potentials differing by less than a constant, that generates this ground state electronic density.

The formal demonstration of this first theorem is surprisingly simple. It is made by contradiction, supposing, in the first place, that there are two potentials $V_{\text{ext},1}(\mathbf{r})$ and $V_{\text{ext},2}(\mathbf{r})$ that differ by more than a constant, but lead to the same ground state electronic density $n(\mathbf{r})$. Both potentials determine two hamiltonians $\hat{H}_1$ and $\hat{H}_2$, similarly to Eq. (2.24). Consequently, two different wavefunctions, Ψ_1 and Ψ_2, are associated to these operators.

Given that both wavefunctions are distinct, the variational principle from Eq. (2.28) assures that

$$\langle\Psi_1|\hat{H}_1|\Psi_1\rangle < \langle\Psi_2|\hat{H}_1|\Psi_2\rangle. \tag{2.34}$$

Replacing a hamiltonian such as $\hat{H}_i = \hat{T} + \hat{V}_{\text{ee}} + \hat{V}_{\text{ext,i}}$ in Eq. (2.34) leads to

$$\langle\Psi_1|\hat{T} + \hat{V}_{\text{ee}} + \hat{V}_{\text{ext},1}|\Psi_1\rangle < \langle\Psi_2|\hat{T} + \hat{V}_{\text{ee}} + \hat{V}_{\text{ext},1}|\Psi_2\rangle. \tag{2.35}$$

However, the expected value of the external potential is better understood using the notation from Eq. (2.7),

$$\langle\Psi_i|\hat{V}_{\text{ext},1}|\Psi_i\rangle = \int \psi_i^*(\mathbf{r})V_{\text{ext},1}\psi_i(\mathbf{r})d^3r = \int V_{\text{ext},1}n_i(\mathbf{r})d^3r. \tag{2.36}$$

Since by hypothesis both wavefunctions have the same density,

$$n(\mathbf{r}) = \psi_1^*(\mathbf{r})\psi_1(\mathbf{r}) = \psi_2^*(\mathbf{r})\psi_2(\mathbf{r}), \tag{2.37}$$

the inequality from Eq. (2.35) is simplified to

$$\langle\Psi_1|\hat{T} + \hat{V}_{\text{ee}}|\Psi_1\rangle < \langle\Psi_2|\hat{T} + \hat{V}_{\text{ee}}|\Psi_2\rangle. \tag{2.38}$$

Repeating the same procedure but exchanging Ψ_1 by Ψ_2 leads to

$$\langle\Psi_2|\hat{T}+\hat{V}_{\text{ee}}|\Psi_2\rangle < \langle\Psi_1|\hat{T}+\hat{V}_{\text{ee}}|\Psi_1\rangle. \tag{2.39}$$

Equations (2.38) and (2.39) cannot be simultaneously satisfied, rendering the initial hypothesis an absurd and completing the proof. Therefore, it is not possible to two potentials which differ by more than a constant to lead to the same electronic density of the ground state. As a corollary of the first Hohenberg-Kohn theorem, the density can be used to completely describe any quantum mechanical system.

The consequence of this demonstration is more useful than it seems. It implies that the knowledge of the electronic density of the ground state allow us to find the potential of the system, thus, its eigenstates and eigenvalues.

The second Hohenberg-Kohn theorem attests that the electronic density of the ground state of a system also minimizes its energy. The demonstration is evident: if the density of the ground state does not minimizes the energy, then, there is another density for which the energy is minimum. Invoking the variational principle, the initial density could not be that from the ground state.

Based on both Hohenberg-Kohn theorems, all informations from a system may be derived from the electronic density. Therefore, it is possible to assure the existence of a functional from the density to the energy,

$$E[n(\mathbf{r})] = \langle\Psi|\hat{T}+\hat{V}_{\text{ee}}+\hat{V}_{\text{ext}}|\Psi\rangle, \tag{2.40}$$

that can be rewritten in terms of the external potential and the electronic density as

$$E[n(\mathbf{r})] = \langle\Psi|\hat{T}+\hat{V}_{\text{ee}}|\Psi\rangle + \int n(\mathbf{r}')V_{\text{ext}}(\mathbf{r}')d^3r'. \tag{2.41}$$

A usual way to write the expected value of the kinetic energy and the electron-electron interaction is

$$F[n(\mathbf{r})] = \min_{\Psi\to n}\langle\Psi|\hat{T}+\hat{V}_{\text{ee}}|\Psi\rangle, \tag{2.42}$$

leading to the ground state energy

$$E[n(\mathbf{r})] = F[n] + \int n(\mathbf{r}')V_{\text{ext}}(\mathbf{r}')d^3r'. \tag{2.43}$$

Many-body problems can be exactly solved using DFT. All derivations have been

made exact, and no approximation was made to Eq. (2.43). Thus, it suffices to know the functional of $F[n]$ in its exact form to solve all problems of energy in quantum systems. However, since it is not known, an approximate framework for the DFT is necessary.

2.4.2 Kohn-Sham scheme

The Kohn-Sham scheme is one of the first ways to solve many-body problems within the DFT (KOHN; SHAM, 1965). Its model bypasses one major problem in the description of electronic systems, namely the interaction term between particles. It creates a non-interacting system of particles that have exactly the same ground state electronic density of the interacting system. According to the first Hohenberg-Kohn theorem, both systems must have the same energy, since they share the same electronic density of the ground state.

The fictitious non-interacting system is best represented by a Slater determinant, as in Eq. (2.29). The DFT formalism allow us to write the unknown functional $F[n]$ as

$$F[n(\mathbf{r})] = U_0[n] + T_0[n] + E_{\text{xc}}[n], \tag{2.44}$$

where $U_0[n]$ and $T_0[n]$ are functionals relating the potential and kinetic energy, respectively, of a non-interacting system. The exchange-correlation (XC) energy E_{xc} cover all unknown information about the problem, i.e.

$$E_{\text{xc}}[n] = V_{\text{ee}}[n] - U_0[n] + T[n] - T_0[n], \tag{2.45}$$

where $V_{\text{ee}}[n]$ are $T[n]$ the electron-electron interaction and the kinetic energy, respectively, of the real system.

Having built a system in which particles are decoupled, the solution is quite similar to the HF method. The orbitals ϕ_i are chosen in such a way that the electronic density is given by

$$n(\mathbf{r}) = \sum_i |\phi_i(\mathbf{r})|^2. \tag{2.46}$$

The kinetic and potential energies of the system are obtained exactly as in the HF method,

$$T_0[n] = -\frac{1}{2}\langle\Phi|\nabla^2|\Phi\rangle = -\frac{1}{2}\sum_i \int \phi_i^*(\mathbf{r})\nabla^2\phi_i(\mathbf{r})d^3r, \tag{2.47}$$

and

$$U_0[n] = \frac{1}{2}\iint \frac{n(\mathbf{r})n(\mathbf{r}')}{|\mathbf{r}-\mathbf{r}'|}d^3r d^3r'. \tag{2.48}$$

We want to minimize the energy

$$E[n] = T_0[n] + U_0[n] + E_{\text{xc}}[n] + \int V_{\text{ext}}(\mathbf{r})n(\mathbf{r})d^3r, \tag{2.49}$$

subject to the normalization restriction to each orbital,

$$\langle\phi_i|\phi_i\rangle = 1, \tag{2.50}$$

which, on its turn, implies that the density is given by

$$\int n(\mathbf{r})d^3r = N. \tag{2.51}$$

As in the HF approximation, the minimization of the energy subject to a restriction is made by Lagrange multipliers, leading to the equation

$$\left[-\frac{\nabla^2}{2} + V_{\text{KS}}(\mathbf{r})\right]\phi_i(\mathbf{r}) = \epsilon_i\phi_i(\mathbf{r}), \tag{2.52}$$

where the Kohn-Sham potential V_{KS} is defined by

$$V_{\text{KS}} = V_{\text{ext}} + V_{\text{xc}} + V_{\text{H}}. \tag{2.53}$$

XC potentials V_{xc}, as well as Hartree potentials V_{H}, are obtained by functional derivatives

$$V_{\text{xc}} = \frac{\delta}{\delta n(\mathbf{r})}E_{\text{xc}}[n], \tag{2.54}$$

and

$$V_{\text{H}} = \frac{\delta}{\delta n(\mathbf{r})}U_0[n] = \int \frac{n(\mathbf{r}')}{|\mathbf{r}-\mathbf{r}'|}d^3r. \tag{2.55}$$

The Kohn-Sham scheme allows us to solve the problem iteratively. First of all, the density is initialized with an appropriate value for the system under study, such as a set of atomic orbitals in an non-interacting system. Then, the Kohn-Sham potential is calculated and solved from Eq. (2.52) and the density is obtained again. The process is repeated

until the stopping criteria is reached. Its implementation is simpler than the HF method because of the absence of a complex calculation such as the Fock operator. Therefore, DFT calculations are more efficient in terms of computational efforts when compared to its HF counterpart.

Up to now, however, the XC potential, as well as the expression for the XC energy, are still unknown. Nevertheless, as stated before, all passages are exact within the Kohn-Sham scheme. To solve real problems, approximations are necessary, which justifies the creation of systems which adequately describe the XC term.

2.4.3 Local Density Approximation

The local density approximation (LDA) is a first possible procedure to deal with the XC indeterminacy. Its solution was proposed by Kohn and Sham back in 1965 (KOHN; SHAM, 1965). The first deviation from the exact framework is to consider that the XC energy in an electronic system is identical to that seen in an homogeneous electron gas. This delocalized model, specially useful for infinite solids with the appropriate boundary conditions, asks for a more suitable definition of the XC energy $E_{\mathrm{xc}}[n]$ in terms of a density of XC energy $e_{\mathrm{xc}}[n]$,

$$E_{\mathrm{xc}}[n] = \int e_{\mathrm{xc}}[n] n(\mathbf{r}') d^3 r'. \tag{2.56}$$

If we use plane waves — which are uniform electronic densities in space — as orbitals in Eq. (2.33), we derive an analytical expression to the non-interacting electrons Fock operator. Thus, the density of exchange energy is given by

$$e_{\mathrm{x}}[n] = -\frac{3}{4}\left(\frac{3}{\pi}\right)^{1/3} n^{1/3}. \tag{2.57}$$

The correlation term is more complicated and does not possesses an analytical development (ENGEL; DREIZLER, 2011; BECHSTEDT, 2015). Approximations made by Quantum Monte Carlo simulations (CEPERLEY; ALDER, 1980) or the Random Phase Approximation are used to fit analytical expressions to this term (PERDEW; ZUNGER, 1981).

The LDA considers all electrons delocalized, but is able to describe surprisingly well the systems of interest. In solids, for example, the bond lengths are underestimated. Nevertheless, its accuracy is quite remarkable, with less than 5% of deviation from measurements (BECHSTEDT, 2015). Energy gaps in semiconductors and insulators, however, are severely underestimated by LDA. It is not uncommon to find errors superior

to 50% when these calculations are confronted with experiments (BECHSTEDT, 2015).

2.4.4 Generalized Gradient Approximation

An improvement over LDA can be made if non-local terms are included in the XC energy functional. Correlation is intrinsically non-local, and is overlooked by LDA when considered as a power of the density. To better the approximation, the energy expression is made also a functional of the density gradient, naming this technique "Generalized Gradient Approximation" (GGA), in a functional such as

$$E_{\mathrm{xc}}[n] = \int f[n, \nabla n] d^3r. \tag{2.58}$$

Initially proposed by Perdew and Yue (PERDEW; YUE, 1986) and later implemented within the popular functional PBE (PERDEW *et al.*, 1996; PERDEW *et al.*, 1997), the GGA model has the format (PARR, 1980)

$$E_{\mathrm{xc}}[n] = \int n(\mathbf{r}) e_{\mathrm{x}}[n] F_{\mathrm{xc}}(s) d^3r, \tag{2.59}$$

where F_{xc} is an enhancement factor such that, for the homogeneous electron gas,

$$s = \frac{|\nabla n|}{2k_F n}, \tag{2.60}$$

with

$$k_F = (3\pi^2 n)^{1/3}. \tag{2.61}$$

Beyond the more accurate description when compared to the LDA, thanks to the non-locality of the functional treatment, the GGA overestimates bond lengths when compared to measurements. However, no more than 3% of error is found, with a mean error of up to 0,95% for a set of selected 3D solids (BECHSTEDT, 2015). Just like LDA, the semiconductor and insulators band gap is underestimated. Its value can be as low as 30% of the measurements (BECHSTEDT, 2015).

2.4.5 Hybrid functionals

Since both DFT and HF present different advantages and drawbacks, one could think of performing joint DFT and HF calculations to obtain more accurate results. After all, HF has an exact exchange, while DFT deals correctly with correlation, which could lead

to better calculations.

Becke (1993) proposed the use of hybrid functionals, in which the hybrid XC energy $E_{\mathrm{xc}}^{\mathrm{hyb}}$ is composed by a mixture of the DFT and HF energies, following a linear relationship such as (FIOLHAIS *et al.*, 2003)

$$E_{\mathrm{xc}}^{\mathrm{hyb}} = E_{\mathrm{x}}^{\mathrm{HF}} + (1-a)(E_{\mathrm{x}}^{\mathrm{DFT}} - E_{\mathrm{x}}^{\mathrm{HF}}) + E_{\mathrm{c}}^{\mathrm{DFT}}. \tag{2.62}$$

Becke (1993) introduces the use of the parameter a as 1/2. In the case of $a = 1/4$, derived with the variational principle, the hybrid functional PBE0 is obtained (PERDEW *et al.*, 1996). Although the energy is improved in these systems, the convergence starts to be a problem in solids due to the long-range integral from HF calculations. Heyd *et al.* (2003) came up with the idea of dividing the exact exchange term in two parts: a short-range part and a long-range one. In this case, the XC energy is written as

$$E_{\mathrm{xc}}^{\mathrm{HSE06}} = \frac{1}{4}E_{\mathrm{x}}^{\mathrm{HF,sr}}(\mu) + \frac{3}{4}E_{\mathrm{x}}^{\mathrm{GGA,sr}}(\mu) + E_{\mathrm{x}}^{\mathrm{HF,lr}} + E_{\mathrm{c}}^{\mathrm{GGA}}, \tag{2.63}$$

having μ as an adjustable "screening" parameter, and with "sr" and "lr" standing for short range and long range, respectively. The XC energy is better represented when non-locality is included in the exchange energy. This also describes partially quasiparticle effects due to electronic excitations. This is a reason for the success of hybrid functionals, specially when its complexity is reduced by means of an artifice such as the one employed in HSE06 (BECHSTEDT, 2015). Mean absolute errors for band gaps of 40 different solids calculated with HSE, as reported by Janesko *et al.* (2009) are as small as 0.26 eV, while those calculated with PBE are about five times larger, equal to 1.13 eV (JANESKO *et al.*, 2009). As a trade-off, however, HSE06 calculations require more computational time and can be up to two order of magnitude slower than PBE calculations (LARRSON, 2015).

2.4.6 van der Waals corrections

van der Waals (vdW) interactions are essential to describe 2D materials. Although LDA and GGA are reasonably successful when calculating solid systems, London dispersions are not well taken into account due to the short range of the correlation in these methods (ENGEL; DREIZLER, 2011). Since, in the methods presented, these systems are solved by a local density, correlation effects are not enough to describe their electronic behavior. For instance, two atoms separated by a long distance may be almost non-interacting from a correlation point of view, due to the small wavefunction overlap. However, virtual excitations, such as ones in vdW interaction, give rise to forces which are not well described by these methods.

To solve this problem, Dion *et al.* (2004) proposed to adjust the correlation energy, dividing it in two,

$$E_c[n] = E_c^0[n] + E_c^{\text{nl}}[n], \tag{2.64}$$

where both terms on the right-hand side of Eq. 2.64 are non-local correlation energies. $E_c^0[n]$ is a term similar to the LDA one, while $E_c^{\text{nl}}[n]$ is responsible by the vdW interaction. Its format is something like

$$E_c^{\text{nl}}[n] = \frac{1}{2}\iint n(\mathbf{r})\phi(\mathbf{r},\mathbf{r}')n(\mathbf{r}')d^3r d^3r', \tag{2.65}$$

with $\phi(\mathbf{r},\mathbf{r}')$ a function dependent of $\mathbf{r}-\mathbf{r}'$.

In 2D systems or adsorption of molecules and surfaces, the importance of vdW interaction is necessary to predict adequate distances between systems and binding energies. The non-locality obtained by adjusting the correlation energy, therefore, deals adequately with the vdW interaction and alters stability effects.

2.4.7 Hellmann-Feynman theorem

From the energy minimum regarding structural stability of the systems under study, we verify whether atomic dynamics are close enough to the stability, thus ensuring their ground state geometries. Calculating forces acting on atoms, therefore, is a necessary condition to obtain a relaxed geometry in terms of internal stresses. In this case, the Born-Oppenheimer approximation should be discarded until an atomic configuration that minimizes the forces is found.

The Hellmann-Feynman theorem from quantum mechanics states that, given a normalized wavefunction Ψ^λ dependent of a parameter λ, which is an eigenstate of the hamiltonian $\hat{H}^\lambda$, the derivative of the expected value of the energy with respect to λ is given by (ENGEL; DREIZLER, 2011)

$$\frac{d}{d\lambda}\langle\Psi^\lambda|\hat{H}^\lambda|\Psi^\lambda\rangle = \langle\Psi^\lambda|\frac{\partial\hat{H}^\lambda}{\partial\lambda}|\Psi^\lambda\rangle. \tag{2.66}$$

If we adopt the positions of the atomic nuclei as parameters, Eq. (2.27) is then used as starting point for the calculation of forces on each atom. Mathematically,

$$\mathbf{F} = -\nabla_{\mathbf{R}_k}(E[n] + E_{\text{nucleus-nucleus}}[n]), \tag{2.67}$$

where $E_{\text{nucleus-nucleus}}[n]$ is the repulsion energy between nuclei. Developing the Eq. (2.67) based on Eq. (2.27), we have

$$\mathbf{F} = -\int n(\mathbf{r}) \frac{Z_k(\mathbf{R}_k - \mathbf{r})}{|\mathbf{R}_k - \mathbf{r}|^3} d^3r + \sum_j \sum_{k \neq j} \frac{Z_k Z_j (\mathbf{R}_k - \mathbf{R}_j)}{|\mathbf{R}_k - \mathbf{R}_j|^3}. \tag{2.68}$$

Equation (2.68) allows the calculation of atomic forces as function of the electronic density of the ground state and the positions of the other atoms. A relaxation algorithm is necessary to accordingly predict the equilibrium geometry of the system. First, the electronic density is calculated using the known techniques. Then, forces are obtained using Eq. (2.68). After adequate displacements are made in atomic positions, which are subtly designed to not raise instabilities on the algorithm nor let the convergence become too slow, a new geometry is found. From this new geometry, a new electronic density of the ground state is found, restarting the iterative process until convergence is reached.

2.4.8 Projector-Augmented Wave

Although several approximations are made, DFT solutions still are rather costly from a computational point of view. Even when the procedures explained so far are employed, the description of solids leads to problems such as:

- The singularity of the Coulomb potential renders too large the number of plane waves necessary to describe it adequately, specially when compared to non-singular potentials. The rapid oscillation of plane waves close to the atomic nuclei requires a high truncation energy in Eq. (2.22).
- Heavier elements in the periodic table require more electrons to be simulated, rendering simulations more costly and complex.

Several methods try to solve this problem, such as the linearized augmented plane wave method (LAPW) (SINGH; NORDSTROM, 2006) or the plane-augmented wave method (PAW) (BLÖCHL, 1994; KRESSE; JOUBERT, 1999). In both methods, the problem of the plane waves describing the wavefunction is firstly solved by determining a sphere with radius r_c around the atoms. Inside these spheres, the wavefunction oscillates rapidly in space due to the Coulomb potential. Outside these spheres, the wavefunction is smoother and can easily be described using plane waves.

In PAW, electrons closer to the nucleus (called "core") do not contribute to chemical bonds. Only valence electrons are responsible by these bondings. Therefore, it is possible to suppose a frozen core hypothesis to introduce a screening in the nucleus potential and leading to an effective potential to the system. This potential is then called pseudopotential.

Since states closer to the nucleus are not relevant to chemical bonds between atoms, it is possible to modify the pseudopotentials to obtain smoother wavefunctions close to them. However, they should be still identical outside this region.

The method consists in transforming the wavefunctions $|\Psi\rangle$ in pseudo-functions $|\tilde{\Psi}\rangle$ related by a transformation $\hat{\mathcal{T}}$ such that (BLÖCHL, 1994)

$$|\Psi\rangle = \hat{\mathcal{T}}|\tilde{\Psi}\rangle. \tag{2.69}$$

By hypothesis, $|\Psi\rangle$ and $|\tilde{\Psi}\rangle$ differ only for regions distant by, at most, r_c from the atoms that make the crystal. In this case, it is possible to divide the transformation $\hat{\mathcal{T}}$ in a sum of the identity operator with the transformations $\hat{\mathcal{T}}_{\mathbf{R}_k}$, where $\mathbf{R}_k$ is the position of the atomic site k. Therefore,

$$\hat{\mathcal{T}} = \hat{I} + \sum_k \hat{\mathcal{T}}_{\mathbf{R}_k}. \tag{2.70}$$

It is possible to expand the functions $|\Psi\rangle$ e $|\tilde{\Psi}\rangle$ in terms of the all-electron basis $|\psi_i\rangle$ and $|\tilde{\psi}_i\rangle$, respectively, where $|\tilde{\psi}_i\rangle = |\psi_i\rangle$ for $r > r_c$ and the generic index i designate the angular and magnetic quantum numbers, as well as the atomic sites $\mathbf{R}_k$. These bases are similar to partial waves in the region external to r_c. From this decomposed form and additional conditions, it is possible to show that the transformation $\hat{\mathcal{T}}$ can be written as (BLÖCHL, 1994)

$$\hat{\mathcal{T}} = \hat{1} + \sum_i \left(|\psi_i\rangle - |\tilde{\psi}_i\rangle\right) \langle\tilde{p}_i|, \tag{2.71}$$

with $\langle\tilde{p}_i|$ the projection function of the pseudo-function $|\tilde{\Psi}\rangle$ at the pseudo-orbital $|\tilde{\psi}_i\rangle$, obeying the condition $\langle\tilde{p}_i|\tilde{\psi}_j\rangle = \delta_{ij}$. Therefore, the true wavefunction can be written from Eqs. (2.69) and (2.71) as (BLÖCHL, 1994)

$$|\Psi\rangle = |\tilde{\Psi}\rangle + \sum_i |\psi_i\rangle\langle\tilde{p}_i|\tilde{\Psi}\rangle - \sum_i |\tilde{\psi}_i\rangle\langle\tilde{p}_i|\tilde{\Psi}\rangle, \tag{2.72}$$

usually rewritten as

$$|\Psi\rangle = |\tilde{\Psi}\rangle + |\Psi^1\rangle - |\tilde{\Psi}^1\rangle. \tag{2.73}$$

The PAW method, therefore, divides the wavefunction in three terms: (i) a pseudo-wavefunction $|\tilde{\Psi}\rangle$, related to a pseudopotential and identical to $|\Psi\rangle$ for $|\mathbf{r} - \mathbf{R}_k| > r_c$, for all k; (ii) a component $|\Psi^1\rangle$ that corrects the behavior of the wavefunction close to the

nuclei; and (iii) a component $|\tilde{\Psi}^1\rangle$ that cancel the pseudo-function on the atomic site. It is worthy of note that the original behavior of $|\Psi\rangle$ is recovered by the pseudo-function thanks to the inclusion of terms (ii) and (iii).

Other quantities of interest in the PAW method are also obtained by the division in three terms, such as the electronic density n, given by (BLÖCHL, 1994)

$$n(\mathbf{r}) = \tilde{n}(\mathbf{r}) + n^1(\mathbf{r}) - \tilde{n}^1(\mathbf{r}), \tag{2.74}$$

with $\tilde{n}(\mathbf{r})$ the pseudo-electronic density and $n^1(\mathbf{r})$ and $\tilde{n}^1(\mathbf{r})$ the electronic and pseudo-electronic densities of the real function on the atomic site, respectively. It can be shown that the effective hamiltonian operator acting on pseudo-wavefunctions is given by (BLÖCHL, 1994)

$$\hat{\tilde{H}} = \hat{T} + \hat{V}_{\text{ef}} + \sum_{i,j} |\tilde{p}_i\rangle \left(\tilde{D}_{ij} + D^1_{ij} - \tilde{D}^1_{ij}\right) \langle \tilde{p}_j|, \tag{2.75}$$

with $\hat{V}_{\text{ef}}$ an effective potential operator and $\tilde{D}_{ij}$, D^1_{ij} and $\tilde{D}^1_{ij}$ elements of division of $n(\mathbf{r})$ with respect to the functions $\tilde{n}(\mathbf{r})$, $n^1(\mathbf{r})$ and $\tilde{n}^1(\mathbf{r})$. Finally, given this effective hamiltonian, it is possible to obtain properties of interest by solving the Eq. (2.75), specially by employing the DFT.

2.5 Coincidence lattice method

First of all, 2D heterostructures can generally be fabricated with mismatch of crystal structures, lattice constants and chemical bonding. However, theoretical investigations suffer from the problem of incommensurability. During modeling, usually, small 2D supercells are assumed with a certain stacking, orientation and, in particular, some strain (KOMSA; KRASHENINNIKOV, 2013; KOLMOGOROV; CRESPI, 2005). Larger supercells, therefore with a reduced influence of these effects, increase the numerical efforts of quantum mechanical calculations within the DFT (KOHN; SHAM, 1965). Hence, a certain compromise between determination of favorable arrangements and cell size is required.

In this context, a major question arises: how to simulate van der Waals heterostructures with minimal computational costs and without incurring into unrealistic simulations due to commensurability strain? In this section, we present a method developed in this dissertation which leads to more favorable stackings when one allows for specific interlayer twists. This enables theoretical studies to explore deeper possibilities within vdW-bonded systems, effects due to interlayer twist or Moiré patterns despite limited computational

resources (WECKBECKER *et al.*, 2016). Heterostructures tailored to match experimental data can also benefit from the technique, and theoretical structures can be easily created to emulate real-world samples.

2.5.1 Methodology

We assume that the atomic geometries, i.e., the 2D Bravais lattices and the atomic basis, of the 2D crystals forming a bilayer heterostructure are known. Furthermore, we assume that the two layered systems are arranged in energetically favorable atomic positions despite their crystal structure, lattice constant and bonding mismatches. In a first step, *ab initio* calculations of the total energy should not be performed to determine the relative positions of the two crystal lattices. Rather, we start from two isolated 2D Bravais lattices with given lattice constants (from *ab initio* calculations or measurements) and follow the idea to construct a coincidence lattice with a larger unit cell from a common Bravais sublattice (BECHSTEDT; ENDERLEIN, 1988). The physical principle of this idea is the realization of a joint lattice that leaves the energy of the bilayer system smaller by enhanced bonding at the interface when compared to the general orientations and translations of the two isolated crystals.

We denote the primitive basis vectors of the Bravais lattices of the 2D crystals a and b by

$$\begin{aligned} \mathbf{R_a} &= m_1\mathbf{a}_1 + m_2\mathbf{a}_2, \\ \mathbf{R_b} &= n_1\mathbf{b}_1 + n_2\mathbf{b}_2, \end{aligned} \tag{2.76}$$

in which $m_i, n_i \in \mathbb{Z}$, $i = 1, 2$ and $\mathbf{a}_i$ and $\mathbf{b}_i$ are the primitive vectors for each of the lattices. They are characterized by one or two lattice constants of the 2D crystal and the type of the 2D Bravais lattice (KITTEL, 2004). Linear combinations of these vectors with integer coefficients yield all lattice points of the corresponding 2D Bravais lattice. The relationship between these vectors and the unit cell area is given by

$$\begin{aligned} S_\mathbf{a} &= |\mathbf{a}_1 \times \mathbf{a}_2|, \\ S_\mathbf{b} &= |\mathbf{b}_1 \times \mathbf{b}_2|. \end{aligned} \tag{2.77}$$

The primitive basis vectors $\tilde{\mathbf{a}}_i, \tilde{\mathbf{b}}_i$ of the coincidence lattice can be constructed by arbitrary linear mappings, denoted by the 2×2 matrices $\hat{M}^a$ and $\hat{M}^b$, taking into account

all possible scalings and rotations

$$\begin{aligned}\begin{bmatrix} \tilde{\mathbf{a}}_1^{\mathrm{T}} \\ \tilde{\mathbf{a}}_2^{\mathrm{T}} \end{bmatrix} &= \hat{M}^a \begin{bmatrix} \mathbf{a}_1^{\mathrm{T}} \\ \mathbf{a}_2^{\mathrm{T}} \end{bmatrix}, \\ \begin{bmatrix} \tilde{\mathbf{b}}_1^{\mathrm{T}} \\ \tilde{\mathbf{b}}_2^{\mathrm{T}} \end{bmatrix} &= \hat{M}^b \begin{bmatrix} \mathbf{b}_1^{\mathrm{T}} \\ \mathbf{b}_2^{\mathrm{T}} \end{bmatrix},\end{aligned} \tag{2.78}$$

where $\mathbf{v}^{\mathrm{T}}$ is a line vector, i.e., the transposed vector of $\mathbf{v}$.

In contrast to surface physics (BECHSTEDT, 2003), we restrict ourselves here to the case in which all elements from these transformation matrices are integer numbers in order to obtain sublattices of the original 2D Bravais lattices. Therefore, the areas of the corresponding unit cells are

$$\begin{aligned}|\tilde{\mathbf{a}}_1 \times \tilde{\mathbf{a}}_2| &= \det \hat{M}^a |\mathbf{a}_1 \times \mathbf{a}_2|, \\ |\tilde{\mathbf{b}}_1 \times \tilde{\mathbf{b}}_2| &= \det \hat{M}^b |\mathbf{b}_1 \times \mathbf{b}_2|.\end{aligned} \tag{2.79}$$

In surface physics (BECHSTEDT, 2003) one speaks about a superstructure or a reconstruction of the original surface layers, characterized by a $\hat{M}$ matrix. Instead of the matrix notation introduced in equation (2.78), in most cases it is more convenient to use the so-called Wood notation (WOOD, 1964), which relates the supercell vectors $\{\tilde{\mathbf{a}}_i,\tilde{\mathbf{b}}_i\}$ to the original ones $\{\mathbf{a}_i,\mathbf{b}_i\}$ by means of a scaling and rotation denoted as

$$\begin{aligned}&\left(\frac{|\tilde{\mathbf{a}}_1|}{|\mathbf{a}_1|} \times \frac{|\tilde{\mathbf{a}}_2|}{|\mathbf{a}_2|}\right) \mathrm{R}\phi_a, \\ &\left(\frac{|\tilde{\mathbf{b}}_1|}{|\mathbf{b}_1|} \times \frac{|\tilde{\mathbf{b}}_2|}{|\mathbf{b}_2|}\right) \mathrm{R}\phi_b,\end{aligned} \tag{2.80}$$

with

$$\begin{aligned}\phi_a &= \arccos\left(\frac{\tilde{\mathbf{a}}_1 \cdot \mathbf{a}_1}{|\tilde{\mathbf{a}}_1||\mathbf{a}_1|}\right), \\ \phi_b &= \arccos\left(\frac{\tilde{\mathbf{b}}_1 \cdot \mathbf{b}_1}{|\tilde{\mathbf{b}}_1||\mathbf{b}_1|}\right).\end{aligned} \tag{2.81}$$

Rotations and displacements of original Bravais lattices, therefore, may generate sublattices, which may be equal in the commensurate case or almost equal in the incommensurate case. The latter situation may be transformed into a commensurate case by considering the two 2D crystals slightly strained. In the commensurate limit, a coincidence lattice is

defined by the same primitive basis vectors on both sides of the heterointerface

$$\begin{aligned} \tilde{\mathbf{a}}_1 &= \tilde{\mathbf{b}}_1, \\ \tilde{\mathbf{a}}_2 &= \tilde{\mathbf{b}}_2, \end{aligned} \tag{2.82}$$

which gives identical supercells on both sides with the same area

$$|\tilde{\mathbf{a}}_1 \times \tilde{\mathbf{a}}_2| = |\tilde{\mathbf{b}}_1 \times \tilde{\mathbf{b}}_2|. \tag{2.83}$$

Such supercell contains one coincidence lattice site.

To determine this supercell, we have to find two matrices $\hat{M}^a$ and $\hat{M}^b$ that fulfill the conditions (2.82) and consequently (2.83) as

$$\hat{M}^a \begin{bmatrix} \mathbf{a}_1^{\mathrm{T}} \\ \mathbf{a}_2^{\mathrm{T}} \end{bmatrix} = \hat{M}^b \begin{bmatrix} \mathbf{b}_1^{\mathrm{T}} \\ \mathbf{b}_2^{\mathrm{T}} \end{bmatrix}. \tag{2.84}$$

The desired solution is the one which minimizes the area (2.83) of the supercell. In the incommensurate case, one requires that the conditions (2.82), (2.83) and (2.84) approximately match, so that a small strain should be applied to one or both 2D materials to obtain a commensurate situation.

In principle, one would have infinite solutions for supercells, but only use a single one which has a minimum area. Therefore, it is possible to determine the two matrices $\hat{M}^a$ and $\hat{M}^b$ and, consequently, the desired supercell for the lattices by solving the equations (2.78), (2.83) and (2.84).

In a practical approach, it is sufficient to solve this problem as a system of diophantine equations through considerations which simplify the problem for computational solutions. To derive that simpler form, let $\theta = \phi_b - \phi_a$ be the relative rotation angle between these two lattices. As we have a degree of freedom for the angle of these planar lattices due the invariance of the conjoint Bravais arrangements to rotation, i.e., a simultaneous rotation of both lattices would not interfere with the relative distances of each point of the Bravais lattice with respect to all others points in the lattice, it would be redundant specify two angles, one for each original lattice. Then, we can write a rotation matrix M to perform a relative rotation for only one of the two 2D crystals as

$$M = \begin{bmatrix} \cos\theta & \sin\theta \\ -\sin\theta & \cos\theta \end{bmatrix}. \tag{2.85}$$

We have to fulfill the requirement described in equation (2.82), which is equivalent to solve the equation (2.84). Since $\hat{M}^a$ and $\hat{M}^b$ take into account scaling and rotation,

we could solve this equation in two steps: first by fixing a given angle θ (and therefore the matrix M) and second by stating the equivalence between equation (2.84) and the coincidence $\mathbf{R_a} = M\mathbf{R_b}$, recurring to the notation from equation (2.76). If this coincidence occurs for at least three non-collinear points, this assures the existence, given the angle θ, of a supercell for the heterostructure. That is equivalent to find two non-zero and linearly independent solutions (m_1, m_2, n_1, n_2), $(m_1', m_2', n_1', n_2') \in \mathbb{Z}^4$ to the equation $\mathbf{R_a} = M\mathbf{R_b}$, which can be rewritten using a linear system notation, introduced here as

$$\underbrace{[\mathbf{a}_1\ \mathbf{a}_2]}_{A}\underbrace{\begin{bmatrix} m_1 \\ m_2 \end{bmatrix}}_{\mathbf{m}} = M\underbrace{[\mathbf{b}_1\ \mathbf{b}_2]}_{B}\underbrace{\begin{bmatrix} n_1 \\ n_2 \end{bmatrix}}_{\mathbf{n}}, \qquad A\mathbf{m} = MB\mathbf{n}. \tag{2.86}$$

The desired solution is often the one which minimizes the area of the supercell, i.e., the vectors $\mathbf{m}$ and $\mathbf{m}'$ for which the area $|(A\mathbf{m}) \times (A\mathbf{m}')|$ is minimum. That is analogous to simply finding the minimum ratio $|\mathbf{m} \times \mathbf{m}'|$ between the area of the supercell and the area of the unit cell. In this case, $|\mathbf{m}|$ and $|\mathbf{n}|$ are related to the size of the supercell compared to the size of the unit cell of the first and second 2D crystal, respectively. Using multiples of the original unit cells (e.g. a 2×2 supercell) for each one of the layer crystals would be equivalent to multiply the original solution $\mathbf{m}$ by a valid integer number. Multiplying the solution (m_1, m_2, n_1, n_2) by any non-zero integer would also return a solution for the same problem. That means, rotation and displacement of original Bravais lattices are both taken into account, just like the case described in the more general approach. The use of coincidence lattices for the simulation corresponds to the application of non-primitive unit cells in terms of the original Bravais lattice. It, therefore, does not affect the electronic properties of each individual 2D crystal. The band gap and density of states remain unchanged. Only the band structure is modified due to its folding onto a correspondingly smaller Brillouin zone. The interaction between the individual 2D crystals in a heterostructure may give rise to modifications of the electronic properties.

As fluctuations in computed lattice parameters deduced using *ab initio* calculations would almost always lead to an incommensurate case of matching, we define a tolerance related to the maximum strain we would like to apply to each of the materials, in order to turn it into a commensurate case. These solutions are given by $|A\mathbf{m} - MB\mathbf{n}| < \text{TOLERANCE}$. In this case, the strain could be distributed between the two materials for optimal simulations according to the sensitivity of each one to an applied strain. It is also useful to limit the investigation of the supercells using an integer cutoff $N_{\max}$ as a stopping criterion and hence limit the size of the supercells. More importantly, the θ angle must be specified as a parameter in this approach to impose a supercell creation with these specifications.

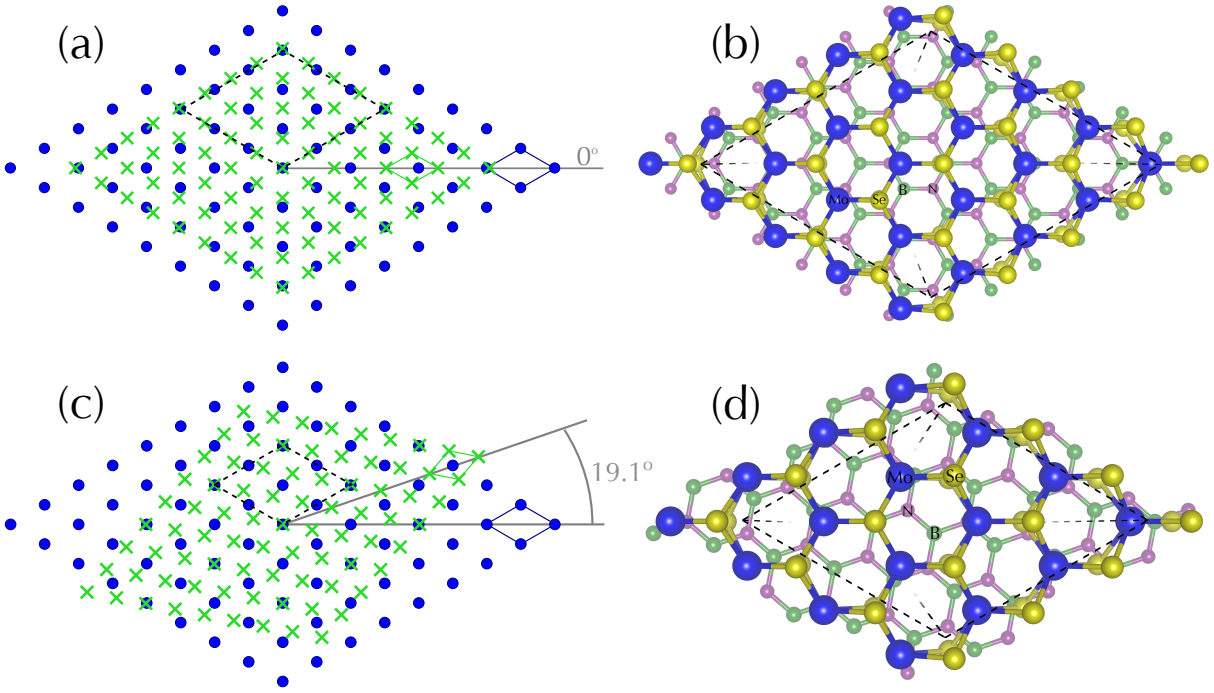

FIGURE 2.1 – Matching of the hBN Bravais lattice (green crosses) and the $MoSe_2$ lattice (blue circles) (a) without rotation and (c) rotating both lattices by 19.1° against each other. The original monolayer 1×1 unit cells are drawn with solid lines while the resulting supercell is shown with dashed lines. Atomic representations (perspective view) of the coincidence lattice method for $MoSe_2$ on top of hBN (b) without any rotation and (d) laterally rotated are also given. Molybdenum atoms are portrayed in blue, selenium atoms in yellow, boron atoms in green and nitrogen in purple.

The application of the described method is useful not only to study the changes in the electronic structure with the rotation angle by using the smallest supercell, but also in cases in which the rotation does not play a significant role. In this latter case, it may lead to higher optimizations when comparing to the supercell creation which does not consider the possibilities of rotations.

Good examples for illustration of the method are heterostructures made by two hexagonal 2D crystals, characterized by lattice constants a_a and a_b, in which the resulting coincidence lattice should also be hexagonal with a lattice constant $|\mathbf{m}|a_a = |\mathbf{n}|a_b$. To better illustrate the method, let us design a supercell of the bilayer heterostructure of hBN and molybdenum diselenide ($MoSe_2$), as depicted in Figure 2.1. With this example, we demonstrate the existence of a supercell of these two 2D crystals which is smaller when considering a relative rotation of 19.1° in comparison with a vanishing rotation between the two lattices. The latter would imply a supercell containing 59 atoms if both 2D compounds are biaxially strained by an absolute value of 0.73% (compressive for hBN and tensile for $MoSe_2$). On the other hand, applying a rotation leads to a smaller supercell, containing only 26 atoms, created with a smaller necessary strain with an absolute value of 0.33% (also compressive for hBN and tensile for $MoSe_2$) in order to make the two 2D systems

commensurate.

To this point, no considerations about total energy are made, only predictions for the resulting supercell and coincidence lattice. Therefore, for a more precise description of their energetics, the resulting heterostructures such the ones displayed in Figs. 2.1c and 2.1d should be investigated with respect to their actual energies and resulting electronic (band) structures by means of *ab initio* simulations based on total energy and electronic structure methods.

2.6 Computational Details

First-principles simulations in this work are made using the software Vienna Ab-initio Simulation Package (VASP) (KRESSE; FURTHMÜLLER, 1996a; KRESSE; FURTHMÜLLER, 1996b), within the PAW method (BLÖCHL, 1994; KRESSE; JOUBERT, 1999) to generate the wavefunctions and pseudopotentials. The software performs integrations in the 1BZ to obtain functions of interest by means of a sampling,

$$\int_{1\mathrm{BZ}} f(\mathbf{k}) d^3k \approx \sum_{\mathbf{k}} w_{\mathbf{k}} f(\mathbf{k}), \tag{2.87}$$

where $w_{\mathbf{k}}$ is a weight over the $\mathbf{k}$-points chosen in the sampling. The way with which this sampling is made is by means of Monkhorst-Pack grids (MONKHORST; PACK, 1976) centered at the $\Gamma = (0,0,0)$ point of the 1BZ. Throughout the work, this $\mathbf{k}$-point mesh is set as at least $11 \times 11 \times 1$.

The plane wave truncating parameter for the kinetic energy is given, within VASP, by a parameter named ENCUT. In this work, this ceiling to the plane waves energy is fixed at 500 eV.

Convergence criteria are such that structural relaxations occur until Hellmann-Feynman are minimized to values inferior to 1 meV/Å. The stopping criterion for the self-consistent Kohn-Sham cycle is such that the total energy variation, as well as the energy of the eigenvalues, is inferior to 10^{-5} eV.

Several functionals are employed throughout the work. Excited states are described with the functional GGA-PBE (PERDEW *et al.*, 1996; PERDEW *et al.*, 1997) within the DFT and with the hybrid functional HSE06 (HEYD *et al.*, 2003; HEYD *et al.*, 2006). vdW interaction is described with the functional optB86b (KLIMEŠ *et al.*, 2011), given its superior capability to describe structural parameters of the systems when compared to its peers (KLIMEŠ *et al.*, 2011; BJÖRKMAN, 2014).

VASP uses, in its description, periodic boundary conditions. To simulate 2D crystals,

the repetition of 2D sheets in the out-of-plane directions is made, potentially leading to long-range interactions between them. One way to prevent spurious effects on the simulation is to vary the out-of-plane lattice vector, thus inserting a vacuum separating the monolayers. Its optimal value is obtained by a careful convergence in the perpendicular direction. Although a very large vacuum reduces the interaction between adjacent layers, an excessive length leads to a larger number of plane waves in the system. The increase of the vector perpendicular to the monolayer leads to a shorter Brillouin zone. This, on its turn, requires a larger number of plane waves due to its high frequency. The vacuum length used in this work is at least 15 Å long, enough to separate adjacent layers by at least 4 monolayers.

3 Prediction of coincidence lattices

3.1 Motivation

In order to construct coincidence lattices and obtain heterostructure properties of the 2D crystals on top of each other, we need a unique database for the isolated 2D materials of interest. Experimental lattice constants suffer from different preparation and measurement techniques (KLIMEŠ *et al.*, 2011; BJÖRKMAN, 2014). Theoretical lattice constants are available for the majority of 2D materials of interest for this work (BJÖRKMAN, 2014), which are essentially hexagonal lattices with one lattice constant. However, the coincidence lattice method asks for an unified dataset. Thus, we have to repeat the calculations considering the same numerical approach with respect to XC functional energy cutoff and k-point sampling. After investigating the 2D monolayers and their lattice parameters, we employ the coincidence lattice method to find favorable lattices to be analyzed. Then, we need to refine the atomic geometries to discuss consequences on the energetics and electronic structures of the heterostructures. In this chapter, only the case of isolated monolayers and the prediction of coincidence lattices will be discussed. Using the database here refined, we validate the coincidence lattice method by comparing its results with available data from experiments and theoretical calculations. Finally, a set of interesting heterocombinations is shown for low-cost computational simulations and physical analysis.

3.2 Monolayer 2D materials

To obtain the structural parameters for the isolated sheet materials, we have employed the optB86b functional to minimize deviations from the experimental lattice parameters (KLIMEŠ *et al.*, 2011; BJÖRKMAN, 2014). This allows reasonable predictions of heterostructures, which are not influenced by fluctuations of measured values by different groups and can be fully relaxed using one and the same method. It is important to mention that the actual lattice parameters influence the electronic structure, as if the crystals are virtually strained when simulated; for instance, smaller lattice constants could lead to larger quasiparticle band gaps and vice versa (GUZMAN; STRACHAN, 2014).

Here, we focus mainly on heterostructures made by two hexagonal sheet crystals. Thereby, apart from the flat monolayers graphene and hBN, we investigate 2D crystals consisting of triple atomic layers such as TMDCs and group-IV dichalcogenides. Results for combination of such hexagonal crystals with rectangular ones, e.g. phosphorene, are discussed later. The triple-layer systems occur in different polymorphs, mainly 1T and 2H, which represent respectively octahedral (CdI_2-like) or trigonal prismatic coordination (ZHUANG; HENNIG, 2013). Phase transitions between them, sometimes accompanied by a semiconductor-metal transition as in MoS_2, may happen (LIN *et al.*, 2014). We choose here the most stable phase of a TMDC according to (ZHUANG; HENNIG, 2013). In the case of the Sn dichalcogenides, we use the energetically favorable 1T phase (WEN *et al.*, 2015), due to its experimental availability. We should remark, however, that as far as we know, WTe_2 and $TaTe_2$ have not been observed experimentally in the phase here investigated. This is due to the existence of a more stable configuration in a distorted 1T phase (LUO *et al.*, 2015; LEE *et al.*, 2015), which also alters the electronic properties of these materials. Yet, in this work, this phase transition is not taken into consideration, leading to simulations and coincidence lattice predictions for the theoretical 2H conformation phase with hexagonal Bravais lattices.

Results for the relaxed, isolated 2D materials are presented in Table 3.1. The lattice parameters are in excellent agreement with the bulk experimental values and the interchange between underestimation/overestimation has been predicted in a previous work (BJÖRKMAN, 2014). For better structural characterization of the neutral triple atomic layers, in Table 3.1 we also list the bond length between a metal (M) atom in the central atomic layer and a neighboring chalcogen (X) atom in a layer above or below the central one. The expectation that the GGA-like XC functional optB86b gives slightly overestimated lattice constants is not only fulfilled for graphene and hBN but also for dichalcogenides with VIA, VIIA and IVB elements from the periodic table. The dichalcogenides of transition metal atoms from the groups IVA and VA, however, show the opposite behavior.

For studies beyond finding coincidence lattices, such as the influence of these superstructures on the electronic properties, e.g. band alignments in corresponding heterostructures, characteristic band structure parameters of the isolated 2D crystals are also given in Table 3.1 and in Fig. 3.2. Quasiparticle effects are approximately simulated using the non-local exchange-correlation functional HSE06 (HEYD *et al.*, 2003; HEYD *et al.*, 2006). We use the HSE06 approach despite the seemingly underestimation of the quasiparticle shifts (BECHSTEDT, 2015) with respect to calculations in the framework of the GW approach (QIU *et al.*, 2013). For a given transition metal atom there is a clear trend with the chalcogen atom. The fundamental gaps (in the case of a semiconducting phase) become smaller along the column S $\rightarrow$ Se $\rightarrow$ Te. The $3d$, $4d$ and $5d$ transition metal cations have also a significant influence. In the case of group VB elements and for Ti there is a clear

TABLE 3.1 – Structural and electronic properties of selected monolayer 2D crystals. The lattice parameter (a) and the bond length (d_{MX}) are calculated with the optB86b functional, whereas the band gap (E_{g}) is obtained from a subsequent HSE06 calculation. The ionization energy (I) and electron affinity (A) are referred to the vacuum level. Experimental lattice parameters (a_{exp}) are taken from the collection from Björkman (2014), Gronvold *et al.* (1960), Madelung *et al.* (1998). The most stable polymorph according to Zhuang e Hennig (2013), 1T or 2H, is studied.

	a (Å)	a_{exp} (Å)	d_{MX} (Å)	E_{g} (eV)	A (eV)	I (eV)
Graphene	2.467	2.456	1.42	0	4.330	4.330
hBN	2.512	2.510	1.45	5.79	0.941	6.735
HfS_2 (1T)	3.626	3.635	2.55	2.03	4.925	6.956
$HfSe_2$ (1T)	3.734	3.748	2.67	1.18	4.829	6.008
$HfTe_2$ (1T)	3.920	3.957	2.88	Semimetal	4.670	4.670
MoS_2 (2H)	3.164	3.162	2.41	2.25	4.025	6.270
$MoSe_2$ (2H)	3.301	3.289	2.54	1.95	3.735	5.685
$MoTe_2$ (2H)	3.528	3.518	2.73	1.57	3.558	5.123
NbS_2 (2H)	3.340	3.310	2.49	Metal	6.202	6.202
$NbSe_2$ (2H)	3.641	3.442	2.62	Metal	5.847	5.847
$NbTe_2$ (2H)	3.663	3.680	2.81	Metal	5.150	5.150
PtS_2 (1T)	3.566	3.542	2.40	2.64	4.355	6.992
$PtSe_2$ (1T)	3.728	3.727	2.53	1.91	4.218	6.129
$PtTe_2$ (1T)	3.988	4.026	2.70	1.08	3.913	4.990
SnS_2 (1T)	3.667	3.648	2.59	2.36	4.955	7.315
$SnSe_2$ (1T)	3.831	3.811	2.73	1.38	5.112	6.493
TaS_2 (2H)	3.321	3.364	2.48	Metal	6.024	6.024
$TaSe_2$ (2H)	3.449	3.476	2.63	Metal	5.432	5.432
$TaTe_2$ (2H)	3.674	–	2.80	Metal	5.026	5.026
TiS_2 (1T)	3.375	3.409	2.42	0.47	5.559	6.029
$TiSe_2$ (1T)	3.499	3.536	2.55	Semimetal	5.213	5.213
$TiTe_2$ (1T)	3.705	3.777	2.76	Metal	4.777	4.777
VS_2 (1T)	3.153	3.221	2.34	Metal	5.482	5.482
VSe_2 (1T)	3.305	3.358	2.48	Metal	5.256	5.256
WS_2 (2H)	3.182	3.153	2.43	2.29	3.782	6.073
WSe_2 (2H)	3.296	3.282	2.54	2.11	3.325	5.430
WTe_2 (2H)	3.527	–	2.73	1.52	3.395	4.918
ZrS_2 (1T)	3.650	3.662	2.57	1.85	5.138	6.989
$ZrSe_2$ (1T)	3.768	3.770	2.69	1.10	4.996	6.091
$ZrTe_2$ (1T)	3.926	3.952	2.90	Semimetal	4.839	4.839

tendency for a metallic behavior independent of the 1T or 2H polymorph. We also list the electron affinity A and the ionization potential I for the 2D crystals, given by

$$A = \varepsilon_{\text{vac}} - \varepsilon_c, \tag{3.1}$$

$$I = \varepsilon_{\text{vac}} - \varepsilon_v. \tag{3.2}$$

The description of the surface barriers of the 2D crystals with respect to the vacuum level ε_{vac} has been determined as the plateau of the electrostatic potential between the material slabs (BECHSTEDT, 2003). Their values will be used later to determine natural band discontinuities between two 2D crystals via a vacuum-level alignment for the purpose of comparison.

Differences between the ionization potential and the electron affinity characterize the fundamental quasiparticle energy gaps

$$E_g = I - A, \tag{3.3}$$

in which excitonic effects are not taken into account. The optical and quasiparticle band gaps differ by the exciton binding energy, as shown in Fig. 3.1. In 2D semiconductors and insulators, strongly-bound excitons are observed, leading to pronounced differences between the two aforementioned band gaps.

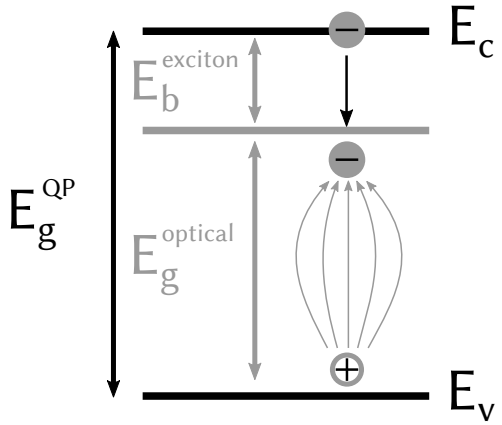

FIGURE 3.1 – Depiction of the quasiparticle energy gap (E_g^{QP}) and the optical energy gap ($E_g^{\text{ótico}}$), which differ by the exciton binding energy ($E_b^{\text{éxciton}}$). Energies from the VBM (E_v) and the CBM (E_c) are also shown.

All calculations resulting in Table 3.1 have been performed using primitive unit cells of the 2D crystals. Later, in the case of bilayer heterostructures with coincidence lattices, however, larger non-primitive unit cells are investigated. As a consequence, also in the limit of vanishing interlayer interactions, smaller Brillouin zones are considered, resulting in folded band structures.

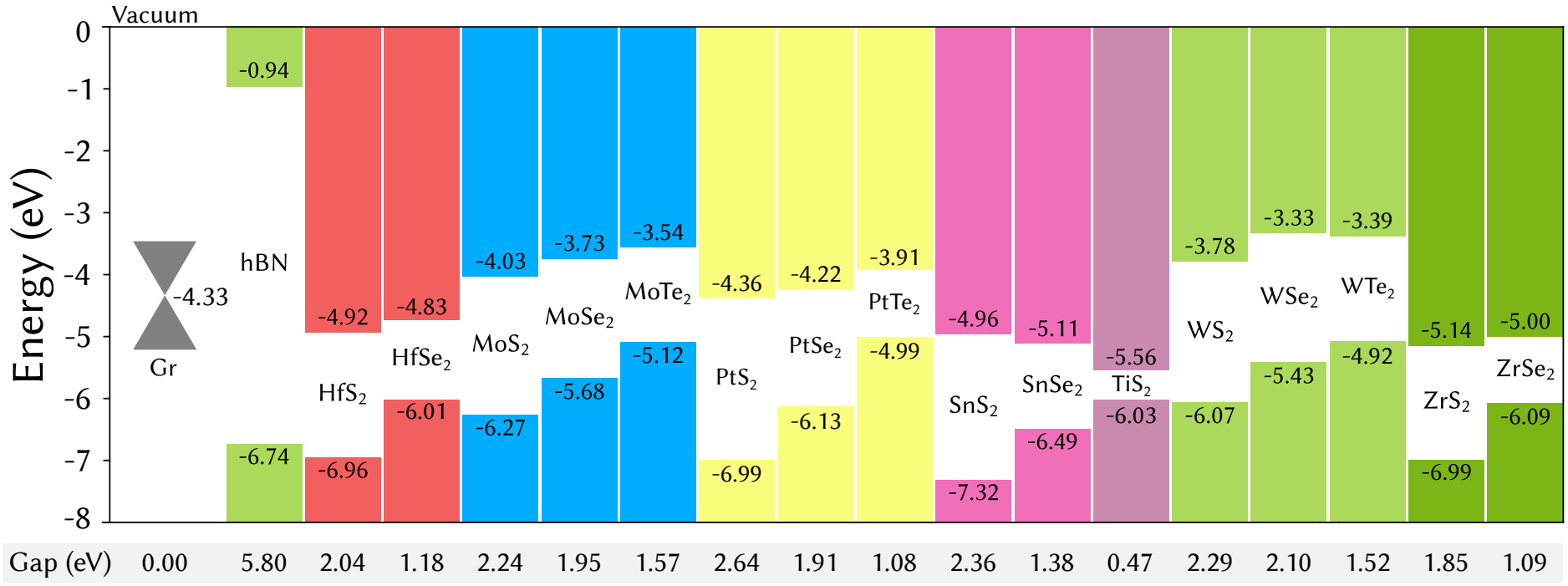

FIGURE 3.2 – Conduction and valence band edges calculated within HSE06 for all semiconductor 2D crystals displayed in Tab. 3.1. The colored bar edges represent the valence band maximum and the conduction band minimum for each monolayer, while the Dirac cone vertex characterizes the Fermi level for graphene. All energies are given in eV and are taken with respect to the vacuum level.

3.3 Validation of the coincidence lattice method

Using the calculated lattice parameters in Table 3.1 for the investigated monolayer 2D materials and the procedure described in the coincidence lattice method section, we predict the coincidence lattices of almost strain-free 2D crystals in vdW bonded heterostructures. Special care is taken for the supercell of the coincidence lattice, which is expressed by a superstructure of each of the two 2D crystals combined. Essentially the results are presented using the Wood notation in the form shown in Eq. (2.80) whenever the heterostructure is formed by two hexagonal lattices. In these cases, the heterointerface can be described using the common surface physics representation. That denotation is dropped when we deal with rectangular lattices, which are better described with the original matrix notation from Eq. (2.78). Then, the construction of the supercell is possible just by applying a commensurability strain and stacking both sheet crystals following the orientation shown, similar to the specifications in surface physics (BECHSTEDT, 2003).

In the majority of combinations, each heterostructure possesses a small strain, which is related to the conversion of its incommensurate matching into a commensurate one by modifying the original lattice parameters by their relative value to obtain approximate solutions of equation (2.86). In the case of the hexagonal lattices, this value represents the biaxial strain which has to be applied to the primitive basis vectors of both monolayers if this strain is assumed to be distributed equally in magnitude to both layers. This information can be easily retrieved if we have the solution (**m**,**n**) from equation (2.86), which gives us the length of the supercell vectors relative to the original vectors. Therefore, the biaxial strain $\varepsilon = \varepsilon_{\mathrm{x}} = \varepsilon_{\mathrm{y}}$ is obtained straining both compounds to match the same supercell lattice parameter, i.e., from

$$\begin{aligned} (1+\varepsilon)|\mathbf{Am}| &= (1-\varepsilon)|\mathbf{Bn}|, \\ \varepsilon &= \frac{|\mathbf{Bn}| - |\mathbf{Am}|}{|\mathbf{Bn}| + |\mathbf{Am}|}. \end{aligned} \tag{3.4}$$

The application of the strain can be conditioned, when creating the supercell accordingly, to the elastic constants of each separated sheet crystal. In this way, more sensitive materials could be submitted to a smaller strain in order to minimize changes in the band structure of the constituents of the resulting heterostructure.

The results of the coincidence lattice method described above for all the combinations of hexagonal crystals given in Table 3.1 are summarized in Table S1 of the Supporting Information from Koda *et al.* (2016). Despite our limitations to a biaxial strain $\varepsilon < 0.01$ and an unit cell size of the heterostructure with a number of atoms $N \leq 100$ in Table S1 (KODA *et al.*, 2016), more than 700 different combinations described by pairs of Wood notations for the two crystals forming the heterosystems are listed. This variety of bilayers

is too large to discuss here. In order to demonstrate the applicability of the general procedure, we first focus on the discussion of heterostructures reported experimentally or in other theoretical works. Thereby, the strain in these vdW-bonded heterostructures is only discussed based on the lattice constants given in Table 3.1. Furthermore, in a few more cases we also discuss supercell sizes with $N > 100$, in order to compare the size of the derived supercells with experimentally observed Moiré patterns, which represent long-range periodicities in the real space. These patterns can easily be treated within the proposed approach. Our predictions for such already studied systems are listed in Table 3.2. In general, the presented supercells show agreement with those results obtained by other, experimental and theoretical, methods adopted in previous papers concerning structural terms. No total energy calculations, however, have been performed for these bilayer systems. All predictions are based on the coincidence lattice method.

Superior examples for the success of the coincidence lattice method are explored. Indeed, the Moiré pattern predicted for a twisted ($\theta = 3.3°$ in Table 3.2) bilayer of graphene is in agreement with experimental findings (BRIHUEGA *et al.*, 2012). The Moiré pattern and its supercell are represented in Fig. 3.3. The calculated long-range periodicity with 1202 carbon atoms in the supercell gives a lattice constant of 4.27 nm, in good agreement with the measured value of 4.3 nm (BRIHUEGA *et al.*, 2012). In Table 3.1, a similar agreement is found for graphene on hexagonal BN assuming a strain-free situation, despite the fact that the lattice constant of the supercell is much larger, equal to 13.8 nm (SLOTMAN *et al.*, 2015). Applying the coincidence lattice method with two different strain parameters, we find a perfect agreement with another theoretical work (SLOTMAN *et al.*, 2015). We also find that a smaller pattern could be formed if a small strain is allowed in both 2D crystals. Other experimental results for the graphene/hBN system can be explained by the coincidence lattice method. Allowing larger cells of coincidence lattices, our method predicts a Moiré wavelength of 12.4 nm for an interlayer twist of 0.5°, very similar to experimental values around a length of 12.3 nm (TANG *et al.*, 2013; WANG *et al.*, 2016a). A reasonable agreement with the size of the formed superlattice can be also noted for the MoS_2/WSe_2 heterobilayer, in which the measurement range is of four to six times the lattice constants of the monolayers (FANG *et al.*, 2014). The calculated lattice constant of 1.45 nm is close to the value derived from the experiment. Coincidences motivated by experimental results are also found for the bilayer MoS_2 (HUANG *et al.*, 2014). The bilayer MoS_2 twisted by 27.8° has a perfect coincidence lattice, due to the equivalence of the lattice parameters, with 78 atoms inside the supercell. The two values are in agreement with the analysis made by Huang and coworkers (HUANG *et al.*, 2014). The experimental stacking with a twist of 51.5° can be also explained within the coincidence lattice method and calculated lattice parameters, but only with a induced 2.44% strain on each layer.

In addition to the comparison with measured data, one can also compare with supercells

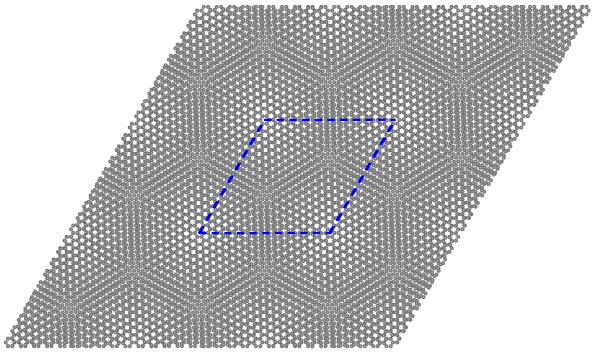

FIGURE 3.3 – Theoretical Moiré pattern for a twisted bilayer graphene rotated by 3.3° with respect to each other. The lattice parameter of the unit cell, represented in blue dashed lines, is 4.27 nm, in agreement with the experimental result (BRIHUEGA *et al.*, 2012). Carbon atoms are depicted as gray circles, and their spatial distribution leads to bright spots, indicating atoms aligned in the stacking direction, and darker regions, where atoms from one layer fill the empty spots from the other.

applied in total energy calculations. For the bilayer heterostructures studied in Refs. Komsa e Krasheninnikov (2013), Wang *et al.* (2015), we predict different possibilities with varying supercell size, biaxial strain and twisting angle. Corresponding results are also listed in Table 3.2. The graphene/MoS_2 heterobilayers from Ref. Wang *et al.* (2015) demonstrate that the size of the proposed heterostructures is almost the same in terms of relative scaling for each rotation angle. Differences between the two predicted strains can be attributed to lattice optimizations, whose deviations result in varying lattice mismatches. Finally, the *ab initio* predictions for bilayer heterosystems of MoS_2 with other TMDCs but also graphene and hBN (KOMSA; KRASHENINNIKOV, 2013) are in agreement with the assortment of supercells derived by our method. However, the coincidence lattice method also finds smaller cells with reasonable strains and less atoms inside the resulting supercell, also as a result of variation of the optimized lattice parameters and the assumption of equally distributed strain.

3.4 Favorable coincidence lattices

For further illustration of the coincidence lattice method, a selected set of our findings for commensurable heterostructures with small strains and supercell sizes are listed in Table 3.3. All combinations reported in this table are a subset from the more than 700 cases reported in Table S1 from Koda *et al.* (2016). All heterostructures analyzed throughout this work are displayed in Tab. 3.3 or, in the case of phosphorene-based heterostructures, in the text.

The coincidence lattices predicted for combinations of two 2D hexagonal crystals in Table 3.3 illustrate the huge variety of possibilities for investigating heterobilayers made

TABLE 3.2 – Coincidence lattice predictions of supercells for systems studied in the literature (KOMSA; KRASHENINNIKOV, 2013; BRIHUEGA *et al.*, 2012; WANG *et al.*, 2015; HUANG *et al.*, 2014; FANG *et al.*, 2014). The column labeled as layer 1/2 relates the original monolayer unit cell in Wood notation (BECHSTEDT, 2003; WOOD, 1964) to the supercell used in the heterostructure, rotated by an angle θ with respect to each other. The first compound shown in the heterobilayer column is denoted as layer 1. The predicted number N of atoms inside the supercell and the equally-distributed biaxial strain ε also characterize the building of the supercell. All lattice parameters used were the ones from this work's optimizations. The $\pm$ sign indicates a tensile strain used on the layer 1 and a compression strain on the layer 2, and vice-versa for the $\mp$ sign.

Heterobilayer	Layer 1	Layer 2	θ	N	ε (%)
Experimental bilayer graphene Moiré patterns (as in Ref. Brihuega et al. (2012)):					
Gr/Gr	$(\sqrt{300} \times \sqrt{300})$ R 30.0°	$(\sqrt{301} \times \sqrt{301})$ R 3.3°	3.3°	1202	$\pm$0.08
Gr/Gr	$(\sqrt{91} \times \sqrt{91})$ R 27.0°	$(\sqrt{91} \times \sqrt{91})$ R 27.0°	6.0°	364	$\pm$0.00
Gr/Gr	$(\sqrt{37} \times \sqrt{37})$ R 25.3°	$(\sqrt{37} \times \sqrt{37})$ R 25.3°	9.4°	148	$\pm$0.00
Theoretical Moiré patterns of graphene on top of hBN (as in Ref. Slotman et al. (2015)):					
Gr/hBN	56×56	55×55	0.0°	12322	$\pm$0.00
Gr/hBN	37×37	36×36	0.0°	5330	$\mp$0.47
Experimental WSe_2/MoS_2 heterobilayer (as in Ref. Fang et al. (2014)):					
WSe_2/MoS_2	$(\sqrt{19} \times \sqrt{19})$ R 23.4°	$(\sqrt{21} \times \sqrt{21})$ R 10.9°	12.5°	120	$\pm$0.46
Theoretical graphene/MoS_2 heterobilayers (as in Ref. Wang et al. (2015)):					
Gr/MoS_2	$(\sqrt{21} \times \sqrt{21})$ R 10.9°	$(\sqrt{13} \times \sqrt{13})$ R 13.9°	3.0°	81	$\pm$0.45
Gr/MoS_2	$(\sqrt{43} \times \sqrt{43})$ R 7.6°	5×5	7.6°	161	$\mp$1.12
Gr/MoS_2	$(\sqrt{39} \times \sqrt{39})$ R 16.1°	5×5	16.1°	153	$\pm$1.32
Gr/MoS_2	$(\sqrt{7} \times \sqrt{7})$ R 19.1°	2×2	19.1°	26	$\mp$1.55
Gr/MoS_2	$(\sqrt{21} \times \sqrt{21})$ R 10.9°	$(\sqrt{13} \times \sqrt{13})$ R 13.9°	24.8°	81	$\pm$0.45
Gr/MoS_2	8×8	$(\sqrt{37} \times \sqrt{37})$ R 25.3°	25.3°	239	$\mp$1.26
Experimental MoS_2 bilayers (as in Ref. Huang et al. (2014)):					
MoS_2/MoS_2	$(\sqrt{13} \times \sqrt{13})$ R 13.9°	$(\sqrt{13} \times \sqrt{13})$ R 13.9°	27.8°	78	$\pm$0.00
MoS_2/MoS_2	$(\sqrt{39} \times \sqrt{39})$ R 16.1°	$(\sqrt{43} \times \sqrt{43})$ R 7.6°	51.5°	246	$\pm$2.44
Theoretical heterobilayers with MoS_2 (as in Ref. Komsa e Krasheninnikov (2013)):					
MoS_2/WS_2	1×1	1×1	0.0°	6	$\pm$0.28
MoS_2/hBN	$(\sqrt{13} \times \sqrt{13})$ R 13.9°	$(\sqrt{21} \times \sqrt{21})$ R 10.9°	3.0°	81	$\pm$0.45
$MoS_2/MoTe_2$	4×4	$(\sqrt{13} \times \sqrt{13})$ R 13.9°	13.9°	87	$\pm$0.25
$MoS_2/MoSe_2$	$(\sqrt{13} \times \sqrt{13})$ R 13.9°	$(\sqrt{12} \times \sqrt{12})$ R 30.0°	16.1°	75	$\pm$0.12
MoS_2/Gr	4×4	$(\sqrt{27} \times \sqrt{27})$ R 30.0°	30.0°	102	$\pm$0.64
Our predictions for smaller systems among the ones from Ref. Komsa e Krasheninnikov (2013):					
MoS_2/Gr	$(\sqrt{13} \times \sqrt{13})$ R 13.9°	$(\sqrt{21} \times \sqrt{21})$ R 10.9°	3.0°	81	$\mp$0.45
MoS_2/hBN	$(\sqrt{12} \times \sqrt{12})$ R 30.0°	$(\sqrt{19} \times \sqrt{19})$ R 23.4°	6.6°	74	$\mp$0.05
$MoS_2/MoTe_2$	3×3	$(\sqrt{7} \times \sqrt{7})$ R 19.1°	19.1°	48	$\mp$0.84

of graphene and transition metal/group-IV dichalcogenides without great computational efforts. Intriguing investigations of TMDCs heterobilayers are also feasible with reduced numerical cost. The characteristic twist angles shown in the table, e.g. 0.0°, 30.0° and 19.1°, are due to the matching of the smaller lengths possible between two lattice points in a hexagonal lattice (e.g. see Fig. 2.1). Most trivial cases, like combinations of the type (1×1) R 0°, are excluded in this succinct version of the table. Rotations with redundant

angles are also not shown. Since the rotation of a hexagonal lattice by multiples of 60° is symmetry conserving, we only investigate relative rotations that lie within the interval [0°, 30°], as rotating the hexagonal cell by $30° + \varphi$, $\varphi \in [0°,30°]$, is equivalent to rotating the cell by $-30° + \varphi$.

TABLE 3.3 – Favorable predictions of combinations of hexagonal crystals based on the coincidence lattice method. The "Layer 1/2" column relates the original monolayer unit cell to the supercell used in the heterostructure, rotated by an angle θ with respect to each other. The first compound shown in the heterobilayer column is denoted as layer 1. The predicted number N of atoms inside the supercell and the equally distributed biaxial strain ε also characterize the building of the supercell. The $\pm$ sign indicates a tensile strain applied on the layer 1 and a compressive strain on the layer 2, and vice versa for the $\mp$ sign. Only a set of the supercells available from this work are displayed.

Heterobilayer	Layer 1	Layer 2	θ	N	ε (%)
Gr/$MoSe_2$	$(\sqrt{7} \times \sqrt{7})$ R 19.1°	2×2	19.1°	26	$\pm$0.57
Gr/SnS_2	3×3	2×2	0.0°	30	$\mp$0.45
Gr/$SnSe_2$	3×3	2×2	0.0°	30	$\pm$1.73
Gr/WSe_2	$(\sqrt{7} \times \sqrt{7})$ R 19.1°	2×2	19.1°	26	$\pm$0.49
Gr/ZrS_2	3×3	2×2	0.0°	30	$\mp$0.69
Gr/$ZrSe_2$	$(\sqrt{7} \times \sqrt{7})$ R 19.1°	$(\sqrt{3} \times \sqrt{3})$ R 30.0°	10.9°	23	$\mp$0.01
hBN/$MoSe_2$	$(\sqrt{7} \times \sqrt{7})$ R 19.1°	2×2	19.1°	26	$\mp$0.33
hBN/$MoSe_2$	$(\sqrt{12} \times \sqrt{12})$ R 30.0°	$(\sqrt{7} \times \sqrt{7})$ R 19.1°	10.9°	45	$\pm$0.18
hBN/$MoSe_2$	4×4	3×3	0.0°	59	$\mp$0.73
hBN/$SnSe_2$	$(\sqrt{7} \times \sqrt{7})$ R 19.1°	$(\sqrt{3} \times \sqrt{3})$ R 30.0°	10.9°	23	$\mp$0.08
HfS_2/MoS_2	$(\sqrt{3} \times \sqrt{3})$ R 30.0°	2×2	30.0°	21	$\pm$0.35
HfS_2/SnS_2	1×1	1×1	0.0°	6	$\pm$0.56
HfS_2/ZrS_2	1×1	1×1	0.0°	6	$\pm$0.33
MoS_2/SnS_2	2×2	$(\sqrt{3} \times \sqrt{3})$ R 30.0°	30.0°	21	$\pm$0.22
MoS_2/ZrS_2	2×2	$(\sqrt{3} \times \sqrt{3})$ R 30.0°	30.0°	21	$\mp$0.02
$MoSe_2$/$SnSe_2$	2×2	$(\sqrt{3} \times \sqrt{3})$ R 30.0°	30.0°	21	$\pm$0.25
SnS_2/WS_2	$(\sqrt{3} \times \sqrt{3})$ R 30.0°	2×2	30.0°	21	$\pm$0.10
SnS_2/ZrS_2	1×1	1×1	0.0°	6	$\mp$0.23
$SnSe_2$/WSe_2	$(\sqrt{3} \times \sqrt{3})$ R 30.0°	2×2	30.0°	21	$\mp$0.33
$SnSe_2$/$ZrSe_2$	1×1	1×1	0.0°	6	$\mp$0.83

It is important to note that no information about the stacking order or in-plane translations are made in Tables 3.1, 3.2, and 3.3, as we start from the primitive hexagonal Bravais lattices and do not take the atomic basis of a given 2D crystal into account. Moreover, the stacking order could alter the final geometry under rotations. For instance, for graphene-like materials a AA stacking would become a AB stacking order under a 60° rotation. Also, fractional planar translations of each monolayer system with atoms could alter the stability of the heteroconfiguration. Corresponding space-group operation can be easily done by displacing the atoms inside the original unit cells of the 2D crystals which

form the bilayer system. Thus, precise conclusions of system stability require total energy calculations of the complete atomic arrangements having in mind that our listed lattice matchings do not explore directly the possible stackings because only Bravais lattices are studied. This is only possible if the atoms are really taken into consideration, as in explicit total energy calculations.

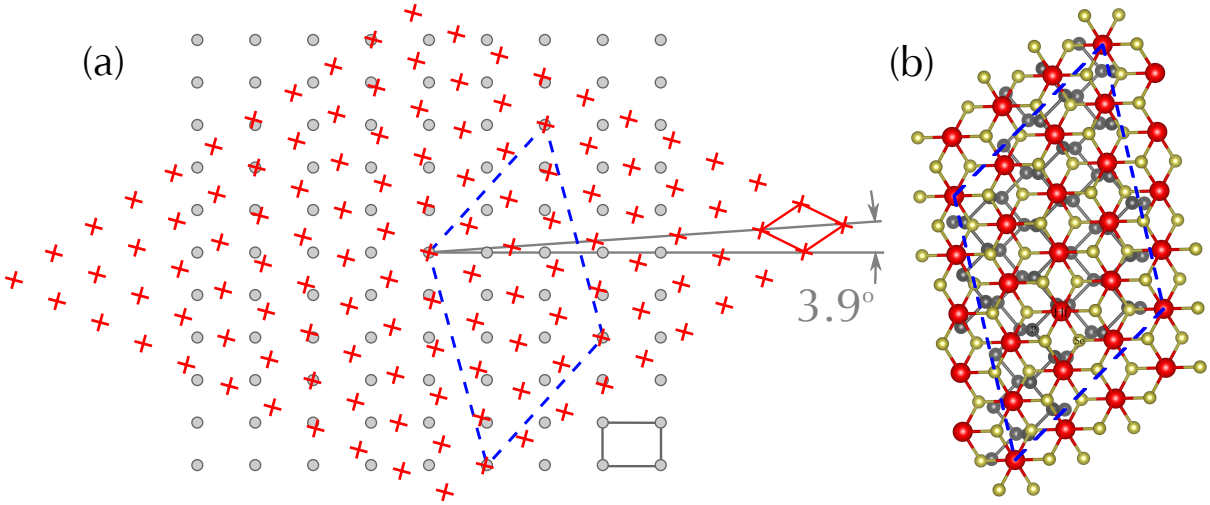

FIGURE 3.4 – (a) Matching of a $HfSe_2$ hexagonal lattice (red crosses) and a phosphorene rectangular lattice (gray circles) rotated by 3.9° against each other. The original unit cells are drawn with solid lines and the supercell is described by dashed lines. (b) Supercell of the heterostructure with atomic basis. Hafnium, selenium and phosphorus atoms are displayed in red, yellow and gray, respectively.

Until now only combinations of two hexagonal crystals have been investigated. However, the coincidence lattice method presented above can be applied to arbitrary 2D Bravais lattices (BECHSTEDT; ENDERLEIN, 1988; KITTEL, 2004). As an example in which two Bravais lattices with different shape of the primitive cells are used, we inspect the possibility to build coincidence lattices from a rectangular 2D Bravais lattice and a hexagonal one using the approach suggested here. The rectangular lattice was adopted from a 2D phosphorene crystal (LIU *et al.*, 2014), whose orthogonal vectors are found to have the lengths of 4.504 Å (armchair direction) and 3.305 Å (zigzag direction) within the DFT-optB86b total energy optimization described earlier. Many combinations with a hexagonal 2D crystal are possible. An illustration of the great action of the coincidence lattice method applied to different Bravais lattices is a heterostructure of $HfSe_2$ on top of phosphorene, whose Bravais and coincidence lattices are shown in Figure 3.4. In this case, the $HfSe_2$ layer is rotated by 3.9° with respect to the phosphorene armchair orientation and the commensurability is obtained by applying a non-uniform in-plane strain smaller than 1%. In the case of a rectangular/hexagonal combination, however, the resulting strain is not biaxial anymore because the shape of the supercell is different from that of the original ones. Rather, besides different uniaxial strains in x and y direction, a shear strain appears. One has, therefore, to handle the full 2×2 in-plane deformation tensor $\hat{\varepsilon}$. Consequently,

instead of the simplified Wood notation, the representation of the heterojunction basis asks for the use of the matrix notation, resulting

$$\hat{M}^{\mathrm{Ph}} \begin{bmatrix} \mathbf{a}_1^{\mathrm{T}} \\ \mathbf{a}_2^{\mathrm{T}} \end{bmatrix} = \begin{bmatrix} 1 & -5 \\ 2 & 3 \end{bmatrix} \begin{bmatrix} 4.504\ \mathring{\mathrm{A}} & 0 \\ 0 & 3.305\ \mathring{\mathrm{A}} \end{bmatrix} \tag{3.5}$$

with $\{\mathbf{a}_1, \mathbf{a}_2\}$ the primitive vector basis of the phosphorene rectangular lattice. The resulting superlattice is characterized by the matrix $\hat{M}^a$ from Eq. (3.5).

In this dissertation, we also explore the case of phosphorene stacked on top of $MoSe_2$ and WSe_2. This coincidence lattice leads to a transformation matrix for the phosphorene layer represented by

$$\hat{M}^{\mathrm{Ph}} \begin{bmatrix} \mathbf{a}_1^{\mathrm{T}} \\ \mathbf{a}_2^{\mathrm{T}} \end{bmatrix} = \begin{bmatrix} 5 & 0 \\ 0 & 1 \end{bmatrix} \begin{bmatrix} 4.504\ \mathring{\mathrm{A}} & 0 \\ 0 & 3.305\ \mathring{\mathrm{A}} \end{bmatrix}. \tag{3.6}$$

4 Influences of stacking and rotation on band alignments

4.1 Motivation

Despite the feasible preparation of vdW heterostructures by means of exfoliated 2D layers from vdW-bonded three-dimensional layered crystals, resizing of the two lattices, their relative orientation, stacking, and strain effects are capable of changing the electronic properties of 2D crystals (WANG *et al.*, 2015; ZANDE *et al.*, 2014). These influences become more important when considering the epitaxial growth of one layer on the other one, e.g. the vdW epitaxy of TMDC monolayers on graphene for which a preferential orientation among the layers have been found (SHI *et al.*, 2012). Effects such as stacking, interlayer twist and incommensurability may induce changes into structural and electronic properties of the system (WOODS *et al.*, 2014; SHI *et al.*, 2012). Therefore, structure-induced effects on the interface formation and the electronic structure alignment cannot be overlooked.

For the determination of the actual atomic geometry in a bilayer heterostructure, the presented coincidence lattice method has to be combined with DFT total energy calculations using the constructed supercells listed in Tables 3.2 and 3.3. First, to analyze effects of stacking on vdW heterostructures, we apply the combined methods to heterobilayer sulfide systems for three examples, also listed in Table 3.3: (i) a simple, almost lattice-matched heterostructure of HfS_2 and ZrS_2, to illustrate the effect of stacking on the binding energy and interlayer distance, (ii) a heterostructure built from MoS_2 and HfS_2 rotated by 30° against each other, and (iii) a similar heterostructure made by MoS_2 and ZrS_2 rotated by 30° against each other.

Stacking is not the only structural factor that may influence the energetics of vdW heterostructures, however. Due to the weak interlayer interaction and the 2D nature of the crystals itself, an additional degree of freedom is found within interlayer twists. Not all bilayer systems, however, are computationally favorable to be simulated from supercells with different interlayer twist angles, since coincidence lattices are strongly dependent of

the lattice mismatch between the monolayer 2D crystals. To understand how does the interlayer twist influences the electronic properties of a heterobilayer system, we select a single bilayer to be studied predicted using the coincidence lattice method. In this case, heterostructures of hBN/$MoSe_2$ twisted bilayer systems are found to be favorable.

Simulations of the structural properties of different stacks of the lattice-matched heterobilayers are first discussed in Sec. 4.2. Then, effects of the stacking on the electronic properties of the materials are investigated in Sec. 4.3. Afterwards, the same structural and electronic analysis is made for the lattice-mismatched TMDC bilayers, as well as the reasons behind the modification of their properties 4.4. Then, we proceed to the investigation of interlayer twist on vdW heterostructures. Simulations of the structural properties of hBN/$MoSe_2$ are given in Sec. 4.5, followed by an analysis of the influences of the interlayer twist on the electronic properties of the bilayers in Sec. 4.6.

4.2 Effects of stacking on structural properties of bilayers

The simplest case investigated is the almost lattice-matched HfS_2 and ZrS_2 heterobilayer system. In order to test the strain influence on isolated layers, we studied the maximum 0.66% biaxial strain on HfS_2. However, no significant changes have been observed in the electronic properties of this material, as expected from previous studies (GUZMAN; STRACHAN, 2014). Therefore, only weak strain-induced modifications are expected for the behavior of the bilayer system. We investigated four different stackings possible for the HfS_2/ZrS_2 bilayer arrangement with 1T-structure layers, T, C7, C27 and AA (KOŚMIDER; FERNÁNDEZ-ROSSIER, 2013), thereby keeping the original 1×1 translational symmetry (refer to Table 3.3). The influence of the stacking on interlayer separation, in-plane translations, and binding energy is of interest. The stacking geometries (top and side views) are depicted in Fig. 4.1a. The energetics of the bilayer system versus the interlayer distance and the relative lateral displacement of the two 2D crystals are illustrated in Fig. 4.1b and Fig. 4.1c, respectively.

The stability for bilayer systems throughout this work is investigated first by varying the interlayer distance and obtaining the energy as a function of the separation while keeping the atoms fixed in their positions within the monolayers. The binding energy E_b is given by

$$E_b = \frac{(E_1 + E_2) - E_{\text{het}}}{A_{\text{supercell}}}, \tag{4.1}$$

in which E_{het} is the total energy of the heterobilayer for a given interlayer distance, E_1 and

E_2 are the energies of the strained and isolated layers 1 and 2 that form the heterostructure considering their atomic positions, and $A_{\text{supercell}}$ is the area of the supercell. Therefore, no contribution due to the elastic energy is included in the binding energy, and the binding energy curve only takes into account the contact energy to analyze effects of rotation into the weak vdW binding.

In the case of the lattice-matched heterostructures, the plot of binding energy versus distance between HfS_2 and ZrS_2 in Fig. 4.1b show that the stackings AA, C7 and T are more stable than the C27 configuration. This results in a smaller interlayer distance of about 3.0 Å compared to the 3.5 Å in the C27 case. However, despite the fixed coincidence lattice, also the relative lateral atomic arrangements influence the stability of the bilayer systems. Small in-plane displacements executed, keeping constant the interlayer distance of AA and C7 stackings of the two 2D crystals 1T-HfS_2 and 1T-ZrS_2, demonstrate in Fig. 4.1c the local stability of these arrangements, contrary to the C27 one. The total energy curves do not exhibit pronounced minima and the stackings are not very rigid. The T stacking can be turned into a AA stacking with a significant displacement in the $[\bar{1}100]$ direction, which also lowers the equilibrium interlayer distance (compare the two structures in Fig. 4.1a) and explains the absence of a local energy minimum for this stacking. Total force calculations indicate that repulsion between close sulfur atoms make the C27 configuration unstable against in-plane shifts in the $[\bar{1}100]$ direction. The calculated binding energies lie between 15.6 meV/Å^2 and 22.2 meV/Å^2, values which are very reasonable energies for vdW-bonded TMDCs bilayers (BJÖRKMAN *et al.*, 2012). The stability of even the least energetically favorable stacking, therefore, is in agreement with the success of the preparation of such vdW-bonded heterostructures in several experiments. The weak vdW bonding and the formation of coincidence lattices allow the easy preparation of stacked heterostructures from exfoliated 2D materials despite mismatch in the lattice constants, bonding and even crystal structure.

4.3 Effects of stacking on electronic properties of bilayers

The influence of the actual stacking and atomic geometry of the heterostructure on the electronic structure has been studied by means of the band structure and the alignment of the electronic states of the two isolated 2D crystals in the heterocombination. For illustration of this geometric influence, the corresponding band structures are calculated for the four stackings of HfS_2/ZrS_2. As an example, that of the AA stacking is displayed in Fig. 4.2a. Using a projection technique, the band structures of HfS_2 and ZrS_2 in the heterostructure are extracted and presented in different colors. This technique allows us to

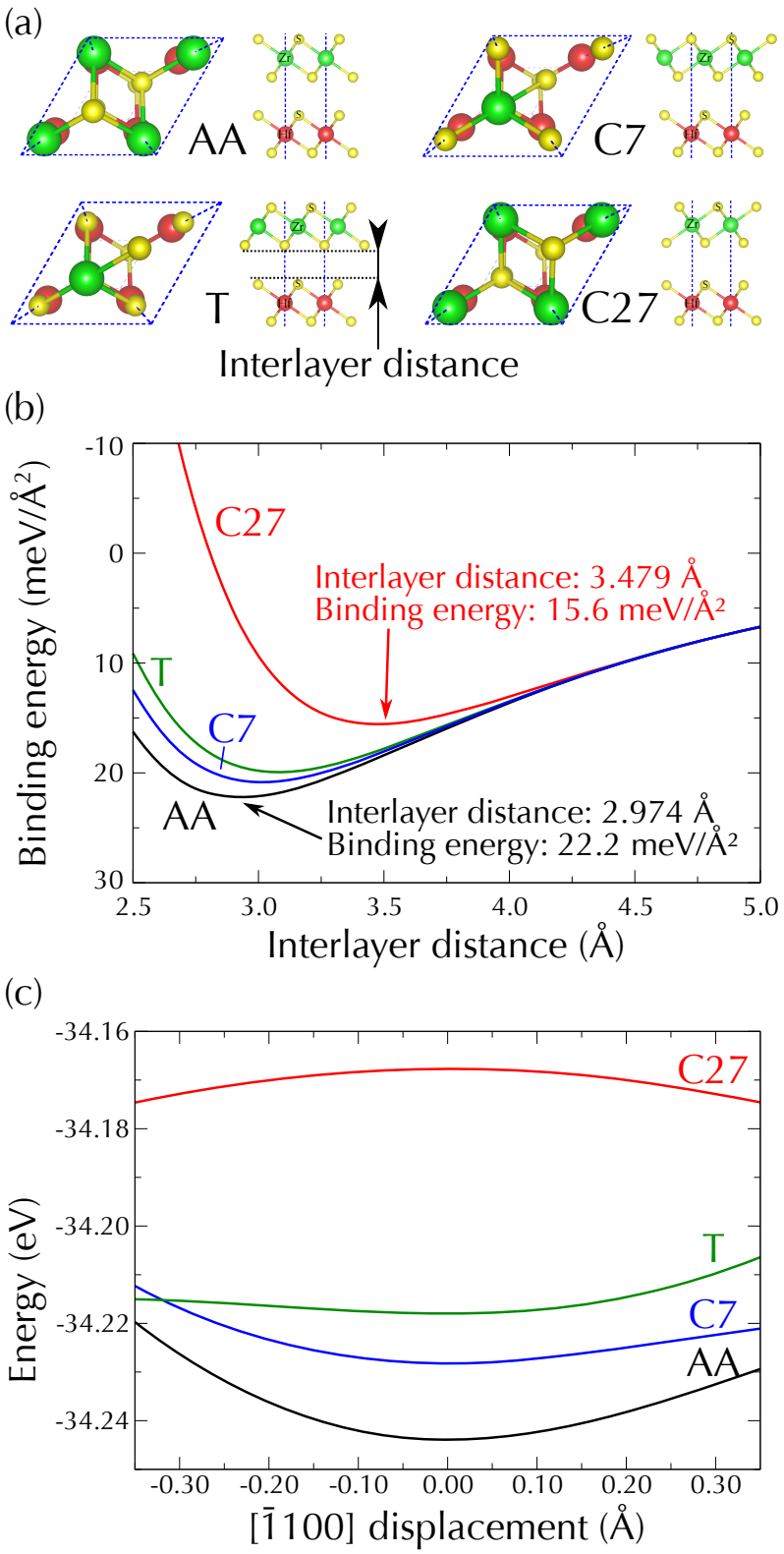

FIGURE 4.1 – (a) Four different stackings investigated for the HfS_2 and ZrS_2 heterostructure. Zirconium, hafnium and sulfur are depicted in green, red and yellow, respectively, and the dashed lines detail the supercell edges. (b) Total energy of the supercell for the different stackings, showing a stable configuration for each one of them. (c) Total energy of the supercells on their own equilibrium interlayer distance for small displacements in the $[\bar{1}100]$ direction.

derive the local energy gap E_g, the valence band maximum (VBM or negative I) at Γ, and the conduction band minimum (CBM or negative A) at M in the BZ of the two materials for each given stacking, strain and, hence, the vdW interactions. The corresponding results are summarized in Table 4.1. The stacking and bilayer influences follow from a comparison with the corresponding quantities of the freestanding 2D crystals in Table 3.1. Indeed, the values E_g, A and I are influenced by the heterocombination. We have to point out that a similar influence due to stacking in Table 4.1 has been recently observed experimentally for the interlayer twist in the graphene/MoS_2 system (JIN *et al.*, 2015). The differences in the CBM and VBM values in Table 4.1 define the true band discontinuities between material 1 and 2,

$$\begin{aligned} \Delta E_v &= \mathrm{VBM}(2) - \mathrm{VBM}(1), \\ \Delta E_c &= \mathrm{CBM}(1) - \mathrm{CBM}(2) \end{aligned} \tag{4.2}$$

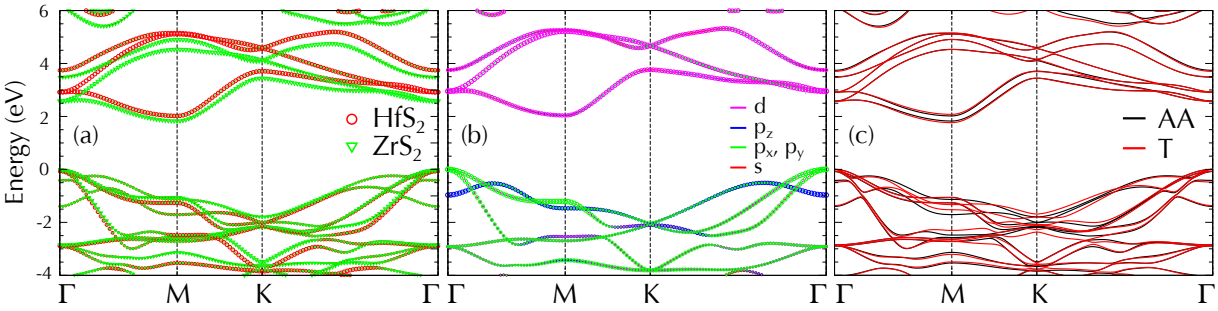

FIGURE 4.2 – (a) Band structure of HfS_2/ZrS_2 heterostructure with AA stacking projected onto each layer calculated with HSE06. Contributions from HfS_2 are shown with red circles and from ZrS_2 are displayed with green triangles. The size of the marker indicates the relative contribution from each monolayer to the total band structure. (b) Orbital character of the bands states of pristine HfS_2. (c) Influence of different HfS_2/ZrS_2 stackings on the heterobilayer band structures.

in the heterostructure. They can be compared with the natural band discontinuities

$$\begin{aligned} \Delta E_v^{\mathrm{nat}} &= I(1) - I(2), \\ \Delta E_c^{\mathrm{nat}} &= A(2) - A(1), \end{aligned} \tag{4.3}$$

applying the vacuum level alignment (BECHSTEDT, 2003; MÖNCH, 2004) and the characteristic energies from Table 3.1. The band discontinuities characterize a type I (II) heterostructure by $\Delta E_v \cdot \Delta E_c > 0$ ($\Delta E_v \cdot \Delta E_c < 0$).

The energy differences in the band gaps and positions of band extrema (see Table 4.1) and, hence, bands discontinuities are inferior to of 0.10 eV between different stackings, suggesting only a little charge transfer through the interface between the two sheet crystals HfS_2 and ZrS_2. However, this trend is not monotonous. This observation is supported

TABLE 4.1 – Characteristic electronic energies of HfS_2 and ZrS_2 in a vdW-bonded heterostructure with interface calculated with HSE06. The projection technique illustrated in Fig. 4.2a is used to extract values for the individual 2D crystals. The conduction band minimum (CBM) and valence band maximum (VBM) are taken with respect to the vacuum level. The band gap (E_g) is the energy difference between the CBM and VBM for each monolayer in the heterojunction. The energies from isolated monolayers are also shown for the ease of comparison.

	HfS_2			ZrS_2		
Stacking	CBM (eV)	VBM (eV)	E_g (eV)	CBM (eV)	VBM (eV)	E_g (eV)
Monolayer	-4.925	-6.956	2.03	-5.138	-6.989	1.85
AA	-4.951	-7.049	2.10	-5.144	-6.970	1.83
C7	-4.944	-7.040	2.10	-5.157	-6.971	1.81
T	-4.887	-7.035	2.15	-5.201	-6.965	1.76
C27	-4.785	-6.922	2.14	-5.064	-6.859	1.80

by the almost unchanging electronic properties of the two materials when comparing the values in Tables 3.1 and 4.1. Thereby, the influence of the most stable AA, C7 and T stackings and the details of the atomic geometry on the VBM positions is negligibly small. The main effect of the heterostructure are the absolute shifts of the VBM of HfS_2 (ZrS_2) of about 0.08 (0.02) eV toward lower (higher) energies with respect to the freestanding situations. The opposite behavior is found for the CBM. As a consequence, the gap of HfS_2 (ZrS_2) is opened (shrunk) compared to the isolated situation along the row AA, C7 and T. These small shifts, however, have important consequences for the predicted heterostructure behavior. In comparison to the type II expectation for the pristine monolayers with the natural band discontinuities $\Delta E_v^{\mathrm{nat}} = -33$ meV and $\Delta E_c^{\mathrm{nat}} = 213$ meV from Table 3.1, the real junctions change from type II to type I due to vdW interactions and the small valence band offset already visible from the natural band alignment. For instance, in the AA case, band discontinuities $\Delta E_v = 79$ meV and $\Delta E_c = 193$ meV occur. This fact is accompanied by an increase in the band gap of HfS_2 and decrease in the band gap of ZrS_2 in the heterostructure.

For the purpose of better understanding the influence of interlayer interactions in band alignments, we have inspected the formation of the bands from the original HfS_2 and ZrS_2 monolayers. Considering the similarities shared by these two TMDCs and perceiving that their bands are generated within the same crystal structure, we depict the nature of the bands and their orbital character only for HfS_2 in Fig. 4.2b. The formation of the bands for ZrS_2 is analogous and hence not explicitly shown. It is possible to explain the almost invariance of the band gap and band discontinuities in the heterobilayer recognizing the predominance of localized cation d orbitals in the CBM and in-plane anion $p_x + p_y$ states in the VBM, which overlap less with the states from the other layer in contrast to the p_z

orbitals. In fact, the greatest alterations are seen near the BZ boundary, in which the predominance of p_z orbitals in the valence band affects more the electronic properties of the vdW-bonded heterostructure and hence interlayer separation and stacking order. Stackings in which p_z orbitals prevail in the band formation, such as phosphorene or graphene, suffer pronounced changes in the electronic structure due to these interlayer interactions (PADILHA *et al.*, 2015). We also observe a mixture of orbitals at the conduction band minimum near the M point, made predominantly from d_{z^2} and d_{yz} orbitals from the cations. As the stacking goes from the most stable configuration to the least stable one, i.e., from AA to C27, we increase the repulsion between these orbitals from each layer, thus slightly modifying the fundamental band gap of each 2D crystal. The T stacking, however, leads to the larger shifts in the band gaps due the smaller distance between each layers cations (Hf or Zr) and the sulfur anions. These shifts are more directly shown in Table 4.1 and depicted in Fig. 4.2c.

Despite the weak vdW interactions between the two layered crystals do not significantly change the band gaps of each layer constituting the heterointerface, transitions between heterostructure types may happen through their direct contact if the natural band line-ups are characterized by only small band offsets. Interaction-induced changes in the valence or conduction band created by interlayer interactions and orbital overlaps can surmount these natural band alignments and force the transition between a type II to a type I heterostructure or vice-versa, depending on the sensitivity of each layer to orbitals overlapping and charge transfer. Modulation of these properties via external factors, however, such as piezoelectricity (HUANG *et al.*, 2015b), electric field (HUANG *et al.*, 2015a) or interface decoupling (FANG *et al.*, 2014) may also be employed to fine tune the interface properties.

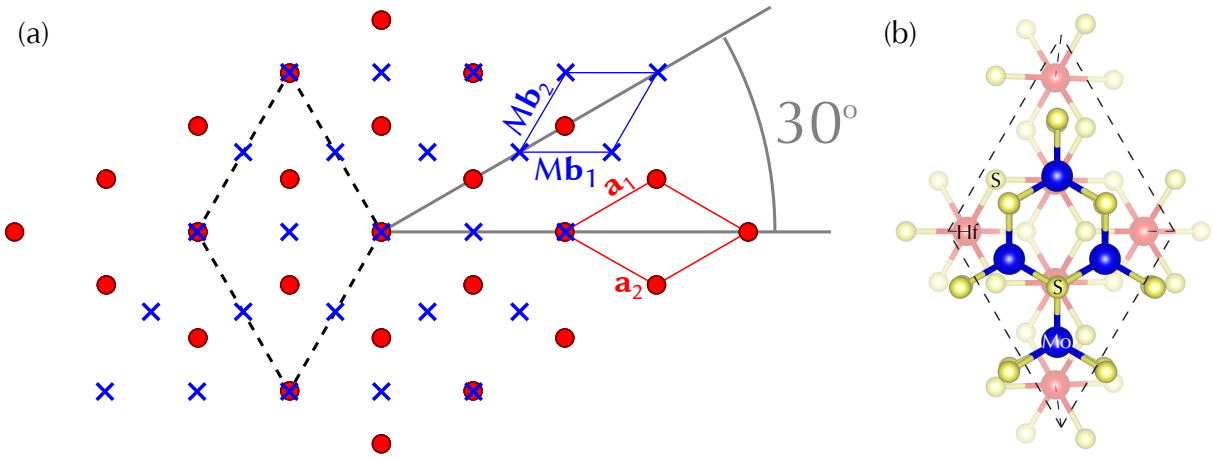

FIGURE 4.3 – (a) Matching of a MoS_2 lattice (blue crosses) and a HfS_2 lattice (red circles) under a relative rotation of 30° and (b) the supercell generated in this case. Molybdenum, hafnium and sulfur atoms are depicted in blue, red and yellow, respectively.

4.4 Effects of stacking on lattice-mismatched bilayers

The same kind of total energy optimizations, electronic band structure calculations and electronic structure investigations has also been applied to the vdW-bonded HfS_2 or ZrS_2 $(\sqrt{3}\times\sqrt{3})$ R30° on MoS_2 (2×2) heterosystem (see Table 3.3). As a supercell in real space, i.e., a non-primitive unit cell of the original crystal lattice, is used, the resulting reciprocal space vectors shrink with respect to the original ones. This leads to band structures folded onto the small Brillouin zone of the coincidence lattice, but without changes in the fundamental electronic properties of each isolated monolayer. The coincidence lattice and the atomic geometry resulting in the HfS_2/MoS_2 case are presented in Fig. 4.3. The two heterocombinations are not lattice-constant matched and, therefore, are good examples for application of the coincidence lattice method to construct supercells in the first step. In the subsequent total energy calculations of the atomic geometries, we have assumed that the entire strain appears in the MoS_2 2D crystal. Only a few electronic changes are observed, e.g. the band gap of MoS_2 changing from 2.25 eV to 2.31 eV while keeping its direct gap character at K. This increase in the MoS_2 gap is due the small compressive strain and has also been predicted in previous studies (GUZMAN; STRACHAN, 2014). The vdW coupling of the two layers lowers the total energy of the supercell and a stable configuration is found with an interlayer distance of 3.329 Å for the HfS_2/MoS_2 system and 3.299 Å for the ZrS_2/MoS_2 system, respectively, with a binding energy of 20 meV/Å^2 in both cases, as shown in Fig. 4.4a. The total energy of the layer stacking does not change by values larger than 1 meV when lateral atomic displacements are made in any lateral direction. Thus, the heterostructures are independent of any relative translation of the two atomic layers against each other, as long as the coincidence lattice remains fixed. Comparing with the larger energy variations predicted for other MoS_2-including heterosystems (BJÖRKMAN *et al.*, 2012), we conclude that the two studied heterobilayers are stable with a given coincidence lattice but rather invariant against planar translations. The two systems are examples in which the lattice mismatch creates a spatially distributed stacking arrangement, leading to an energy gain due to the interface binding regardless their relative lateral positions.

The electronic properties of the two heterostructures are displayed in Figs. 4.4b and 4.4c. We observe a direct character of the MoS_2 band gap, while the indirect band gap of the HfS_2 (ZrS_2) suffers a reduction of 0.1 eV. We find a valence band offset of $\Delta E_v = 0.67$ eV (0.68 eV) and a conduction band offset of $\Delta E_c = -0.97$ eV (-1.09 eV) for the HfS_2/MoS_2 (ZrS_2/MoS_2) system. The comparison with the natural band discontinuities $\Delta E_v^{\mathrm{nat}} = 0.65$ eV/$\Delta E_c^{\mathrm{nat}} = -0.86$ eV (MoS_2/HfS_2) and $\Delta E_v^{\mathrm{nat}} = 0.69$ eV/$\Delta E_c^{\mathrm{nat}} = -1.07$ eV (MoS_2/ZrS_2) from Table 3.1 shows that the two heterostructures preserve the natural band alignments of the individual materials given in Table 3.1, i.e., a type II heterocharacter despite the relative rotation imposed on the supercell simulated

and the vdW bonding. The small difference between the natural band discontinuities and the values obtained from the simulated interface in the HfS_2/MoS_2 heterojunction is due the small strain induced in MoS_2 needed to compose a commensurate system.

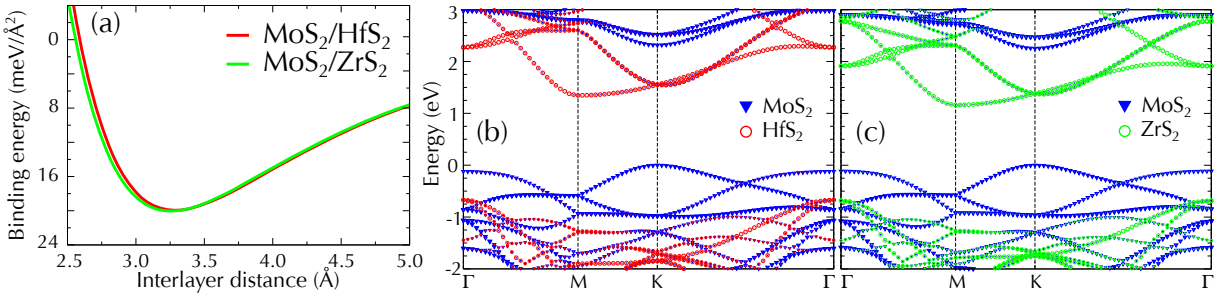

FIGURE 4.4 – (a) Binding energy of the MoS_2 on top of HfS_2 and ZrS_2 per unit area versus the interlayer distance. For each equilibrium positions, band structures projected onto each monolayer are given for the (b) MoS_2 and HfS_2 and (c) MoS_2 and ZrS_2 heterostructure calculated with HSE06 for the lowest-energy arrangements. Relative sizes of markers indicate percentual composition of each band from each material.

The projected band structures for both simulated heterointerfaces in Figs. 4.4b and 4.4c do not only show the character of the band gaps in the k-space for the "isolated" 2D crystals, but they also clearly indicate the indirect character of the band gaps of the heterostructure in real space. While the CBM appears at M in the HfS_2 or ZrS_2 layer, the VBM at K is defined by the MoS_2 system. The projection technique illustrates the low influence of vdW interactions on the electronic structures of these heterostructures by the very localized band states, which do not indicate reasonable state mixing or electron transfers. The latter phenomena occurs only at symmetry points where the band states are constituted mainly by p_z orbitals, as in the case of the heterostructure band originated from the valence band states of HfS_2 or ZrS_2. This band is composed with significant contributions from both layers and undergo a transition between the M and K points. In the band structures from Figs. 4.4b and 4.4c, this is evidenced by the shrinkage of the circles, i.e. the percentage of orbitals from the HfS_2 or ZrS_2 layer, and the increase of the size of blue triangles. Conduction bands, whose character is based predominantly on d orbitals, do not withstand appreciable changes.

4.5 Effects of rotation on structural properties of bilayers

Exactly as performed for the TMDC heterobilayers, we start from the DFT-optimized 2D crystals and their Bravais lattices. According to predictions from Chapter 3, if a $hBN/MoSe_2$ heterobilayer would be constructed without taking rotations into account, a (4×4) hBN and (3×3) $MoSe_2$ supercell could be built if both layers were subjected to a

biaxial strain of 0.73%, compressive for hBN and tensile for $MoSe_2$. Furthermore, a supercell with 59 atoms would have to be simulated. Creating a supercell of a $(\sqrt{7} \times \sqrt{7})$ R19.1° hBN on (2×2) $MoSe_2$, however, reduces the strain to make the system commensurate to an absolute value of 0.33% on both layers, still compressive for hBN and tensile for $MoSe_2$. This supercell contains 26 atoms inside itself and is depicted in Fig. 4.5a. To further expand investigations concerning rotations, a $(\sqrt{12} \times \sqrt{12})$ R30.0° hBN on $(\sqrt{7} \times \sqrt{7})$ R19.1° $MoSe_2$ supercell can be created to minimize the strain necessary to make the system almost commensurate, as a biaxial strain as small as 0.18% on both layers would be enough to create the supercell. This last system is still smaller than the aligned heterobilayer supercell, with 45 atoms to be taken in consideration, and is represented by Fig. 4.5b.

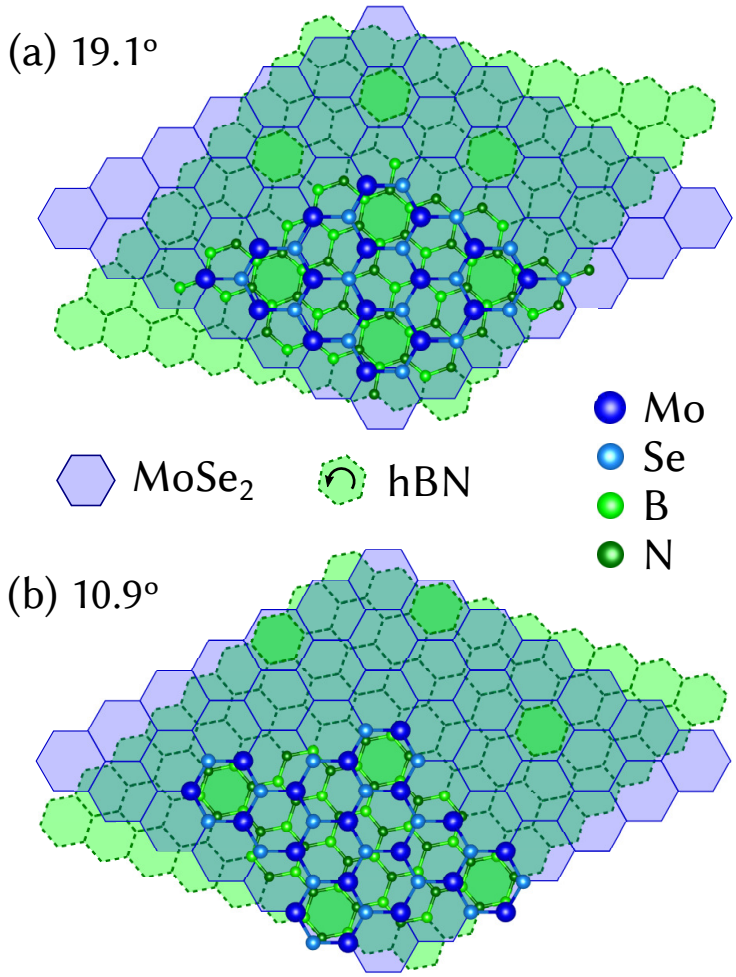

FIGURE 4.5 – Coincidence lattices and atomic representation for the $MoSe_2$/hBN heterobilayer for interlayer twist angles of (a) 19.1° and (b) 10.9°. Blue (green) hexagons with solid (dashed) lines depict $MoSe_2$ (hBN) Bravais lattices, respectively, while dark blue, light blue, light green and dark green circles depict molybdenum, selenium, boron and nitrogen atoms, respectively. Coincidence lattices are highlighted with green hexagons as a guide to the eye.

We simulate the last two systems, designated by their relative interlayer twist angle of 19.1° and 10.9°, due to their lower strain and size compared to the aligned system.

In order to preserve the electronic properties of the strain-sensitive $MoSe_2$ (GUZMAN; STRACHAN, 2014), such as its direct band gap, we apply all strain on hBN. This leads to biaxial strains on this layer of -0.67% (0.37%) for the 19.1° (10.9°) rotated system. The applied strain has small influences on electronic properties of hBN. This commensurability strain shifts the CBM upwards (downwards) by 0.05 eV (0.04 eV) and the VBM downwards (upwards) by 0.02 eV (0.01 eV) for the -0.67% (0.37%) strain case. The tensile strain of 0.37% on hBN also leads to a indirect to direct band gap transition.

For each of the two interlayer twist angles investigated, a minimum of energy is found, as shown in Fig. 4.6. Then, letting the heterobilayers with an interlayer distance that minimizes the energy of the systems, i.e. their most stable configuration, atomic positions are relaxed. Both systems are almost identical when considering their binding energy curves, with a binding energy of 21.2 meV/Å^2 (21.1 meV/Å^2) for a relative rotation angle of 19.1° (10.9°). These values are reasonable for molybdenum diselenides (BJÖRKMAN *et al.*, 2012). Interlayer twists do not induce significant changes in the equilibrium distance of the bilayer system because of the planar structure of hBN, for which no preferential stacking is found within the heterobilayer. Nevertheless, vdW interactions assure the stability with the same binding energy regardless of the interlayer twist angle.

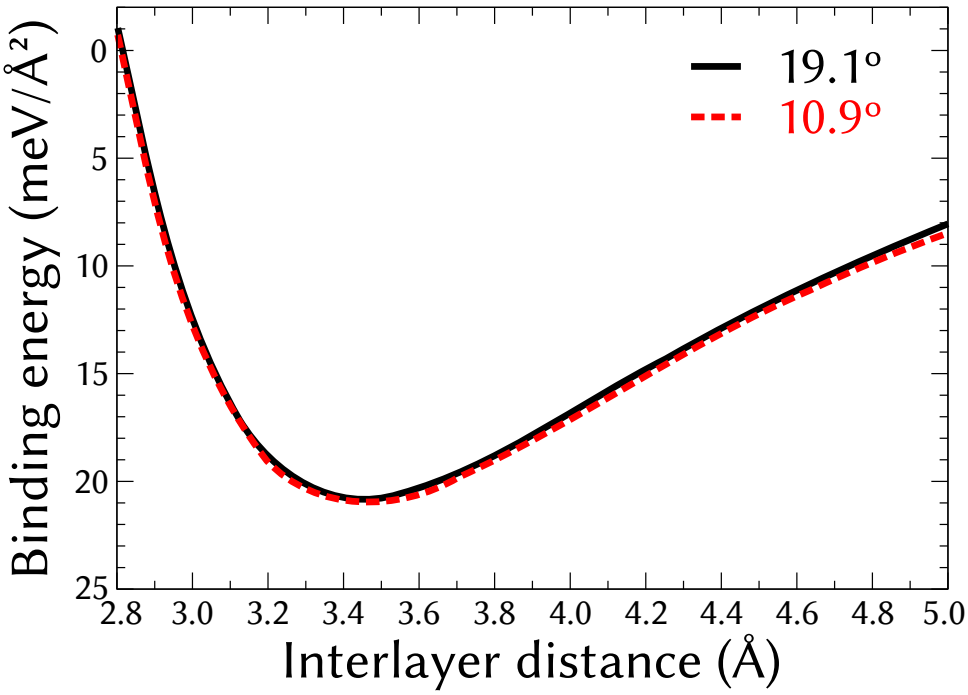

FIGURE 4.6 – Binding energy curves for the $MoSe_2$/hBN heterobilayer system for interlayer twist angles of 19.1° (solid black line) and 10.9° (dashed red line). The equilibrium distance for the 19.1° (10.9°) rotated system is 3.44 Å (3.48 Å) and the binding energy for the most stable configuration is 20.9 meV/Å^2 (21.1 meV/Å^2) if no relaxation in atomic positions is performed.

4.6 Effects of rotation on electronic properties of bilayers

For both heterobilayers on their respective equilibrium positions, band structures are calculated within the DFT using the functional GGA-PBE and then projected onto atomic sites, being represented with colors to allow better interpretations of band formations, as depicted in Fig. 4.7. Projected bands from each monolayer differ from the ones of their 1×1 cells due to band foldings that occur onto the first Brillouin zone (1BZ) when using a supercell to calculate band structures. In order to understand band foldings in arbitrary monolayer supercells, let $\mathbf{k}$ be a point in the 1BZ, written as a linear combination of a reciprocal lattice vector basis $(\mathbf{b}_1, \mathbf{b}_2)$ as

$$\mathbf{k} = k_1\mathbf{b}_1 + k_2\mathbf{b}_2. \tag{4.4}$$

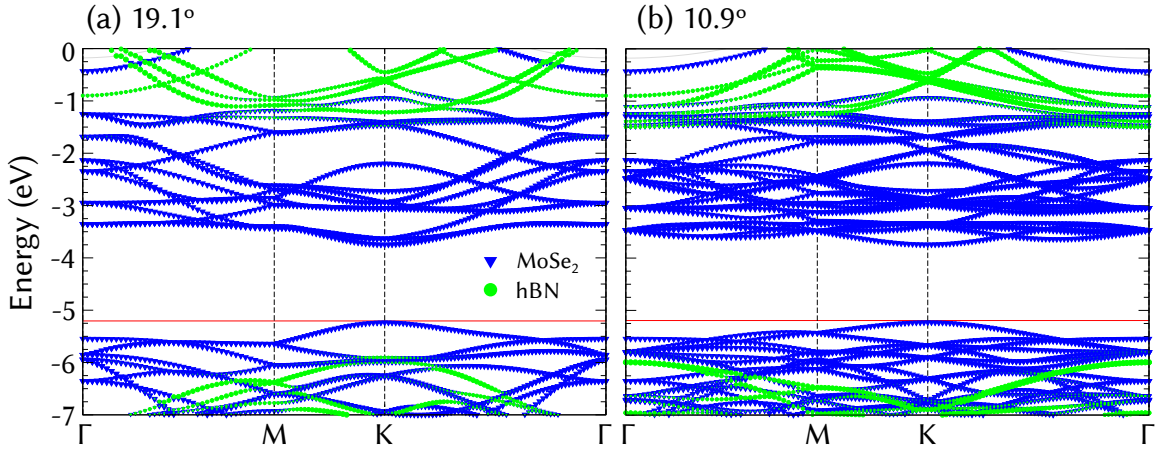

FIGURE 4.7 – Projected band structures for the $MoSe_2$/hBN heterobilayer system with an interlayer twist angle of (a) 19.1° and (b) 10.9° calculated with GGA-PBE. Blue triangles and green circles depict contributions from $MoSe_2$ and hBN, respectively, to the specific eigenvalue for each k-point. Greater relative contributions are represented by bigger markers. The vacuum level of the $MoSe_2$ side is set as the reference and the red line identifies the top of the valence band.

We start from the three-dimensional vector basis $(\mathbf{a}_1, \mathbf{a}_2, \mathbf{a}_3)$ and use the definition of reciprocal lattice vectors from Ashcroft and Mermin (ASHCROFT; MERMIN, 1976),

$$\begin{cases} \mathbf{b}_1 = 2\pi \frac{\mathbf{a}_2 \times \mathbf{a}_3}{\mathbf{a}_1 \cdot (\mathbf{a}_2 \times \mathbf{a}_3)} \\ \mathbf{b}_2 = 2\pi \frac{\mathbf{a}_3 \times \mathbf{a}_1}{\mathbf{a}_1 \cdot (\mathbf{a}_2 \times \mathbf{a}_3)} \end{cases} . \tag{4.5}$$

The 2D Bravais lattice requires only two vectors to be described. Therefore, $\mathbf{a}_3$ may be adopted as $[0\,0\,1]^{\mathrm{T}}$ and the definitions from equation 4.5 reduced to two dimensions by

simplifying the cross product. This leads to

$$\begin{cases} \mathbf{b}_1 = \frac{2\pi}{\det A} \begin{bmatrix} a_{2y} \\ -a_{2x} \end{bmatrix} \\ \mathbf{b}_2 = \frac{2\pi}{\det A} \begin{bmatrix} -a_{1y} \\ a_{1x} \end{bmatrix} \end{cases}, \tag{4.6}$$

in which

$$A = \begin{bmatrix} \mathbf{a}_1 & \mathbf{a}_2 \end{bmatrix} = \begin{bmatrix} a_{1x} & a_{2x} \\ a_{1y} & a_{2y} \end{bmatrix}. \tag{4.7}$$

Finally, the reciprocal lattice vectors can be written as

$$B = \begin{bmatrix} \mathbf{b}_1 & \mathbf{b}_2 \end{bmatrix} = \frac{2\pi}{\det A} \begin{bmatrix} a_{2y} & -a_{1y} \\ -a_{2x} & a_{1x} \end{bmatrix} = 2\pi A^{-\mathrm{T}}. \tag{4.8}$$

Suppose the Bravais lattice symmetry is preserved with a linear transformation, i.e. an operation M is applied to both direct lattice vectors $\mathbf{a}_1$, $\mathbf{a}_2$. The new lattice vectors are, therefore, described by

$$\tilde{A} = MA = \begin{bmatrix} \tilde{\mathbf{a}}_1 & \tilde{\mathbf{a}}_2 \end{bmatrix} = \begin{bmatrix} M\mathbf{a}_1 & M\mathbf{a}_2 \end{bmatrix}, \tag{4.9}$$

and the reciprocal lattice is transformed into

$$\tilde{B} = 2\pi(MA)^{-\mathrm{T}} = 2\pi M^{-\mathrm{T}} A^{-\mathrm{T}}. \tag{4.10}$$

Therefore, the coordinates of the point $\mathbf{k}$ after the change of basis, denoted here by $\tilde{\mathbf{k}}$,

$$\tilde{\mathbf{k}} = \tilde{k}_1 \tilde{\mathbf{b}}_1 + \tilde{k}_2 \tilde{\mathbf{b}}_2 = \tilde{B} \begin{bmatrix} \tilde{k}_1 \\ \tilde{k}_2 \end{bmatrix}, \tag{4.11}$$

are calculated by

$$\begin{bmatrix} \tilde{k}_1 \\ \tilde{k}_2 \end{bmatrix} = B^{-1} M^{\mathrm{T}} B \begin{bmatrix} k_1 \\ k_2 \end{bmatrix}. \tag{4.12}$$

When the methodology from Eqs. 4.4 to 4.12 is employed to calculate the symmetry points for the supercells, it becomes clear that both the K and M points of the 1×1 hexagonal BZ are folded onto Γ for a $(\sqrt{12} \times \sqrt{12})$R30° hexagonal supercell. An immediate

consequence is that the direct band gap of monolayer $(\sqrt{12}\times\sqrt{12})$R30° hBN on K is folded onto Γ. Other relevant symmetry foldings for supercells used in this work are described in Table 4.2. Therefore, the use of monolayer supercells necessary for the construction of heterostructure cells may change the presentation of band structures when comparing with the original ones due to folding. Analysis of electronic properties must be done having in mind that original monolayer supercells lead to different foldings when band structures are plotted, and that this procedure does not interfere with electronic properties of each material. On the other hand, since coincidences between two Bravais lattices define unit cells for heterostructures, band structures for the interface such as the ones depicted in Fig. 4.7 should not be interpreted as folded. Rather, no redundancy is presented within these band structures and no further simplifications are allowed.

TABLE 4.2 – Folding symmetry for 1BZ points in hexagonal supercells. "Original point" corresponds to the symmetry point as seen in a 1×1 cell. When the linear operation described in the "Supercell" column is applied to the unit system, the original point is folded onto the 1BZ according to the relationship shown in the "Folded onto point" column.

Supercell	Original point	Folded onto point
1×1	K	K
	M	M
2×2	K	K
	M	Γ
$(\sqrt{7}\times\sqrt{7})$ R19.1°	K	K
	M	M
$(\sqrt{12}\times\sqrt{12})$ R30°	K	Γ
	M	Γ

For both simulated systems, the direct band gap of $MoSe_2$ is retained and does not deviate from the value of 1.50 eV obtained by simulation of the isolated monolayer. This illustrates an important advantage for the use of hBN as a substrate for optoelectronic applications using this TMDC. On the other hand, electronic properties of hBN differ when rotation is included. An analysis of the heterostructure bands by means of orbital composition indicates an out-of-plane overlapping of p_z orbitals from the hBN layer with d_{xz} and d_{yz} orbitals from $MoSe_2$ layer. Interlayer interactions, therefore, may decrease the band gap projected onto hBN due to the formation of hybrid bands with contributions of both monolayers. However, an interlayer twist of 19.1° keeps sharper distinctions between hBN and $MoSe_2$ conduction bands in the k-space, as can be seen in the projected bands of Fig. 4.7a. This can be compared to the mixed-contributions conduction bands at Γ in the k-space when an angle of 10.9° is imposed to the heterobilayer to assume that relative rotations can influence electronic properties of the monolayer hBN substrate. The opposite effect seems to happen to the valence band. The 19.1°-rotated bilayer presents

more interlayer overlap, which is seen in Fig. 4.7a next to the K point for energies close to -5.8 eV. Meanwhile, the hBN valence band for the 10.9° system distinguishes itself from the $MoSe_2$ bands.

The analysis of the density of states (DOS) for both systems agrees with this inferences. Figure 4.8 shows the DOS calculated for both bilayer heterostructures, from which three important features can be noted. Firstly, the $MoSe_2$ DOS is not influenced close to the valence and conduction bands for both heterobilayers, thus underpinning the preservation of electronic properties of this TMDC upon contact with hBN. Secondly, the conduction band of hBN can be distinguished from the overlapped states with $MoSe_2$ bands because of the falling edge followed by a rising edge at -1.25 eV. Evidently, the DOS for hBN above the CBM should be substantially greater than zero. The same cannot be seen in the 10.9° rotated system, which has a non-zero density of states for energies above -1.50 eV. Furthermore, the magnitude of the DOS for energies close to the CBM of hBN is close to that from hBN itself, indicating the presence of significant hBN states above -1.50 eV. Finally, the density of states for the valence band of both systems show that a step-like DOS for the VBM of hBN in the 10.9° system is coherent with the low-interference between bands. Alternatively, the valence band analysis for the 19.1° heterobilayer shows that the spiky DOS should be consequence of interlayer effects for bands close to this energy.

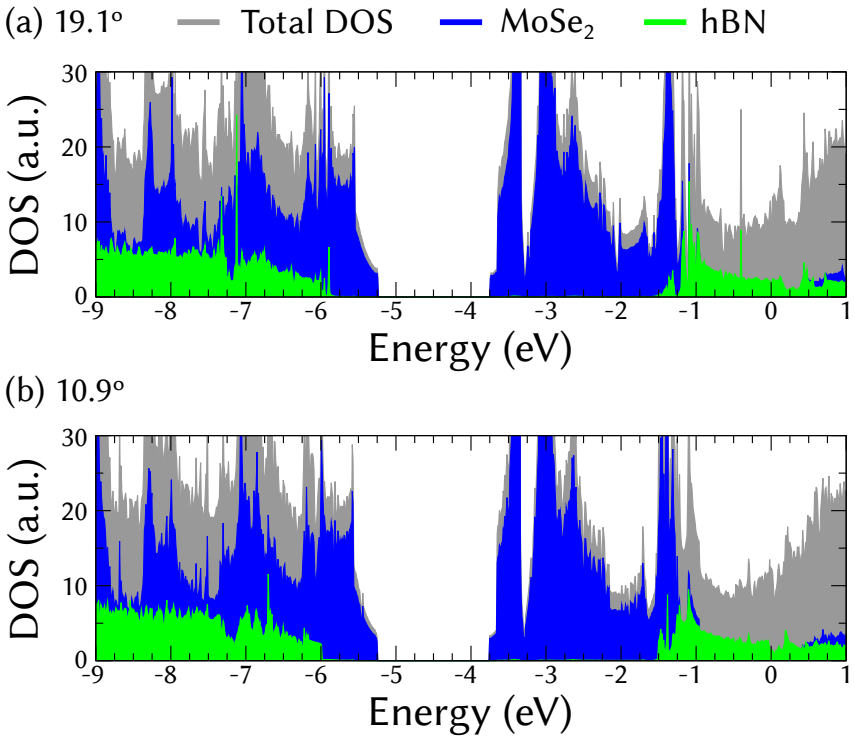

FIGURE 4.8 – Density of states for the $MoSe_2$/hBN heterostructure with an interlayer twist of (a) 19.1° and (b) 10.9°. Gray, blue and green lines depict total states, states from the $MoSe_2$ and from the hBN layers. The vacuum level of the $MoSe_2$ side is set as the reference.

With the electrostatic potential of the vacuum set as the reference for all calculations, it is possible to make a comparison between the band discontinuities given by the separated layers (the natural band alignment) and the band offset of the calculated heterostructure. However, charge transfer effects must be taken into consideration by means of the dipole step in the vacuum level. In both simulated heterobilayers, the vacuum on the $MoSe_2$ side is taken as reference. With respect to this zero, CBM and VBM of $MoSe_2$ do not shift when compared to its natural alignments. However, hBN suffers a shift down, as the VBM shifts downwards by 0.25 eV (0.44 eV) with respect to their VBM for their -0.66% (0.37%) strained and isolated counterparts simulated within the 19.1° (10.9°) systems. This shift could also be responsible for enhancing interlayer interactions in both heterobilayers, specifically for the conduction band, and partly due to the charge transfer between the two layers. We report a ratio between the conduction and valence band of approximately 80:20 (75:25) for the 19.1° (10.9°) system. Figs. 4.9a,b summarize this findings. These effects on band discontinuities can be explained by means of charge transfer mechanisms. By using the differential charge density given by

$$\begin{aligned} \Delta n(z) = \iint n_{\text{het}}(x,y,z)\,dx\,dy - \\ \iint n_{\text{MoSe}_2}(x,y,z)\,dx\,dy - \iint n_{\text{hBN}}(x,y,z)\,dx\,dy, \end{aligned} \tag{4.13}$$

and the total charge transferred as a function of the z position,

$$Q(z) = \int_0^z \Delta n(\xi)\,d\xi, \tag{4.14}$$

a charge transfer analysis can be plotted as in Fig. 4.9c. For both analogous systems, electrons are transferred from the hBN layer to the $MoSe_2$ layer, creating a dipole in the interface. Evaluating $Q(z)$ in the interface between hBN and $MoSe_2$, it can be seen that the charge is negative. This means hBN is depleted from electrons, while $MoSe_2$ receives electrons. Thus, the positive electric charge in hBN shifts down the band edges, in agreement with the dipole step in the interface.

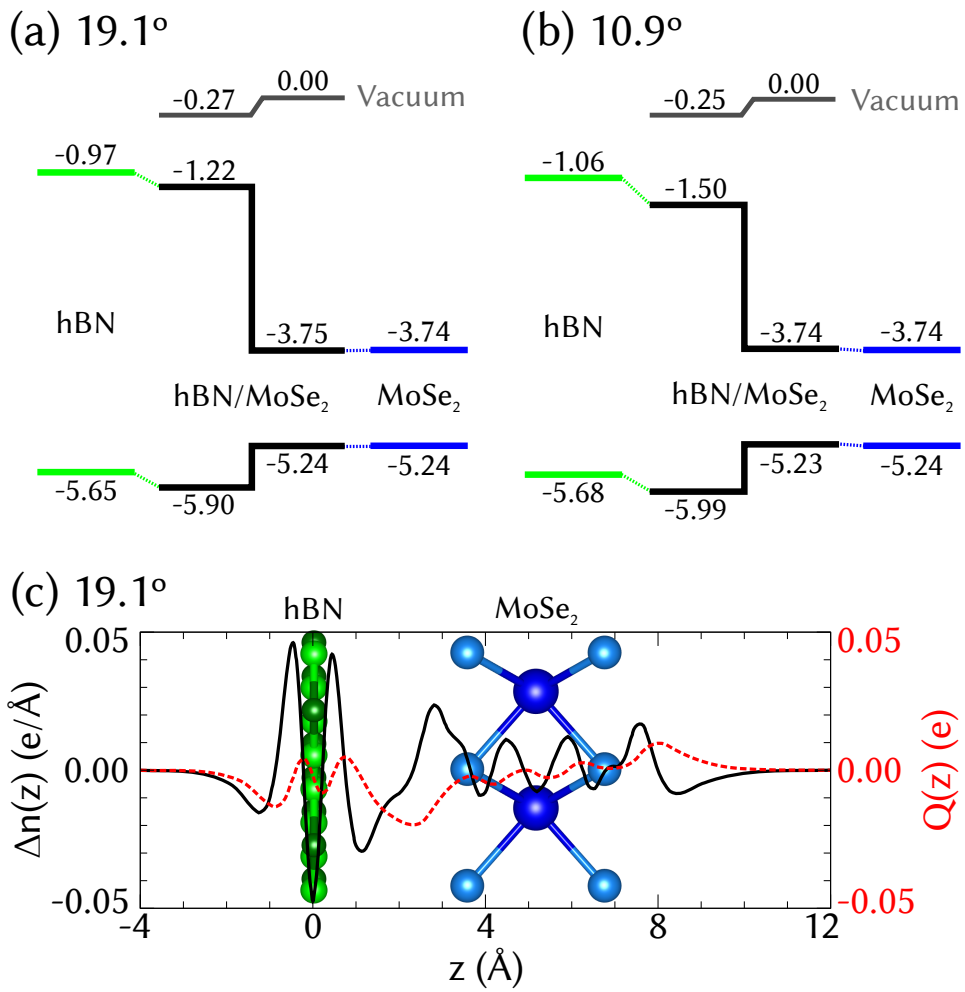

FIGURE 4.9 – Band alignments (in eV) calculated with respect to the vacuum level for the hBN/$MoSe_2$ bilayer when an interlayer twist angle of (a) 19.1° and (b) 10.9° is taken into account. The natural band discontinuities for hBN are from the -0.67% (0.37%) strained monolayers which form the 19.1° (10.9°) heterobilayer. (c) Differential charge density (Δn, black solid lines) and transferred charge (Q, red dashed lines) for the 19.1° bilayer system. Positions of the hBN and $MoSe_2$ layers are represented with the individual cells. The 10.9° system is analogous and is suppressed.

5 Influences of external perturbations on band alignments

5.1 Motivation

Most important characteristics for heterojunctions are the band offsets at the interface, especially for band-engineered devices. Comparisons between the natural band discontinuities of 2D crystals, based only on the original electron affinity rule (ANDERSON, 1962; ANDERSON, 1960), and the band lineups in heterosystems demonstrate that the weak interlayer bonding between the two layers and the formation of quantum dipoles (TERSOFF, 1984; SCHLAF *et al.*, 1997) may influence the electronic properties of the constituents of the interface (KANG *et al.*, 2013; WEI *et al.*, 2016; ZHOU; ZHAO, 2016). The modeling of a realistic heterointerface subject to external perturbation, which takes into account the influence of long-range stacking orders and vdW-induced structure variations, could lead to substantial modifications in electronic structures of the materials in the heterojunction. This turns out to be possible if the coincidence lattice method is employed to minimize computational costs for vdW heterostructures of interest.

Several heterojunctions have already been experimentally suggested or even prepared by 2D crystals weakly-bonded with phosphorene (Ph) including graphene/Ph bilayers (PADILHA *et al.*, 2015), Ph/MoS_2 diodes (DENG *et al.*, 2014), and phosphorene encapsulated with hexagonal boron-nitride (CHEN *et al.*, 2015). The peculiar sensitivity from Ph may hold interesting physics regarding band gaps and band offsets, as well as some clues to tune band alignments within vdW interfaces. In this chapter, we analyze structural and electronic properties of realistic Ph/$MoSe_2$ and Ph/WSe_2 combinations. Structural properties and the stability of the bilayers is analyzed in Sec. 5.2. The most stable configurations are then investigated according to their electronic properties in Sec. 5.3. Finally, the behavior of the band alignments and gaps of the systems under external influences such as pressure and electric field is determined in Sec. 5.4.

5.2 Structural properties of the bilayers

The simulated structures of the bilayer Ph/$MoSe_2$ are depicted in Fig. 5.1. The geometry of Ph/WSe_2 is similar and, therefore, not displayed. We start from the lattice parameters, optimized using vdW corrections via the optB86b functional (KLIMEŠ *et al.*, 2011), $a_{\mathrm{arm}} = 4.504$ Å in the armchair direction and $a_{\mathrm{zig}} = 3.305$ Å in zigzag direction for the phosphorene, and $a = 3.301$ Å for the hexagonal $MoSe_2$ and $a = 3.296$ Å for WSe_2. The vdW heterostructure supercell is constructed from non-primitive 5×1 (armchair $\times$ zigzag) unit cells of phosphorene and 4×1 rectangular unit cells of $MoSe_2$ (WSe_2), resulting in an armchair lattice parameter of 22.519 Å for both supercells. Rotations of two cells against each other are less favorable, as shown by the coincidence lattice method. To further investigate structural parameters from these heterobilayer systems, we first apply the necessary strain to make the phosphorene system commensurate on the $MoSe_2$ (WSe_2) layer. This means that small non-biaxial strains of -1.54% (-1.39%) in the armchair direction and 0.13% (0.28%) in the zigzag direction are applied to the materials, leaving the phosphorene intact. This strain slightly changes the $MoSe_2$ (WSe_2) electronic properties by increasing the band gap from 1.95 eV (2.11 eV) to 2.04 eV (2.17 eV) and by allowing a transition from a direct to an indirect band gap, as expected for a small compressive strain (GUZMAN; STRACHAN, 2014). However, the difference between direct and indirect band gaps of the TMDC layers is smaller than 0.01 eV (0.02 eV). Hence, changes observed in electronic properties of the strained materials still allow us to investigate the electronic properties of the heterobilayers without incurring into large deviations from the freestanding case, even when only one of the heterostructure constituents is strained to form the commensurate system.

Structural parameters are computed starting with a given interlayer distance in both bilayer systems by means of total energy calculations. First, the atoms are kept fixed in their positions within the layer and the distance between the layers is varied. This leads to a favorable interlayer distance of 3.415 Å (3.506 Å) for the Ph/$MoSe_2$ (Ph/WSe_2) system, in agreement with typical lengths between vdW bonded atoms and layers (KOKOTT *et al.*, 2014; KOKOTT *et al.*, 2013). Then, the atoms and the volume of the supercell are allowed to relax until the Hellmann-Feynman forces are smaller than 1 meV/Å . This leads to a more stable equilibrium configuration, which moves the phosphorene toward the $MoSe_2$ (WSe_2) layer, creating a spatial distribution for the interlayer distance in the armchair direction, resulting in a bending, as shown in Fig. 5.1c. These out-of-plane displacements are responsible for a stabilizing effect provided by the weak vdW interaction in the heterojunction and have been recently theoretically explained (KUMAR *et al.*, 2015). Atomic displacements occur in the armchair direction, which has been predicted as being the preferential direction for dislocations due its out-of-plane flexibility (WANG *et al.*, 2016b). The resulting armchair warping is only observed due to the long-range

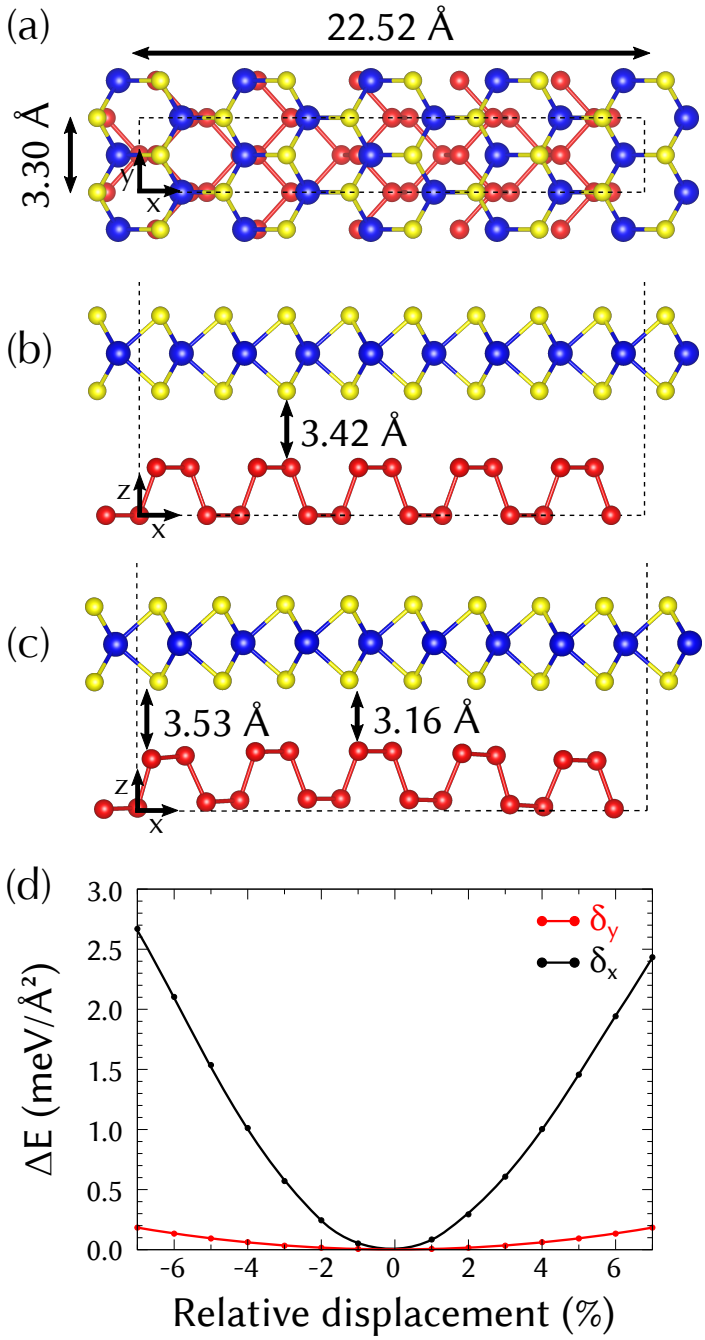

FIGURE 5.1 – Supercell used for simulating the Ph/$MoSe_2$ heterointerface. A (a) top and (b) side view before structural relaxation depict the flat interface between the two materials. (c) After minimization of atomic forces, the phosphorene moves toward the $MoSe_2$ layer. Phosphorus, selenium and molybdenum atoms are represented with gray, yellow and blue atoms, respectively, and the supercell boundary is displayed by red dashed lines. (d) Decrease of energy (ΔE) of the bilayer system when small relative displacements are made in the armchair (δ_x) and zigzag (δ_y) directions.

periodicity of the supercell in this direction, which is 4 times longer than the TMDC unit cell. Doubling the supercell length in the armchair direction does not change the warping. Weak interlayer interactions, therefore, compensate for the strain induced on the structure.

By comparing Figs. 5.1a and 5.1c, it can be seen that the region in which the interlayer distance between phosphorene and the TMDC layer is equivalent to an AB stacking order, while this distance is maximum to the region with an equivalent AA stacking. These local interlayer distances are compatible with AA and AB-stacked phosphorene layers (ÇAKIR *et al.*, 2015).

The stability of the heterobilayer systems is further enhanced by expanding the lateral unit cell, verified by the lowering of their total energy. Joint cells created by relaxing both structures have an armchair lattice parameter of 22.734 Å (22.740 Å) and a zigzag lattice parameter of 3.299 Å (3.297 Å) for the Ph/$MoSe_2$ (Ph/WSe_2) heterojunction. The Moiré pattern length calculated for these systems is 21.2 Å, in agreement with the supercell length for the commensurate system. This corresponds to phosphorene strained by about 1.0% in the armchair direction and -0.2% in the zigzag direction in both cases. The armchair strain for $MoSe_2$ (WSe_2) is reduced to -0.6% (-0.4%) and the zigzag strain is negligible in the heterojunction situation. In addition, the phosphorene is bended in the armchair direction by about 10%. The increased stability by straining phosphorene can be easily understood when one compares the calculated stress tensor from phosphorene with that of $MoSe_2$ or WSe_2. The natural flexibility of monolayer phosphorene in the armchair direction (in-plane stiffness of 26 N/m) (ELAHI *et al.*, 2015; WEI; PENG, 2014) with respect to in-plane strain is superior to that from the studied TMDCs (101 N/m for $MoSe_2$ and 112 N/m for WSe_2) (GUZMAN; STRACHAN, 2014). It lowers the energy of the combined system and reduces atomic forces.

By varying the interlayer distance, it is possible to infer, from the total energy calculations, the binding energy of the two systems represented as a gain of total energy per unit area, more precisely the difference between the energy of the heterobilayer and the energy of the isolated monolayers. For the flat phosphorene over $MoSe_2$ (WSe_2), the binding energy is 23.4 meV/Å^2 (23.8 meV/Å^2), which is a reasonable value for bilayer systems involving TMDCs (BJÖRKMAN *et al.*, 2012). The structural relaxation, which includes small volume changes, and the bending of the phosphorene, increases the binding energy, as this favors vdW interactions on the interface. In this case, the binding energy slightly increases to 24.9 meV/Å^2 (25.2 meV/Å^2). For the matter of comparison, we calculated the binding energy for the AB-stacked bilayer phosphorene as being 31.9 meV/Å^2. This demonstrates the stability of the vdW-bonded bilayer system, as with stacking displayed in Fig. 5.1a and its enhanced binding via out-of-plane displacements. From the lowest energy configuration, we further moved laterally one layer with respect to the other considering small relative displacements in the armchair (δ_x) and zigzag (δ_y) to make sure we really found the minimum energy configuration. This local stability is shown in Fig. 5.1d.

5.3 Electronic properties of the bilayers

Electronic properties of the isolated and bilayer systems were investigated using the exchange-correlation hybrid functional HSE06 (PAIER *et al.*, 2006b; PAIER *et al.*, 2006a; HEYD *et al.*, 2003; HEYD *et al.*, 2006). Its spatial nonlocality simulates an important property of the quasiparticle self-energy. It increases the gaps and interband distances in comparison to local or semi-local DFT results. Band structures of the bilayer systems are shown in Figs. 5.2a,b. Small differences between band structures of the flat freestanding and warped phosphorene over $MoSe_2$ (WSe_2) are due to strain effects on phosphorene created by volume relaxation. The local direct band gap of phosphorene increases from 1.54 eV in the strained and isolated monolayer to 1.72 eV (1.72 eV) when put in contact with $MoSe_2$ (WSe_2) due to vdW interactions and orbital overlapping in the interface. The increase in the band gap at Γ can be explained by the high sensitivity of the phosphorene conduction band minimum (CBM), created primarily by p_z orbitals, upon contact with other atomic layers. In our case, the overlap of $MoSe_2$ (WSe_2) d_{z^2} and p_z orbitals with those from the phosphorene layer defines about 13% (12%) of the orbital character of the joint conduction band. On the other hand, the top of the valence band overlaps little with the TMDC layer, with 4% (3%) of contribution from $MoSe_2$ (WSe_2), shifting down the VBM level and further opening the gap. This shift occurs only in regions in the k-space where the conduction band of phosphorene is generated by p_z orbitals, and this relative overlap agrees quantitatively with the band gap increase experienced by the phosphorene layer and is observed for other heterostructures containing phosphorene (HU; HONG, 2015; PADILHA *et al.*, 2015; YOU *et al.*, 2016; HUANG *et al.*, 2015b).

The second minimum in the phosphorene conduction band is originally only 0.26 eV above the global conduction band minimum. However, the uniaxial strain in the armchair direction reduces this difference, as also predicted theoretically from other work (PENG *et al.*, 2014). Since it is produced by p_x and p_y orbitals, it does not suffer an energy increase when put in contact with the TMDC layer. However, this second minimum experiences a strong orbital overlap with the $MoSe_2$ layer due to charge transfer and band superposition, as shown by the relative contributions from different layers to the conduction band in Fig. 5.2a. At about 0.70 Γ-Y, the CBM has a composition of 36% Ph and 64% $MoSe_2$, thus showing that the probability density to find an electron with an energy equal to the heterobilayer CBM is greater within $MoSe_2$. This balance of overlapping is only observed when quasiparticle effects are taken into account, since local or semi-local DFT calculations show that the second minimum in the conduction band is made by 64% phosphorene and 36% $MoSe_2$.

This discussion raises a quantum-mechanical criterion to define a band edge of vdW interfaces within hybrid systems. We define band edges as local energy minima (maxima)

near the gap in the k-space, which belong to the crystal where the probability density to find the electron (hole) with this specific energy is maximum. If such a definition, including the orbital character of the band edges, is possible, one can still introduce "real" band discontinuities in the electronic band structure of heterosystems, even if they are not well energetically separated. Since band discontinuities can also be represented by states localized at the two sides of the interface. This interpretation, derived from the electron (hole) wavefunction, allows the analysis of hybrid structures by localizing the electron (hole), instead of simply relying on the natural band discontinuities. It is also coherent with cases in which little orbital overlap is seen and helps to define a standard to vdW heterostructures with overlapping electronic properties.

The energy separations of the band edges at both sides of the heterointerface can be interpreted as "natural" band discontinuities or offsets. By setting the vacuum level as reference for the electrostatic potential, natural band discontinuities are calculated and compared with the real ones for both studied systems. These results are summarized in Figs. 5.2c,d. Band offsets for both heterobilayers, calculated with the criterion discussed above, deviate from their natural band discontinuities up to 0.2 eV. Hybridization leads to a considerable change in band lineups (black lines in Fig. 5.2c,d) for Ph/$MoSe_2$, in which the heterostructure experiences a type I to type II transition. Ph/WSe_2 systems preserve the type I of the heterostructure expected from the natural band discontinuities, since band superpositions do not affect directly the phosphorene CBM. Shifts in band levels are further enhanced by charge transfer between the two layers. By comparing the vacuum level from both sides of the interface, a potential barrier is observed due to the formation of a dipole on the interface. In both systems, the TMDC layer is depleted from electrons, which shifts downwards its bands with respect to the vacuum level, while phosphorene receives electrons and becomes negatively charged. For Ph/$MoSe_2$ (Ph/WSe_2), the calculated band offsets are given by $\Delta E_v = 0.30$ eV (0.09 eV), the VBO, and $\Delta E_c = 0.11$ eV (0.35 eV), the CBO.

Influences of quasiparticle (QP) corrections on the direct or indirect band gaps of phosphorene within the heterostructures have also been investigated. Besides the gap differences, which indicate large QP openings for both the TMDC and Ph, also the natural band discontinuities in HSE06 $\Delta E_v = 0.30$ eV (0.09 eV) and $\Delta E_c = 0.11$ eV (0.35 eV) vary compared to $\Delta E_v^{\mathrm{DFT}} = 0.31$ eV (0.16 eV), and $\Delta E_c^{\mathrm{DFT}} = 0.21$ eV (0.44 eV) for the Ph/$MoSe_2$ (Ph/WSe_2) heterostructure.

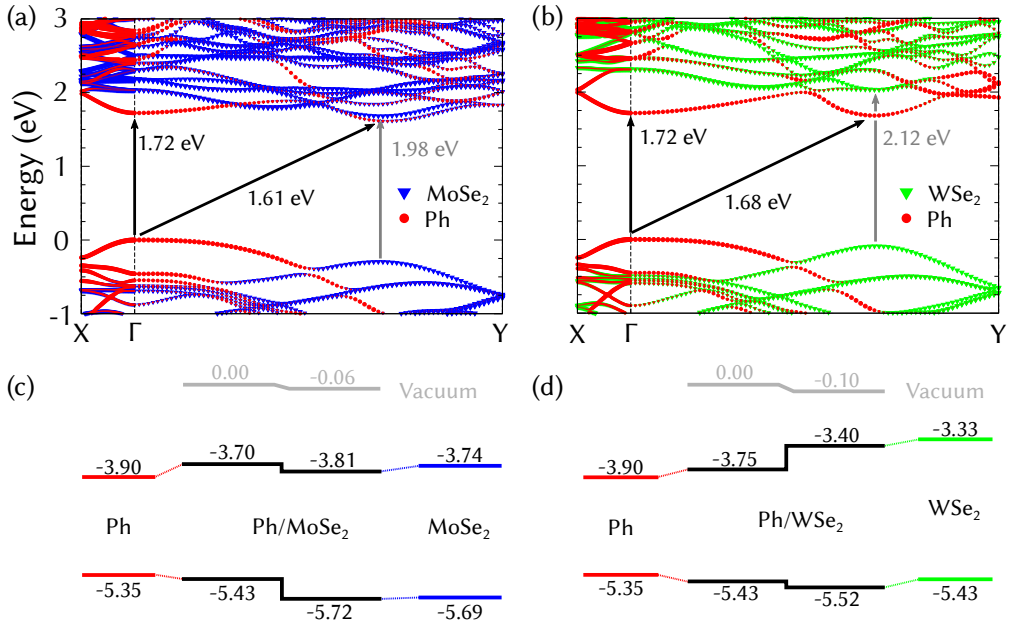

FIGURE 5.2 – Band structures of (a) $Ph/MoSe_2$ and (b) Ph/WSe_2 heterostructures. Contributions from phosphorus atoms are shown with red circles and from the $MoSe_2$ (WSe_2) monolayer are displayed with blue (green) triangles. The size of the symbols specifies the relative contribution from each monolayer to the band formation. The top of the phosphorene valence band is used as energy zero. Band alignments of (c) $Ph/MoSe_2$ and (d) Ph/WSe_2 heterostructures with respect to the vacuum level. Results for freestanding and combined 2D crystals are displayed. All energies are shown in eV.

5.4 Effects of external factors on the heterostructure electronic properties

One way to tune the sensitive electronic properties from phosphorene is through the piezoelectric effect and charge redistribution in the heterointerface, which have been reported both theoretically (HUANG *et al.*, 2015b) and experimentally (RODRIGUES *et al.*, 2015; ZHU *et al.*, 2014) for 2D crystals and other vdW heterostructures. By changing the vdW distances in stacks, it is possible to vary the band gaps from the constituents of the heterostructure due to the modification of the interlayer interaction. We displaced the $MoSe_2$ (WSe_2) layer up to ± 0.4 Å from the equilibrium distance in the warped phosphorene configuration. The corresponding uniaxial pressure along the interface normal direction drastically affects the direct band gap of phosphorene, as summarized in Fig. 5.3 for the $Ph/MoSe_2$ system. The direct band gaps increase when the layers in the heterostructure are put closer, due to more intense interlayer interaction and orbital overlapping. The same physical reason is responsible for shrinking the direct band gap in phosphorene when the two layers have a larger distance than the equilibrium one. Increasing the separation between the two layers leads, asymptotically, to the isolated monolayer case. This is also

observed in the Ph/WSe_2 heterobilayer system . On the other hand, the band gaps of the $MoSe_2$ and WSe_2 layers decrease when the heterobilayer is compressed and increase with the layer separation. This modulation can significantly affect the direct gap of the heterobilayer, which is an interesting feature for optoelectronic sensors and devices, as well as tune band offsets and transport properties by employing mechanical pressure.

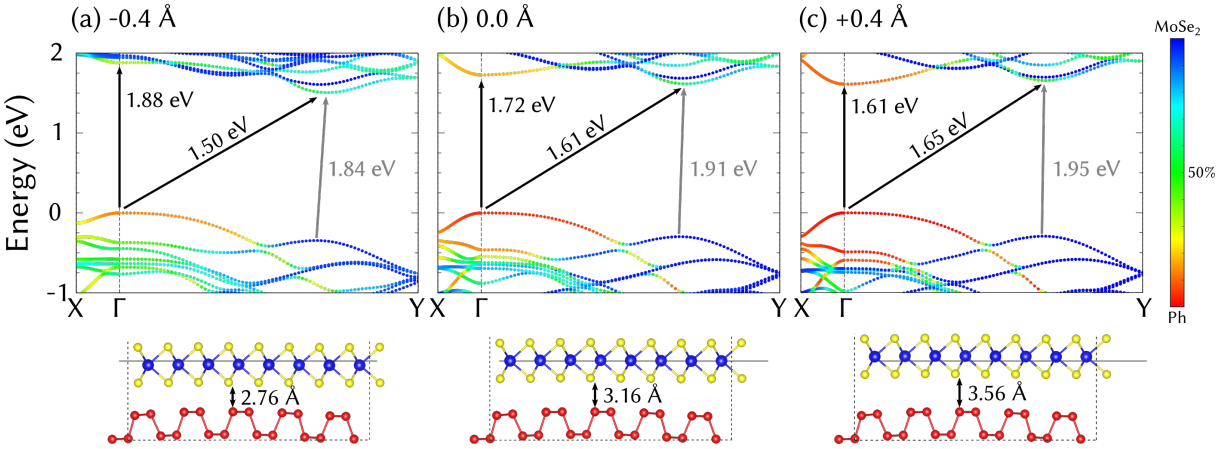

FIGURE 5.3 – Band structures for the Ph/$MoSe_2$ heterobilayer when the vdW gap length is (a) reduced by 0.4 Å, (b) kept constant and (c) increased by 0.4 Å with respect to the equilibrium position. Red and blue markers depict orbital contributions from the phosphorene and $MoSe_2$ layers, respectively. The top of the valence band is taken as reference.

Another possibility to tune band alignments at the Ph/$MoSe_2$ or Ph/WSe_2 interfaces is to apply a vertical external electric field parallel to the stacking direction. This leads not only to a band alignment, but also a heterostructure character depending on the magnitude of the electric field. For both cases, we analyzed small electric fields ranging from -0.4 V/Å to 0.4 V/Å with steps of 0.1 V/Å. Figure 5.4 illustrates how electronic properties of Ph/$MoSe_2$ are influenced by an electric field. When a field is applied in the $-z$ direction, the CBO of the heterostructure increases while reducing the VBO. The charge redistribution imposed by the external electric perturbation leads to a band shift, which can also be interpreted as a bias in the Fermi level on each side of the interface. In the case of the field in the $-z$ direction, this occurs due to the depletion of electrons from Ph by the external electric field, shifting its bands downwards. The opposite behavior of the band offsets happens for $MoSe_2$ and WSe_2. The $MoSe_2$-derived conduction band at about 0.70 Γ–Y moves down in energy while the Ph one shifts toward the vacuum level. As a consequence, a joint band with partial Ph and $MoSe_2$ character appears. For higher field strengths, the Ph/$MoSe_2$ heterostructure returns to a type I character due to this controlled interaction. The crossing point with the vanishing CBO is near -0.1 V/Å, in which the electron wavefunction displays about 50% probability to find an electron when projected onto each layer.

For the Ph/$MoSe_2$ (Ph/WSe_2) system, two transitions between heterostructure types

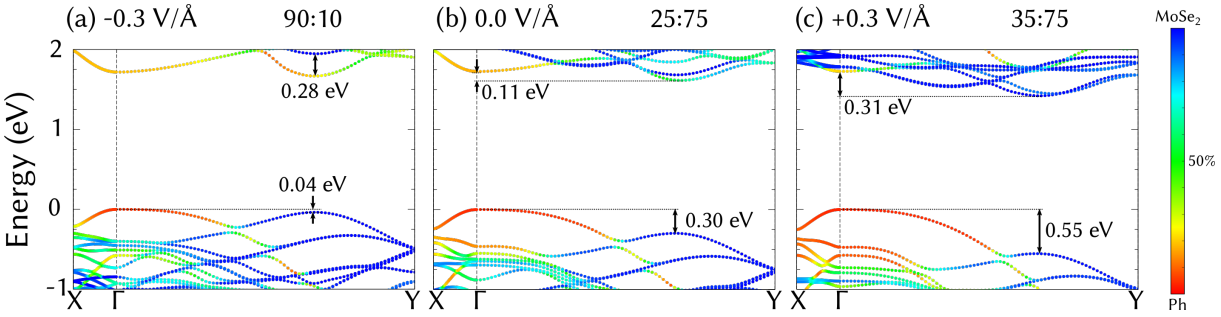

FIGURE 5.4 – Band structures for the Ph/$MoSe_2$ heterobilayer when an electric field of (a) -0.3 V/Å, (b) 0.0 V/Å and (c) +0.3 V/Å is applied in the z direction. The ratios $\Delta E_c/(\Delta E_g)$ and $\Delta E_v/(\Delta E_g)$ are also given. Red and blue markers depict bands formed by orbitals from the phosphorene and $MoSe_2$ layers, respectively. The top of the valence band of each combined system is taken as reference.

are observed for electric fields close to -0.35 V/Å and -0.5 V/Å (-0.1 V/Å and 0.35 V/Å) when considering band offsets defined by direct gaps. Fig. 5.5 also demonstrate the relevance of quasiparticle corrections when calculating band offsets, since DFT calculations do not correctly describe the band hybridization and transitions between heterostructure types under the application of electric fields when examined closely with HSE06 calculations. The former also underestimates the slope of the band offsets with respect to the applied vertical field when compared to the latter. The possibility to control band alignments in heterostructures by vertical fields and enhancement of orbital overlap is fascinating. It paves the way to control carrier injection from one subsystem to another. This broadens possibilities for the construction of field-effect transistors with channels made from atom-thick layers. Moreover, the controlled type II character with electron-hole separation across the heretointerface makes both Ph/$MoSe_2$ and Ph/WSe_2 bilayers suitable for photovoltaic applications.

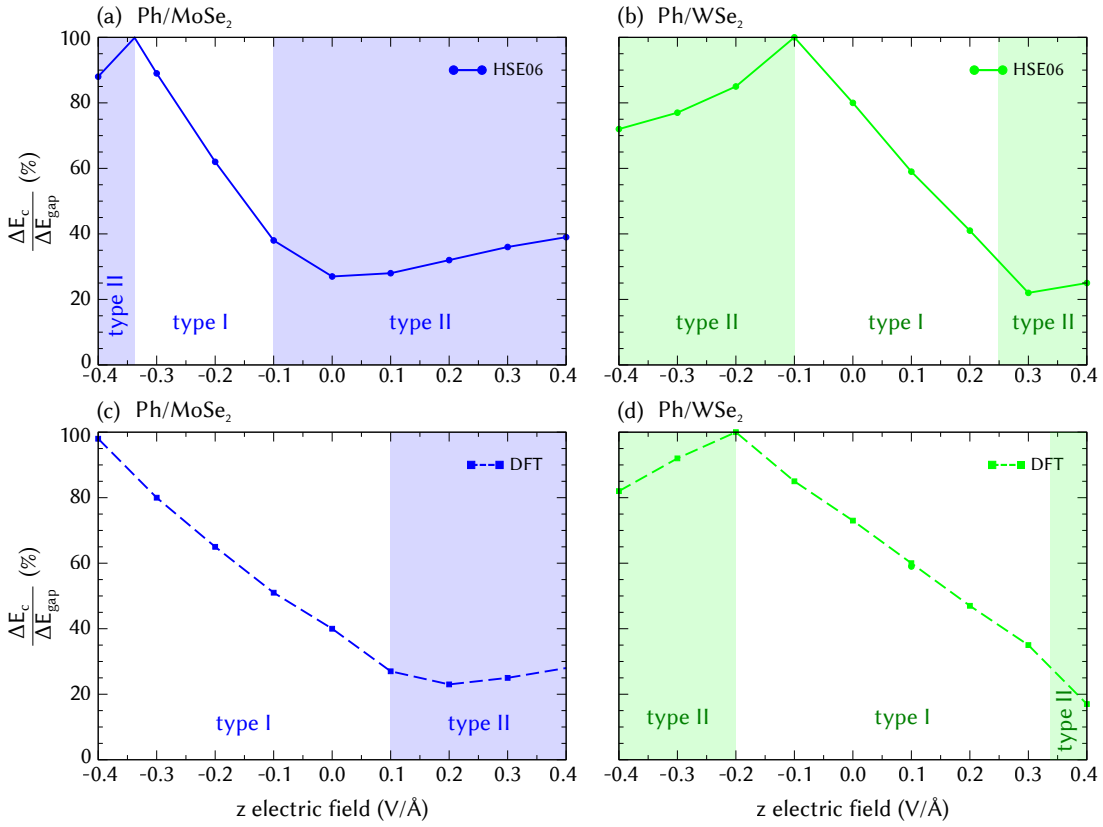

FIGURE 5.5 – Dependence of the heterostructure band offsets $\Delta E_c/\Delta E_{\text{gap}}$ on the vertical electric field applied to Ph/TMDC heterobilayers, which characterizes the heterostructures, for HSE06 calculations of (a) $Ph/MoSe_2$ and (b) Ph/WSe_2. Comparison between DFT calculations for (c) $Ph/MoSe_2$ and (d) Ph/WSe_2 are also shown.

6 Validity of the Anderson rule

6.1 Motivation

The central electronic quantities for the action of a vdW heterojunction between two semiconducting 2D crystals are the band offsets or discontinuities between conduction and valence bands. They influence the transport and charge equilibrium processes of such interfaces (HONG *et al.*, 2014; ZHU *et al.*, 2015; ROY *et al.*, 2016). Nevertheless, the majority of predictions are based on so-called natural band discontinuities between 2D crystals, mainly based on the original electron affinity rule (ANDERSON, 1962; ANDERSON, 1960), i.e., on the vacuum level alignment. The weak interlayer vdW bonding between two atomically thin crystals together leads to a low hybridization of electronic states and the formation of quantum dipoles (TERSOFF, 1984; SCHLAF *et al.*, 1997), as demonstrated in previous chapters.

So far in this work, we have presented a method to predict favorable vdW-bonded stacks of 2D crystals, using it to simulate vdW heterostructures. Several phenomena that arise in these interfaces have been demonstrated, and their effects on band alignments for technological applications should not be overlooked. Therefore, it is necessary to fully understand the limitations of the largely used Anderson rule and the motives behind its failures. In this chapter, we comprehensively analyze band offsets of ten vdW heterostructures based on tin dichalcogenides in order to verify the validity of the Anderson rule. In Sec. 6.2, natural band discontinuities are interpreted and compared with measurements from the literature. Then, in Sec. 6.3 we study the effects of stacking on structural and electronic properties of realistic vdW heterostructures built with these crystals. Band alignments are then discussed in Sec. 6.4. Finally, using the thorough information from this dissertation, the validity and limitations of the Anderson rule are discussed in Sec. 6.5.

6.2 Natural band alignments

We start from the optimized geometries of 11 freestanding 2D crystals optimized according to Chapter 3, with their band discontinuities depicted in Fig. 6.1. The absolute values give the electron affinities A and ionization energies I as in Eq. (3.1). Neglecting interface states, defect levels, charge transfer at a real interface, the electron affinity rule of Anderson (ANDERSON, 1960; ANDERSON, 1962; BECHSTEDT; ENDERLEIN, 1988) can be used to estimate the natural band discontinuities from Eq. (4.3).

Figure 6.1 shows clear chemical trends. With the increase of the anion size from S to Se, both the electron affinities and ionization energies decrease. The only exception appears comparing the conduction band edges of SnS_2 and $SnSe_2$. The quasiparticle gaps E_g of the dichalcogenides vary between 1.1–2.4 eV, indicating semiconducting behavior. The gap values, as well as the I and A values of freestanding 2D crystals, are comparable with those derived from one-shot GW calculations starting from DFT-PBE Kohn-Sham eigenvalues for MS_2 and MSe_2 (M = Zr, Mo, W) (ROUT *et al.*, 2014). The GW gaps are slightly larger than the HSE06 ones because of the somewhat smaller (larger) A (I). However, the trends among the resulting natural band discontinuities from Eq. (4.3) but also their absolute values are rather similar. The observation of comparable band offsets in GW and HSE have been made also for other 2D materials (LIANG *et al.*, 2013). For SnS_2 and $SnSe_2$, the gaps are slightly smaller than values for bulk 3D crystals from similar calculations (SUN *et al.*, 2015) and much closer to the measured gaps of 2.07 and 0.97 eV (DOMINGO *et al.*, 1966). The optical gap of $SnSe_2$ flakes on SiO_2/Si substrate has been measured to be 1.73 eV (ZHOU *et al.*, 2015). The work function of graphene $I = A = 4.33$ eV is in reasonable agreement with other theoretical (ROUT *et al.*, 2014; GIOVANNETTI *et al.*, 2008) and experimental results (OSHIMA; NAGASHIMA, 1997). The electron affinity, ionization energy and fundamental gap reported for bulk SnS_2 and $SnSe_2$ (ROBERTSON, 1979) are also not too far from our computed values.

The variety of band alignments within the Anderson affinity rule demonstrate that the majority of heterostructures based on SnS_2 and $SnSe_2$ are from type II for the chosen crystals in Fig. 6.1 because of their large A and I values, at least for MoS_2, $MoSe_2$, WS_2, and WSe_2. For the $WSe_2/SnSe_2$ heterostructure, the type-II finding is in agreement with photoemission data (ROY *et al.*, 2016). Only the "natural" values $\Delta E_c = 1.78$ eV and $\Delta E_v = -1.06$ eV are somewhat larger. Predictions for the heterojunctions of SnS_2 or $SnSe_2$ with HfS_2, ZrS_2, and $ZrSe_2$ are difficult, since the natural band offsets ΔE_c (SnS_2) and ΔE_v, as well as ΔE_c ($SnSe_2$), are small and may even vary with respect to the sign. For hBN, the situation is difficult since ΔE_v changes the sign with the anion in the dichalcogenide. While hBN/SnS_2 is a type-II system, hBN/$SnSe_2$ clearly shows a type-I character. Most interestingly is the formation of an ohmic contact between graphene and

the tin chalcogenides, since this kind of interface is critical for low-resistance contacts for 2D electronic devices. In summary, natural alignments, however, may be not enough to describe band offsets within vdW heterostructures. Hence, we simulate a series of combinations of 2D crystals in heterojunctions to predict and analyze systematically how does stacking influences the band discontinuities.

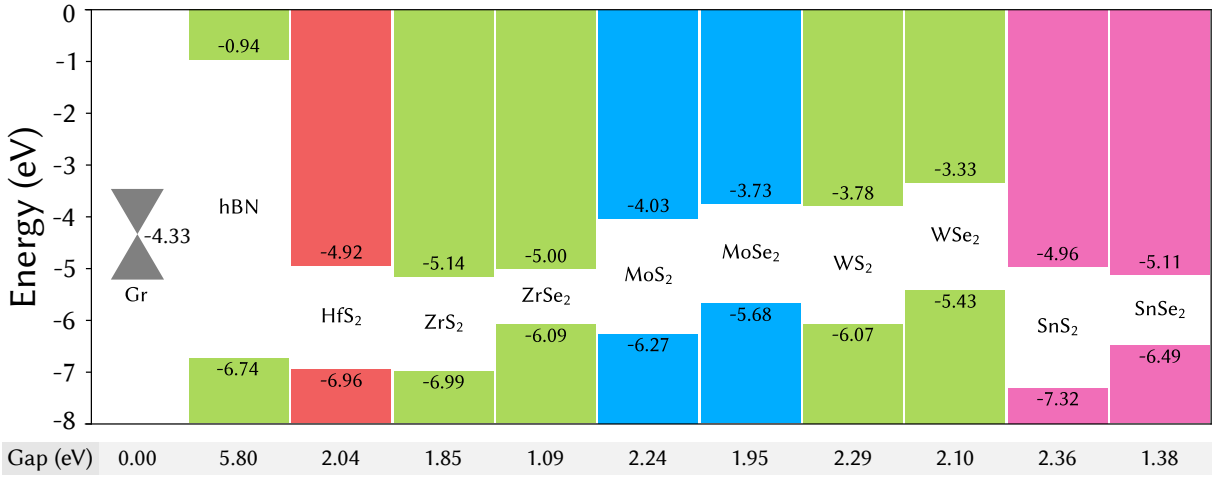

FIGURE 6.1 – Conduction and valence band edges calculated within HSE06 for the 2D crystals under study. The colored bar edges represent the valence band maximum and the conduction band minimum for each monolayer, while the Dirac cone vertex characterizes the Fermi level for graphene. All energies are taken with respect to the vacuum level.

6.3 Real heterostructures

To investigate the formation of interfaces between tin chalcogenides, graphene, boron nitride and the selected TMDCs, we analyze favorable heterostructures. We apply the coincidence lattice method to predict low-energy arrangements of the 2D systems with less than 2% of strain necessary to make an almost commensurate heterobilayer system and number of atoms up to 30 inside the supercell. Thereby, the lateral unit cells, as well as the rotation of the two crystals, are varied. The case of Gr/$SnSe_2$ is an exception, in which the system is forced to be commensurate at an angle of 0° to ensure a reasonable comparison with its SnS_2 counterpart. From then on, each heterostructure is constructed by applying an almost vanishing biaxial strain to the constituents, as given in Tab. 6.1. We keep MoS_2, WS_2, $MoSe_2$ and WSe_2 unstrained due to their stiffness to biaxial strains when compared to SnS_2 and $SnSe_2$ (GUZMAN; STRACHAN, 2014). Graphene is strained to preserve the electronic properties of SnS_2 and $SnSe_2$. In the other cases, the strain is distributed over both monolayers, compressive for one and tensile for the other. This strain distribution gives rise to small variations in electronic properties of the junctions. Then, the interlayer distance between the two layers is varied until an energy minimum is

found. Finally, the system is relaxed to minimize atomic forces. The resulting binding energy E_b of the two layers is calculated as in Eq. 4.1.

For all investigated heterobilayers, stability is found and structural parameters are derived. In the 10 cases listed in Tab. 6.1, the bilayers gain energy due to the interaction between the 2D crystals by vdW bonds, as demonstrated by the magnitude of the binding energy and the interlayer distance. As a rule of thumb, interlayer distances d_{12} around 3 Å are observed. The vdW binding E_b hardly varies around 20 meV/Å^2. For the particular HfS_2/SnS_2, ZrS_2/SnS_2, and $ZrSe_2/SnSe_2$ heterobilayers, the AA stacking is chosen to be simulated due to its enhanced stability and greater binding energy. This has been already shown for interfaces of HfS_2 and ZrS_2 in this work and explains the smaller interlayer distance of these systems within the trend as well. For the other systems, typical vdW distances and binding energies are achieved, as well as a spatial distribution of the bilayer stacking due to the supercell.

TABLE 6.1 – Combinations of 2D crystals with SnS_2 and $SnSe_2$ obtained using the coincidence lattice method. The layer 1/2 column relates the original monolayer unit cell to the supercell used in the heterostructure, denoted according to the Wood notation (WOOD, 1964). The first compound shown in the heterobilayer column is denoted as layer 1. The biaxial strains $\varepsilon_1/\varepsilon_2$ applied to the layers 1/2 to make the system commensurate also characterize the building of the supercell. The relaxed heterobilayer has an interlayer distance of d_{12} and a binding energy of E_b.

Heterobilayer	Layer 1	Layer 2	ε_1 (%)	ε_2 (%)	d_{12} (Å)	E_b (meV/Å^2)
Gr/SnS_2	3×3	2×2	-0.91	0.00	3.38	20.1
HfS_2/SnS_2	1×1	1×1	0.57	-0.56	2.97	21.1
MoS_2/SnS_2	2×2	$(\sqrt{3} \times \sqrt{3})$ R 30.0°	0.00	-0.37	3.32	20.0
WS_2/SnS_2	2×2	$(\sqrt{3} \times \sqrt{3})$ R 30.0°	0.00	0.20	3.34	18.7
ZrS_2/SnS_2	1×1	1×1	0.23	-0.23	2.94	21.3
$Gr/SnSe_2$	3×3	2×2	3.53	0.00	3.46	18.6
$hBN/SnSe_2$	$(\sqrt{7} \times \sqrt{7})$ R 19.1°	$(\sqrt{3} \times \sqrt{3})$ R 30.0°	-0.08	0.08	3.42	18.3
$MoSe_2/SnSe_2$	2×2	$(\sqrt{3} \times \sqrt{3})$ R 30.0°	0.00	-0.50	3.42	19.0
$WSe_2/SnSe_2$	2×2	$(\sqrt{3} \times \sqrt{3})$ R 30.0°	0.00	-0.66	3.44	18.9
$ZrSe_2/SnSe_2$	1×1	1×1	0.84	-0.82	3.00	22.2

For the optimized structural parameters, we calculate electronic properties for all selected heterobilayers. Quasiparticle corrections are approximately included via the hybrid functional HSE06. This not only compensates for a typical underestimation of the DFT band gaps, but describes important hybridization between the layers in a more precise manner, as discussed in Chapter 5. Since band alignments may be quite sensitive to hybridization and interlayer interactions, the methodology adopted ensures an accurate determination of the electronic properties for the heterostructures under investigation. The reference level for the electronic structures is adopted as the energy plateau in the vacuum region of the plane-averaged electrostatic potential, as already used in Fig. 6.1 for

the isolated 2D crystals. However, since a charge transfer may occur, dipole corrections are applied to satisfy the periodic boundary conditions for the supercell in the stacking direction. This leads to the formation of two different vacuum levels, each relative to a side of the interface. Therefore, a step in the vacuum level is adopted for the interface, with height directly related to the magnitude of electrons transferred from one 2D crystal to the other.

Band structures for the heterobilayer systems are displayed in Fig. 6.2, in which the reference is taken as the largest vacuum potential for the interface. The bands are projected onto atomic sites and the contributions of an entire 2D layer is computed. This representation, depicted by markers with different colors in Fig. 6.2, allows us to determine the local energy gap and band discontinuities for each material in the heterostructure. The size of the markers is proportional to the contribution of each crystal to the joint band structure. Since the interface is atomically-thin, the band structure analyzed in the BZ determines the properties of the junction itself.

6.4 Band alignments

To predict the electronic properties of heterostructures for application in electronic and optoelectronic devices, it is indispensable to know the alignment of bands from one material to another. Using the projection technique described earlier and the criterion to determine band edges when hybridization is concerned from Chapter 5, we plot the band diagrams for the heterobilayers. This allows us to understand, from a physical point of view, the relationship between the conduction band minima (CBMs) and valence band maxima (VBMs) from the isolated monolayers and the band offsets of the real interface. Figure 6.3 displays the energy diagrams of the studies vdW interfaces, together with their dipole potential step and isolated band schemes aligned via the vacuum level. Since a commensurability strain has been subject to the 2D crystals, we include the small shifts of the bands of the strained isolated monolayers into the energy diagrams. This allows us to decouple strain effects from the interlayer interactions and restrict our analysis solely to interfacial effects.

To derive chemical trends within the interface, the electronic structure results are displayed in Figs. 6.2 and 6.3. We start with the heterobilayers containing graphene, presenting a metallic behavior. Then we discuss the insulating hBN over $SnSe_2$, while finally discussing the semiconductor heterojunctions with TMDCs.

In the simulated Gr/SnS_2 and Gr/$SnSe_2$ vdW heterostructures, we first observe from Figs. 6.2a,b that the linear band dispersion of graphene is preserved in the heterobilayer system. The Gr Dirac cones, however, appear above the CBM of SnS_2 and $SnSe_2$. Therefore,

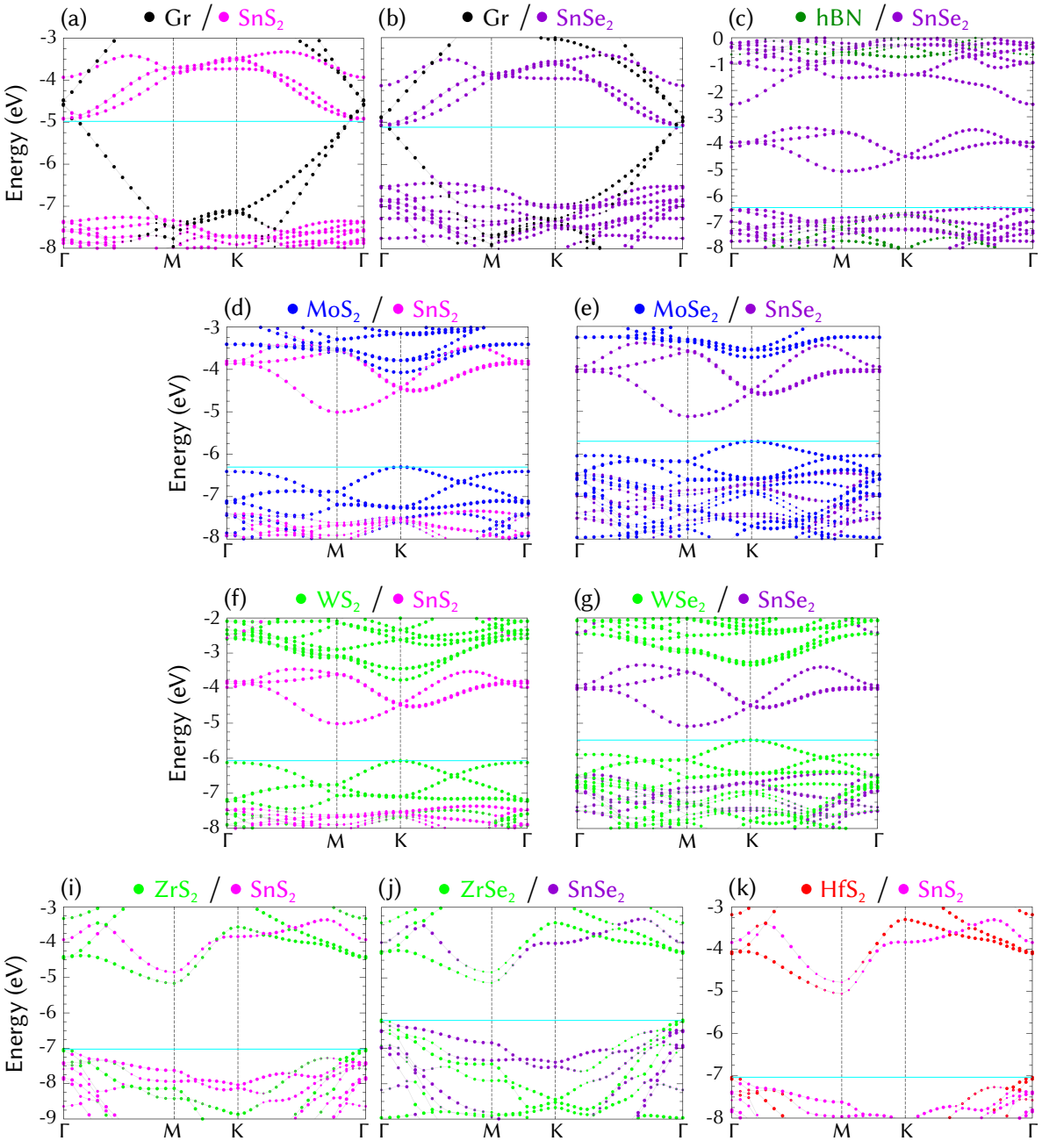

FIGURE 6.2 – Band structures calculated with HSE06 for 10 heterobilayer. The size of the marker represents the relative contribution of each monolayer to the eigenvalue, while its color depicts this contribution projected in the real space. The color representing each 2D crystal in the heterostructure is shown above the band structure. All energies are shown with respect to the highest vacuum level from each heterostructure. The top of the valence band for semiconductor systems (Fermi level for systems with graphene) is shown with an horizontal light blue line.

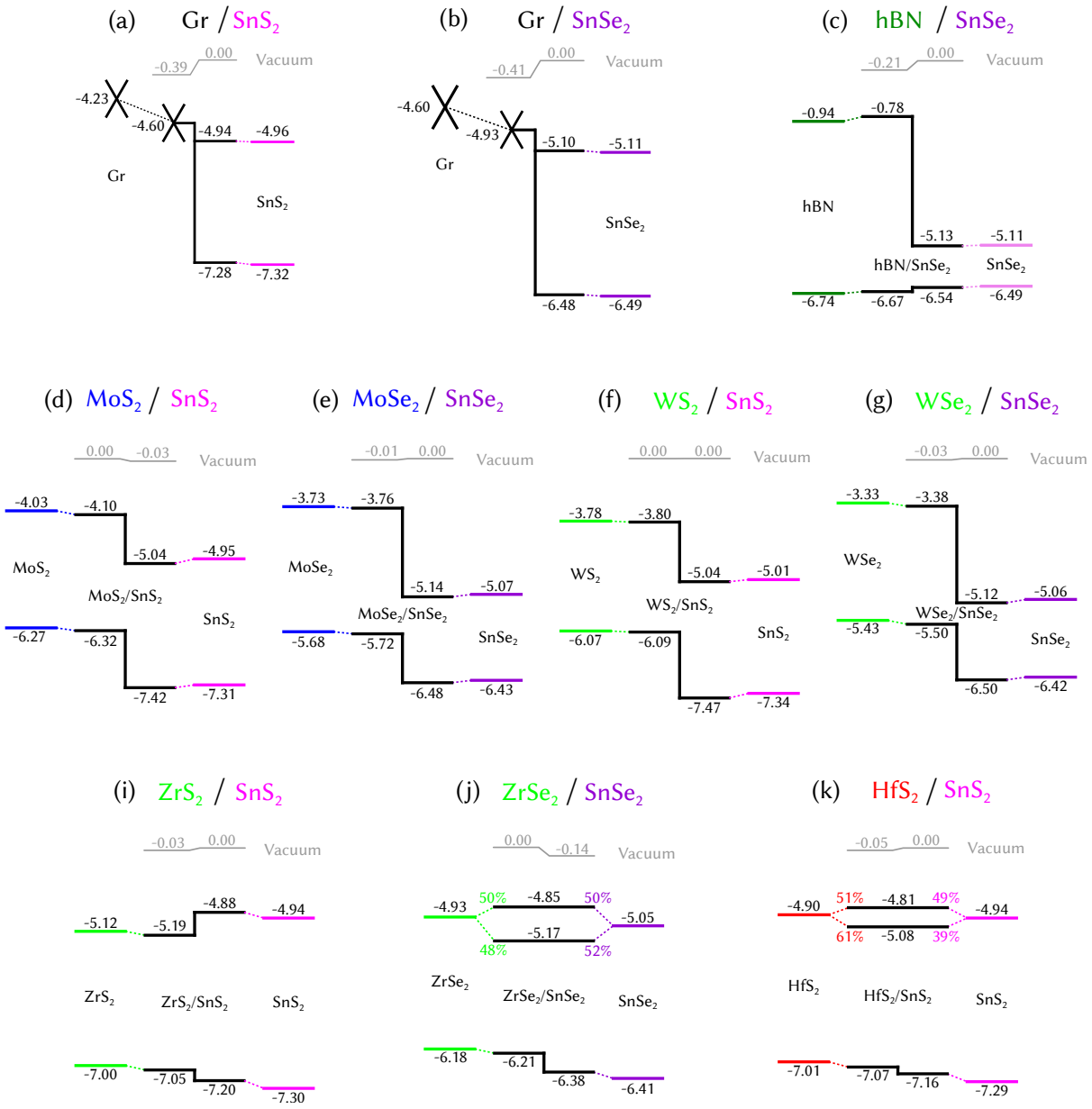

FIGURE 6.3 – Band alignments for each of the 10 heterobilayers under study. The natural band discontinuities for a 2D crystal are represented with colored lines, while the black solid lines at the center of each heterostructure diagram depict the heterojunction band offsets upon contact. The vacuum dipole step is shown in gray, and the colors of each material are specified within the legend of each diagram. In (j) and (k), a hybridization is found within the band edges, and the percentages represent the contribution of each monolayer to the formation of the band minima.

these contacts gives rise to significant charge transfers, creating a dipole potential of the order of 0.4 eV, leading to a vacuum level step and p-doping of the graphene layer. The two effects drastically change the work function of the bilayer, resulting in a metallic behavior. This work function modulation has been observed experimentally and reported in an earlier theoretical work (ROUT *et al.*, 2014). In several devices, the formation of an ohmic contact, such as the one obtained for Gr/SnS_2 or Gr/$SnSe_2$, is preferred. The rectification induced by a Schottky barrier is an impediment to create vdW heterostructure devices with good electric contacts. These interfaces present an alternative for manufacturing Ohmic contacts in 2D semiconductor devices (ALLAIN *et al.*, 2015).

Another 2D crystal used in vdW heterostructure devices is hBN. Its insulating properties make it useful for electronic barriers. By stacking a monolayer hBN on $SnSe_2$, we observe that the electronic properties of both materials are almost preserved, as displayed by the band structures in Fig. 6.2c and the band alignments of the systems in Fig. 6.3c. Only minor changes are observed in the electronic properties of hBN. These modifications of the insulating substrate have been also predicted for other TMDCs/hBN interfaces, as shown in Chapter 4 and experimentally observed for Gr/hBN heterostructures (PAN *et al.*, 2016). Although the hBN/$SnSe_2$ bilayer is a type-I heterostructure, its valence band offset (VBO) is pretty small in both approaches shown in Fig. 6.3c. The large gap discontinuity $\Delta E_g = E_g^{\mathrm{hBN}} - E_g^{\mathrm{SnSe_2}}$ mainly results in a large conduction band offset (CBO), showing that the hole confinement on the $SnSe_2$ side is not very effective. A mutual polarization of the two materials across the interface results in an electrostatic dipole. Its magnitude is compatible with those at interfaces with $MoSe_2$ (see Chapter 4).

SnS_2 and $SnSe_2$ have been largely used for vdW heterostructure devices as underlying substrate layer for the growth of TMDCs (ZHANG *et al.*, 2014). Hence, it is useful to understand the effects underlying the band alignments for these systems. Heterostructures made by MoS_2 and WS_2 with SnS_2 show band offsets very close to their natural ones because of the vanishing interface dipole. The band offsets of $\Delta E_c = 0.9$ or 1.2 eV and $\Delta E_v = -1.1$ or -1.4 eV vary less than 0.1 eV when compared to the ones predicted by the strained monolayer situation. Thus, interfacial coupling almost preserves the local direct band gaps. Nevertheless, the joint electronic properties of the systems may indicate some changes, e.g. indirect band gaps in real space across the interface as for TMDC/SnS_2 systems. Only a small charge transfer occurs on the interface, as indicated by the vanishing vacuum step. These heterostructures are of type II for both MoS_2/SnS_2 and WS_2/SnS_2. The absolute values of ΔE_c and $|\Delta E_v|$ are of the order of 1 eV. This guarantees a spatial charge separation between the electrons and holes on the interface. Experimental results support our findings regarding the heterostructure type and interfacial coupling. Measurements for the stacked few-layer MoS_2, WS_2, and WSe_2 grown on SnS_2 microplates indeed indicate the existence of a weak interaction within the interface, leading even to a

new peak in the photoluminescence spectrum (ZHANG *et al.*, 2014). In the case MoS_2 on SnS_2 this photoluminescence peak has been shown to be from electronic coupling and charge separation of MoS_2 and SnS_2 in the interface, suggesting a type-II heterostructure (LI *et al.*, 2016). This fact is supported by the quenching of the strong excitonic emission peak of freestanding MoS_2.

Heterobilayers of $MoSe_2$ and WSe_2 on $SnSe_2$ are quite similar to the their sulfide analogous (see Figs. 6.3e and g). Small changes are observed in the band alignments but still a vanishing dipole step is found, suggesting weak electroinc polarization between the layers. Both heterostructures are of type-II with band offsets of about $\Delta E_c = 1.4$ or 1.8 eV and $\Delta E_v = -0.8$ or -1.0 eV. However, the extremely small indirect gap between the WSe_2 VBM and the $SnSe_2$ CBM across the heterointerface almost tends to the properties of an broken-gap heterostructure. Experimental results agree with this heterostructure type predictions (ARETOULI *et al.*, 2016; ROY *et al.*, 2016), with some differences in the reported offsets. Small discrepancies are found for the band gaps of WSe_2 and $SnSe_2$ when compared to measurements, ranging between 1.3–1.6 eV and 0.8–1.0 eV, respectively (ARETOULI *et al.*, 2016; ROY *et al.*, 2016). This is due to two facts: (i) the study of approximate quasiparticle gaps in contrast to the optical gaps from spectroscopic measurements and (ii) the dependence of the band gap of these 2D crystals on the number of atomic layers studied. Our results for a CBO of 1.8 eV and a VBO of 1.0 eV for the $WSe_2/SnSe_2$ interface slightly deviate from the experimental values. Excitonic bound states make the optical gaps smaller than the quasiparticle ones due to the strong exciton binding. It has to be eliminated to extract band offsets from optical data. Furthermore, experiments usually report data for few-layer crystals, such as a 3–6 WSe_2 layers (ROY *et al.*, 2016). The thickness influence and the excitonic effects make the results for the studied monolayer case slightly different from the experimental environment explored in the literature (ARETOULI *et al.*, 2016; ROY *et al.*, 2016). These effects explain the smaller CBO of 1.1–1.6 eV and a VBO of 0.8 eV for experimental studies (ARETOULI *et al.*, 2016; ROY *et al.*, 2016) when compared to our results. Nevertheless, the vanishing gap at the $WSe_2/SnSe_2$ interface suggests application in tunneling field-effect transistors (ROY *et al.*, 2016), while $MoSe_2/SnSe_2$ heterobilayers with pronounced type-II character may arouse interest for solar cells and high-performance field-effect transistors (CHEN *et al.*, 2017).

Most interestingly are the HfS_2/SnS_2, ZrS_2/SnS_2 and $ZrSe_2/SnSe_2$ heterostructures when phenomena at the band edges are considered. Due to the small lattice mismatch of these systems ($< 2\%$), it is possible to simulate them as commensurate 1×1 systems by applying a biaxial strain to the crystals. This is not unrealistic though, since similar constraints have been observed experimentally for other vdW heterostructures (WOODS *et al.*, 2014). This kind of commensurability have also been enforced while modulating the

interlayer distance between the 2D crystals (YANKOWITZ *et al.*, 2016).

The three heterojunctions in Figs. 6.3i, j, and k have stacking patterns which lead to different stabilities (KOŚMIDER; FERNÁNDEZ-ROSSIER, 2013). We investigate the most stable of them, namely, the AA stacking. The smallest interlayer distances among the studied systems below 3 Å (see Tab. 6.1) lead to stronger binding energies E_b. This distance decrease is related to stronger interlayer interaction and orbital overlap, which may also tune the electronic properties of the materials, especially their band gaps and band offsets, e.g. by the piezoelectric effect (ZHU *et al.*, 2014; WU *et al.*, 2014). In the $ZrSe_2/SnSe_2$ and HfS_2/SnS_2 heterostructures, for example, the wavefunction overlap drastically changes the lowest conduction bands of the heterojunctions. The almost degenerate states forming the conduction band edges are lifted. According to the molecular orbital theory, the hybridization of the band states of opposite layers in this contact leads to two different energy levels related to bonding and antibonding combinations. Since both layers have a significant contribution to the formation of the joint conduction bands, the definition of a CBO is difficult. In a quantum mechanical sense, the electrons in these bands are delocalized throughout the interface. This fact suggests to derive a zero CBO for these systems. Electrons can freely move in any direction without facing an energy barrier. Theoretical calculations for a $HfSe_2/SnS_2$ heterostructure (SU *et al.*, 2017) are in agreement with our results. On the other hand, in Figs. 6.2i and 6.3i, the ZrS_2/SnS_2 junction exhibits only a weak hybridization when compared to its counterparts in Figs. 6.3j, 6.3k, 6.3j, and 6.3k. The conduction band minimum is formed by 70% of ZrS_2 contributions, which allow a proper definition of a band offset using the quantum mechanical criterion of the highest probability to find an electron on one side of the heterointerface.

While the conduction band is modified by a strong hybridization between the 2D crystals, at least in the latter cases, the uppermost valence band of these three heterosystems are only slightly affected. This is due to the fact that the in-plane orbitals p_x and p_y from the sulfur and selenium anions, responsible for the formation of the valence bands of all five monolayers constituting the three heterointerfaces, remain unaffected upon contact between the layers. By contrast, the conduction bands of ZrS_2, $ZrSe_2$ and HfS_2 are composed mainly by d_{z^2}, d_{xz} and d_{yz} orbitals from the metal atom and p_z orbitals from the anion, and tend to hybridize upon out-of-plane contacts. The conduction bands of SnS_2 and $SnSe_2$ are composed mainly by spherically symmetric s orbitals and, therefore, are hardly influenced by the neighboring layers.

6.5 Anderson rule

Having in mind the importance of band offsets for the construction of heterojunction devices, the formulation of trends regarding band alignments is necessary, in addition to the explicit values given in Fig. 6.3. A heuristic technique commonly applied to semiconductor interfaces is the electron affinity rule, known as the Anderson rule (ANDERSON, 1962; ANDERSON, 1960). According to this rule, the CBO in a semiconductor heterojunction has to be taken directly from the difference between the electron affinities, while the VBO is obtained by the CBO and the quasiparticle (not optical) band gaps of the materials (Eq. (3.3)). In three-dimensional semiconductor heterostructures, stronger mixed covalent-ionic chemical bonding occurs at the interface, which turns the Anderson rule into a rough approximation to describe the junction (BECHSTEDT; ENDERLEIN, 1988). On the other hand, since weak vdW interaction is responsible for the stability of vdW stacks of 2D crystals, the electron affinity rule should be fulfilled for these heterostructures (CHIU *et al.*, 2017). Based on our results, we analyze this expectation in detail below.

We start with cases in which the electron affinity rule in Eq. (4.3) is obviously fulfilled, i.e., where the band alignment in the heterostructure (central part of each panel in Fig. 6.3) can be explained by the "natural" band positions (left and right parts of each panel). The superposition of group VIB metal dichalcogenides, such as MX_2 (M = Mo, W and X = S, Se) with SnX_2, nearly preserves the natural band alignments, with shifts smaller than 0.1 eV in the real heterojunctions. The small dipole potential step in the interface indicates a small charge transfer between the monolayers. The lattice mismatch between the original 1×1 Bravais lattices up to 15% and the difference between their polymorphs (2H for the TMDCs, 1T for the tin dichalcogenides) are impediments to a commensurate 1×1 stacking. The extremely dense coincidence lattices also lead to small interlayer distances. Despite the maximum coincidence and the almost vanishing strain (see Tab. 6.1), interlayer interactions are hindered due to the larger distances between the layers. The chemically dissimilar band compositions leave the monolayers almost intact. Small amounts of charge transfers are found, forming only vanishing dipole steps in the vacuum level (see Fig. 6.3).

When hBN is put into contact with $SnSe_2$, the heterostructure CBO = 4.4 eV differs from the natural CBO (ΔE_c = 4.2 eV) using the electron affinity rule, by almost 0.2 eV. Although no impact is observed on the electronic properties of $SnSe_2$, the insulating hBN layer has modified band edges upon the contact. The large gap of hBN hinders hybridization between the layers, even if its band edge orbital character is mainly p_z on both sides of the interface. The large CBO keeps the $SnSe_2$ CBM almost identical to the one observed in the monolayer case, while the VBM from both crystals suffer from the small VBO. While the electron affinity rule is a reasonable approximation for systems such

as the hBN/$SnSe_2$ one, it does not account for the physical interaction across the interface.

In the case of graphene on SnX_2 the Anderson rule is violated by about 0.4 eV, because of the metallic behavior of the heterostructures. Since the Fermi level of undoped monolayer graphene is above the CBM for both tin dichalcogenides under investigation, a large amount of charge is transferred. In both cases, the p-doping of graphene is responsible for drastic shifts in band alignments.

Also, heterostructures made with group IV-B TMDCs and SnX_2 violate the Anderson rule, even although crystals are only weakly bonded by vdW interaction. One observes a strong hybridization resulting in vanishing CBOs in two cases. This fact seems to be in contrast to the simplicity of the atomic geometries of these heterointerfaces. These heterostructures are made by almost lattice-matched 2D crystals (see Tab. 6.1).Therefore, they can be simulated as 1×1 commensurate systems, leading to small interlayer distances for the AA stacking. This small interlayer distance enhances the conduction state hybridization and dramatically changes the electronic properties of the studied heterosystems. This also happens in the case of phosphorene combined with TMDCs, as shown in Chapter 5.

To validate the above hypothesis, we simulate the same three heterostructures, with exactly the same stacking, but with a larger interlayer distance. Compared to the equilibrium distances d_{12} in Table 6.1, the interlayer distances are increased to values above 3 Å, to 3.32 Å for HfS_2/SnS_2, 3.34 Å for ZrS_2/SnS_2 and 3.41 Å for $ZrSe_2/SnSe_2$. The electronic properties are calculated again using the same methodology. The resulting band alignments are displayed in Fig. 6.4. Comparing these results with those for the most stable arrangements, the vanishing dipole potential steps in Fig. 6.4 and hybridization-induced splittings of the conduction bands for $ZrSe_2/SnSe_2$ show that the electron affinity rule is indeed better fulfilled for the zirconium-based dichalcogenides on top of tin-based dichalcogenides. The increase of the interlayer distance reduces the vdW interaction and hybridization between both layers. The zero CBO in the equilibrium $ZrSe_2/SnSe_2$ heterostructure is replaced by a well-defined CBO for larger interlayer distance in heterostructures. Each 2D crystal hybridizes less with the other layer, leading to 69% $SnSe_2$ contribution to the formation of the joint conduction band. Shifts of about 0.05 eV in the conduction band edges are related to the lift of band degeneracy and the accompanying reduction of hybridization. These effects cannot be ignored in the equilibrium vdW heterostructures, as in the case of HfS_2/SnS_2. Comparing Fig. 6.4c with Fig. 6.3k, we observe that the shifts in the valence band almost vanish when a larger interlayer distance is applied to the system. However, contrary to what is observed in the heterostructures of zirconium and tin dichalcogenides, the CBO does not vanish in the HfS_2/SnS_2 case. The conduction band edges still shift with respect to the situation in the isolated cases. The increase of the interlayer distance, nevertheless, decreases the interlayer interaction. In

the three cases studied, the magnitude of charge transfer is smaller, as evidenced by the almost zero dipole step in the vacuum potential.

The results of our analysis are in agreement with the requirements of the Anderson rule (BECHSTEDT; ENDERLEIN, 1988). For the 2D bilayer heterostructures, we highlighted the three main requirements for the validity of the rule: (i) the orbital overlap should be negligible; (ii) the interlayer interaction should vanish and not be enhanced by external influences, such as electric fields or pressure; and (iii) the natural band positions should be energetically far from each other, so that state hybridization across the interface is supressed upon the contact. In summary, there is a clear tendency that the Anderson rule is fulfilled for vdW bilayer heterostructures with an accuracy of about 0.1 eV. However, in cases where band states localized at opposite sides of the heterointerface are almost energetically degenerate, strong hybridization effects may occur. The accompanying band splittings may violate the rule. This knowledge on vdW bilayer heterostructures may help the band structure engineering for 2D electronic and optoelectronic devices.

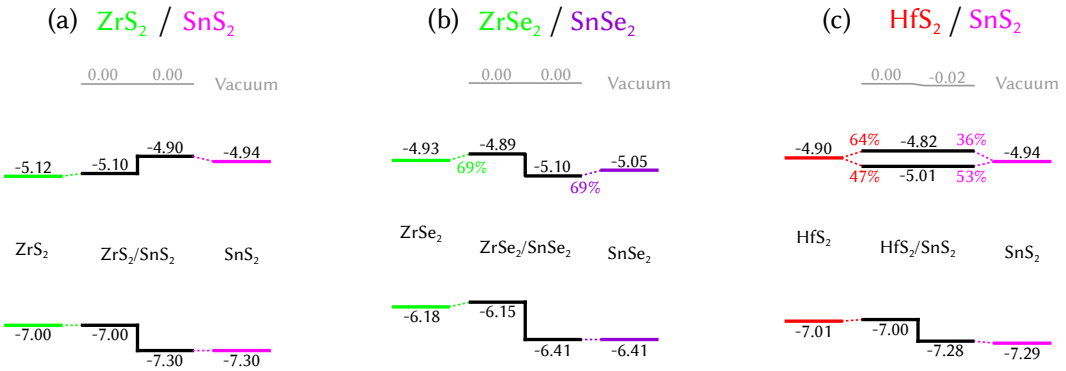

FIGURE 6.4 – Band alignments for (a) ZrS_2/SnS_2, $ZrSe_2/SnSe_2$ and HfS_2/SnS_2 heterostructures with increased interlayer separation (see text). Colored solid lines depict the natural band discontinuities from each monolayer, while the solid black lines represent the band discontinuities upon contact of the systems. The percentage represents the relative contribution of each monolayer to the formation of the band indicated.

7 Conclusions

In summary, the study of vdW heterostructures is challenging both from experimental and theoretical approaches. The incipient environment of this work lies within 2D crystals and their stacks as potential technologies to electronic and optoelectronic devices. We first present a general method for finding small supercells of heterostructures made from 2D materials for studying heterostructures. Based on the idea of the existence of a coincidence lattice in the context of 2D Bravais lattices, we calculate vdW-bonded heterostructures among TMDCs, group-IV dichalcogenides, graphene and hBN using the results of the coincidence lattice method and taking the atoms in account. The method starts from non-primitive unit cells of each sheet crystal in the heterocombination, which correspond to superlattice geometries due to the reconstruction in surface physics and can therefore be described by either the matrix or Wood notation. Within the coincidence lattice method, a system of diophantine equations has to be solved to find optimized lattice geometries of bilayers. The optimization criterion is to find small joint supercells with only an almost vanishing in-plane strain in the two 2D crystals. We validate this approach by comparing its results with those of already studied systems by showing its compatibility with simpler procedures. As an interesting fact, Moiré patterns found experimentally for van der Waals-bonded bilayer systems could be explained by coincidence lattices. We find a large set of interesting coincidence lattices and corresponding supercells using rotations and strain to transform the original combination into a commensurate one. We demonstrate how the small supercells can be applied to simulate real heterojunctions of two sheet crystals.

The coincidence lattice method is then employed to investigate the underlying properties of band alignments on vdW heterostructures. To understand the effects of stacking on structural and electronic properties of the systems, we investigate three heterostructures made from the TMDCs HfS_2, ZrS_2 and MoS_2 using the predicted small supercells, within *ab initio* total energy and electronic structure methods in more detail. For the three explored combinations, we show that the heterostructures are indeed stabilized by vdW interaction. The coincidence lattices filled with the atoms really lead to flat local minima on the total energy surface. The resulting stacking and repulsive effects lead to small influences on the final electronic structure. More importantly, the individual electronic

properties are almost preserved upon contact of the two constituent materials, which certify the promising characteristics from van der Waals heterostructures. Nevertheless, the small interactions between the two 2D crystals in the heterostructure may still change the heterostructure from type II to type I.

Afterwards, we ask whether interlayer twist can affect the electronic properties of the systems. To do so, we expand the application of the method for investigating vdW heterostructures with interlayer twist and supercells requiring low computational efforts. The coincidence lattice method is again employed to simulate $MoSe_2$/hBN heterobilayers with small supercells and taking interlayer twists of 19.1° and 10.9° into account. Small strains were applied to the hBN layer to make the system commensurate, slightly modifying natural band discontinuities. Both systems have almost equal binding energy and are stabilized by weak vdW interactions. Electronic properties are simulated for both rotated systems. The direct band gap of $MoSe_2$ is preserved upon contact with hBN, demonstrating great potential for optoelectronic applications. Electronic structure for hBN suffer from interlayer interactions and orbital overlaps. DOS for both systems are calculated and agree with the analysis of bands in k-space. Charge transfer between the two layers indicate the formation of a dipole in the interface, responsible for shifting band discontinuities and creating a potential barrier between the two layers. Thus, interlayer interactions and twists play a role in slight modulations of the hBN substrate, but electronic properties of $MoSe_2$ are kept unchanged.

Then, effects of interlayer interactions and external perturbations on heterostructure band alignments are made for two heterobilayers of Ph/$MoSe_2$ and Ph/WSe_2. We demonstrate that the systems are stable upon contact and that an interlayer structural bending of 10% is observed in Ph due to vdW interactions. By calculating electronic structures within the approximate quasiparticle picture HSE06, we found an increase of 0.18 eV in the phosphorene band gap and a pronounced orbital overlap, which changes the heterostructure type within Ph/$MoSe_2$ and favors an indirect gap transition in Ph/WSe_2. A definition of band offset for hybridized systems is proposed, according to which band discontinuities are analyzed together within charge transfer and hybridization mechanisms. Significant differences between band offsets calculated with DFT and HSE06 demonstrate the importance of quasiparticle corrections within vdW heterostructures. Electronic properties of the heterobilayers are tuned via application of and external pressure and electric field. We demonstrate the sensitivity of the heterostructures to an external pressure, which modulates band alignments and local direct gaps by up to 0.15 eV for uniaxial vertical strains smaller than 13%. Moreover, electric fields smaller than 0.4 eV/Å can tune the band alignments and control the hybridization between the systems. Whereas strain modulates the band gaps and band offsets in a monotonic way, electric fields along the combined systems can also change the heterostructure character from type I to type II.

The studied heterobilayer systems may be useful for applications in optoelectronics and in FET devices.

Finally, we comprehensively analyze ten different tin dichalcogenides-based vdW heterostructures made from 11 different 2D crystals to validate the Anderson rule for band offsets in heterojunctions. We found atomic geometries for the heterobilayers which minimizes the total energy within the DFT, showing that all systems are stable upon contact and that the interlayer distance between the systems tends to the commensurability of the stack for increased lateral unit cells. Electronic structures are calculated for all heterosystems. From them, band alignments have been derived and compared to their natural band offsets, obtained by vacuum-level alignment and measurements, showing good agreement. Trends among these heterointerfaces have been observed, and their potential applications to device fabrication are emphasized. An Ohmic contact is formed between graphene and SnX_2 (X = S, Se), leading to a p-doping of the graphene layer. The insulating properties of hBN are slightly changed upon contact with $SnSe_2$, while the latter remains almost unchanged. Molybdenum and tungsten dichalcogenides underly small variations, such as band shifts with respect to their isolated monolayer band edges, when stacked over SnX_2, but their band offsets are mostly unaffected. Zirconium dichalcogenides and HfS_2 over SnX_2 interact more strongly with each other, leading to larger shifts in the band offsets between the layers and an important orbital overlap, which gives rise to a zero conduction band offset in the most stable stacking. We also investigated the validity of the electron affinity rule, which works quite accurately for all studied systems except for group-IVB TMDCs on monolayer SnX_2 substrates. In latter cases, we investigated the effect of the interlayer separation, demonstrating that the commensurability of the systems play an important role in the interlayer interaction and state hybridization between the 2D crystals. The increase of the interlayer separation changes the band offsets toward the natural band discontinuities and reduces the hybridization between the layers. We observed an important feature regarding the degeneracy of energy levels, demonstrating its capability to shift the conduction band minimum of the heterobilayer system by the hybridization-induced band splitting.

The knowledge of trends on band alignments and electronic properties of bilayers, as well as the almost validity of the Anderson rule for the studied cases, may guide the way for predicting the action of novel electronic and optoelectronic devices. Together with a theoretical and sound method to analyze vdW heterostructures, this work has major contributions to the scientific community in the area of physics, chemistry and engineering to develop a whole new dimension of materials.

Bibliography

ALLAIN, A. *et al.* Electrical contacts to two-dimensional semiconductors. **Nature Materials**, v. 14, n. 12, p. 1195, 2015. 99

AMET, F. *et al.* Tunneling spectroscopy of graphene-boron-nitride heterostructures. **Physical Review B**, v. 85, n. 7, p. 073405, 2012. 23

ANDERSON, R. Germanium-gallium arsenide heterojunctions [letter to the editor]. **IBM Journal of Research and Development**, IBM, v. 4, n. 3, p. 283–287, 1960. 82, 92, 93, 102

ANDERSON, R. Experiments on Ge-GaAs heterojunctions. **Solid-State Electronics**, Elsevier, v. 5, n. 5, p. 341–351, 1962. 82, 92, 93, 102

ARETOULI, K. E. *et al.* Epitaxial 2D SnSe2/ 2D WSe2 van der Waals Heterostructures. **ACS Applied Materials and Interfaces**, v. 8, n. 35, p. 23222–9, sep 2016. 100

ARGENTERO, G. *et al.* Unraveling the 3D atomic structure of a suspended graphene/hBN van der Waals heterostructure. **Nano Letters**, v. 17, n. 3, p. 1409–1416, 2017. 24

ASHCROFT, N.; MERMIN, N. **Solid State Physics**. South Melbourne: Thomson Learning, 1976. 28, 29, 31, 76

BALANDIN, A. A. *et al.* Superior thermal conductivity of single-layer graphene. **Nano Letters**, v. 8, n. 3, p. 902–907, 2008. 23

BECHSTEDT, F. **Principles of surface physics**. Berlin: Springer, 2003. xv, 47, 56, 58, 61, 69

BECHSTEDT, F. **Many-Body Approach to Electronic Excitations**. Berlin: Springer, 2015. 39, 40, 41, 54

BECHSTEDT, F.; ENDERLEIN, R. **Semiconductor surfaces and interfaces: their atomic and electronic structures**. Berlin: Akademie-Verlag, 1988. (Physical Research). 46, 63, 93, 102, 104

BECKE, A. D. A new mixing of Hartree-Fock and local density-functional theories. **The Journal of Chemical Physics**, v. 98, n. 2, p. 1372–1377, 1993. 41

BJÖRKMAN, T. Testing several recent van der Waals density functionals for layered structures. **The Journal of Chemical Physics**, v. 141, n. 7, p. 074708, 2014. xv, 51, 53, 54, 55

BJÖRKMAN, T. *et al.* van der Waals bonding in layered compounds from advanced density-functional first-principles calculations. **Physical Review Letters**, v. 108, n. 23, p. 235502, 2012. 67, 72, 75, 85

BLÖCHL, P. E. Projector augmented-wave method. **Physical Review B**, v. 50, n. 24, p. 17953, 1994. 43, 44, 45, 51

BRIHUEGA, I. *et al.* Unraveling the intrinsic and robust nature of van Hove singularities in twisted bilayer graphene by scanning tunneling microscopy and theoretical analysis. **Physical Review Letters**, v. 109, n. 19, p. 196802, 2012. x, xv, 59, 60, 61

BUNCH, J. S. *et al.* Impermeable atomic membranes from graphene sheets. **Nano Letters**, v. 8, n. 8, p. 2458–2462, 2008. 23

BUTLER, S. Z. *et al.* Progress, challenges, and opportunities in two-dimensional materials beyond graphene. **ACS Nano**, v. 7, n. 4, p. 2898–2926, 2013. 23

ÇAKIR, D.; SEVIK, C.; PEETERS, F. M. Significant effect of stacking on the electronic and optical properties of few-layer black phosphorus. **Physical Review B**, v. 92, n. 16, p. 165406, 2015. 85

CEPERLEY, D. M.; ALDER, B. Ground state of the electron gas by a stochastic method. **Physical Review Letters**, v. 45, n. 7, p. 566, 1980. 39

CHEN, P. *et al.* Annealing tunes interlayer coupling and optoelectronic property of bilayer SnSe2/MoSe2 heterostructures. **Applied Surface Science**, v. 419, p. 460–464, 2017. 100

CHEN, X. *et al.* High-quality sandwiched black phosphorus heterostructure and its quantum oscillations. **Nature Communications**, v. 6, 2015. 82

CHHOWALLA, M. *et al.* The chemistry of two-dimensional layered transition metal dichalcogenide nanosheets. **Nature Chemistry**, v. 5, n. 4, p. 263–275, 2013. 24

CHIU, M.-H. *et al.* Band alignment of 2D transition metal dichalcogenide heterojunctions. **Advanced Functional Materials**, v. 27, n. 19, 2017. 102

DAS, S. R. *et al.* Low-frequency noise in MoSe2 field effect transistors. **Applied Physics Letters**, v. 106, n. 8, p. 083507, 2015. 24

DEAN, C. R. *et al.* Boron nitride substrates for high-quality graphene electronics. **Nature Nanotechnology**, v. 5, n. 10, p. 722–726, 2010. 23

DENG, Y. *et al.* Black phosphorus-monolayer MoS2 van der Waals heterojunction p-n diode. **ACS Nano**, v. 8, n. 8, p. 8292–8299, 2014. 82

DION, M. *et al.* Van der Waals density functional for general geometries. **Physical Review Letters**, v. 92, n. 24, p. 246401, 2004. 42

DOMINGO, G.; ITOGA, R.; KANNEWURF, C. Fundamental optical absorption in SnS2 and SnSe2. **Physical Review**, v. 143, n. 2, p. 536, 1966. 93

DUFFERWIEL, S. *et al.* Exciton-polaritons in van der Waals heterostructures embedded in tunable microcavities. **Nature Communications**, v. 6, 2015. 24

ELAHI, M. *et al.* Modulation of electronic and mechanical properties of phosphorene through strain. **Physical Review B**, v. 91, n. 11, p. 115412, 2015. 85

ENGEL, E.; DREIZLER, R. M. **Density functional theory: an advanced course**. Berlin: Springer Science & Business Media, 2011. 39, 41, 42

FANG, H. *et al.* Strong interlayer coupling in van der Waals heterostructures built from single-layer chalcogenides. **Proceedings of the National Academy of Sciences**, v. 111, n. 17, p. 6198–6202, 2014. xv, 59, 61, 71

FEI, R.; YANG, L. Strain-engineering the anisotropic electrical conductance of few-layer black phosphorus. **Nano Letters**, v. 14, n. 5, p. 2884–2889, 2014. 24

FIOLHAIS, C.; NOGUEIRA, F.; MARQUES, M. A. **A primer in density functional theory**. Berlin: Springer Science & Business Media, 2003. v. 620. 41

GEIM, A.; GRIGORIEVA, I. Van der Waals heterostructures. **Nature**, v. 499, n. 7459, p. 419–425, 2013. 24

GEIM, A. K.; NOVOSELOV, K. S. The rise of graphene. **Nature Materials**, v. 6, n. 3, p. 183–191, 2007. 23

GIOVANNETTI, G. *et al.* Doping graphene with metal contacts. **Physical Review Letters**, v. 101, n. 2, p. 026803, 2008. 93

GRONVOLD, F.; HARALDSEN, H.; KJEKSHUS, A. On the sulfides, selenides and tellurides of platinum. **Acta Chemica Scandinavica**, v. 14, n. 9, p. 1879–1893, 1960. xv, 55

GUZMAN, D. M.; STRACHAN, A. Role of strain on electronic and mechanical response of semiconducting transition-metal dichalcogenide monolayers: An ab-initio study. **Journal of Applied Physics**, v. 115, n. 24, p. 243701, 2014. 53, 66, 72, 75, 83, 85, 94

HEYD, J.; SCUSERIA, G. E.; ERNZERHOF, M. Hybrid functionals based on a screened coulomb potential. **The Journal of Chemical Physics**, v. 118, n. 18, p. 8207–8215, 2003. 41, 51, 54, 86

HEYD, J.; SCUSERIA, G. E.; ERNZERHOF, M. Erratum: "hybrid functionals based on a screened coulomb potential"[J. Chem. Phys. 118, 8207 (2003)]. **The Journal of Chemical Physics**, v. 124, n. 21, p. 219906, 2006. 51, 54, 86

HOHENBERG, P.; KOHN, W. Inhomogeneous electron gas. **Physical Review**, v. 136, n. 3B, p. B864, 1964. 35

HONG, X. *et al.* Ultrafast charge transfer in atomically thin MoS2/WS2 heterostructures. **Nature Nanotechnology**, v. 9, n. 9, p. 682–686, 2014. 92

HU, T.; HONG, J. Anisotropic effective mass, optical property, and enhanced band gap in BN/Phosphorene/BN heterostructures. **ACS Applied Materials and Interfaces**, v. 7, n. 42, p. 23489–23495, 2015. 86

HUANG, L. *et al.* Electric-field tunable band offsets in black phosphorus and MoS2 van der Waals p-n heterostructure. **Journal of Physical Chemistry Letters**, v. 6, n. 13, p. 2483–2488, 2015. 71

HUANG, L. *et al.* Strain induced piezoelectric effect in black phosphorus and MoS2 van der waals heterostructure. **Scientific Reports**, v. 5, 2015. 71, 86, 88

HUANG, S. *et al.* Probing the interlayer coupling of twisted bilayer MoS2 using photoluminescence spectroscopy. **Nano Letters**, v. 14, n. 10, p. 5500–5508, 2014. xv, 59, 61

JANESKO, B. G.; HENDERSON, T. M.; SCUSERIA, G. E. Screened hybrid density functionals for solid-state chemistry and physics. **Physical Chemistry Chemical Physics**, v. 11, n. 3, p. 443–454, 2009. 41

JARIWALA, D. *et al.* Emerging device applications for semiconducting two-dimensional transition metal dichalcogenides. **ACS Nano**, v. 8, n. 2, p. 1102–1120, 2014. 24

JIN, W. *et al.* Tuning the electronic structure of monolayer graphene/MoS2 van der Waals heterostructures via interlayer twist. **Physical Review B**, v. 92, n. 20, p. 201409, 2015. 69

KANG, J. *et al.* Band offsets and heterostructures of two-dimensional semiconductors. **Applied Physics Letters**, v. 102, n. 1, p. 012111, 2013. 82

KING, S. W. *et al.* Valence and conduction band offsets at amorphous hexagonal boron nitride interfaces with silicon network dielectrics. **Applied Physics Letters**, v. 104, n. 10, p. 102901, 2014. 23

KITTEL, C. **Introduction to Solid State Physics**. Hoboken: Wiley, 2004. 24, 46, 63

KLIMEŠ, J.; BOWLER, D. R.; MICHAELIDES, A. Van der Waals density functionals applied to solids. **Physical Review B**, v. 83, n. 19, p. 195131, 2011. 51, 53, 83

KODA, D. S. *et al.* Coincidence Lattices of 2D Crystals: Heterostructure Predictions and Applications. **The Journal of Physical Chemistry C**, v. 120, n. 20, p. 10895–10908, 2016. 58, 60

KODA, D. S. *et al.* Coincidence Lattices and Interlayer Twist in van der Waals Heterostructures: Application of the Coincidence Lattice Method on hBN/MoSe2 Heterobilayer Systems. **Journal of Electronic Materials**, v. 46, n. 7, p. 3910–3916, 2017.

KODA, D. S. *et al.* Tuning Electronic Properties and Band Alignments of Phosphorene Combined With MoSe2 and WSe2. **The Journal of Physical Chemistry C**, v. 121, n. 7, p. 3862–3869, 2017.

KOHN, W.; SHAM, L. J. Self-consistent equations including exchange and correlation effects. **Physical Review**, v. 140, n. 4A, p. A1133, 1965. 37, 39, 45

KOKOTT, S.; MATTHES, L.; BECHSTEDT, F. Silicene on hydrogen-passivated Si(111) and Ge(111) substrates. **Physica Status Solidi Rapid Research Letters**, v. 7, n. 8, p. 538–541, 2013. ISSN 1862-6270. 83

KOKOTT, S. *et al.* Nonmetallic substrates for growth of silicene: an ab initio prediction. **Journal of Physics: Condensed Matter**, v. 26, n. 18, p. 185002, 2014. 83

KOLMOGOROV, A. N.; CRESPI, V. H. Registry-dependent interlayer potential for graphitic systems. **Physical Review B**, v. 71, n. 23, p. 235415, 2005. 45

KOMSA, H.-P.; KRASHENINNIKOV, A. V. Electronic structures and optical properties of realistic transition metal dichalcogenide heterostructures from first principles. **Physical Review B**, v. 88, n. 8, p. 085318, 2013. xv, 45, 60, 61

KOŚMIDER, K.; FERNÁNDEZ-ROSSIER, J. Electronic properties of the MoS2-WS2 heterojunction. **Physical Review B**, v. 87, n. 7, p. 075451, 2013. 66, 101

KRESSE, G.; FURTHMÜLLER, J. Efficiency of ab-initio total energy calculations for metals and semiconductors using a plane-wave basis set. **Computation Materials Science**, v. 6, p. 15, 1996. 51

KRESSE, G.; FURTHMÜLLER, J. Efficient iterative schemes for ab initio total-energy calculations using a plane-wave basis set. **Physical Review B**, v. 54, p. 11169, 1996. 51

KRESSE, G.; JOUBERT, D. From ultrasoft pseudopotentials to the projector augmented-wave method. **Physical Review B**, v. 59, n. 3, p. 1758, 1999. 43, 51

KROEMER, H. Nobel lecture: Quasielectric fields and band offsets: teaching electrons new tricks. **Review of Modern Physics**, v. 73, n. 3, p. 783, 2001. 24

KUMAR, H. *et al.* Elastic deformations in 2D van der Waals heterostructures and their impact on optoelectronic properties: Predictions from a multiscale computational approach. **Scientific Reports**, v. 5, 2015. 83

LARENTIS, S.; FALLAHAZAD, B.; TUTUC, E. Field-effect transistors and intrinsic mobility in ultra-thin MoSe2 layers. **Applied Physics Letters**, v. 101, n. 22, p. 223104, 2012. 24

LARRSON, P. **VASP on Cray XC-40 Beskow: Preliminary Benchmark Results**. 2015. Disponível em: <https://www.nsc.liu.se/~pla/blog/2015/01/13/vaspstudy-crayxc40/>. Acesso em: 13 jun. 2017. 41

LEE, C. *et al.* Measurement of the elastic properties and intrinsic strength of monolayer graphene. **Science**, v. 321, n. 5887, p. 385–388, 2008. 23

LEE, C.-H. *et al.* Atomically thin p–n junctions with van der waals heterointerfaces. **Nature Nanotechnology**, v. 9, n. 9, p. 676–681, 2014. 24

LEE, C.-H. *et al.* Tungsten ditelluride: a layered semimetal. **Scientific Reports**, v. 5, 2015. 54

LI, B. *et al.* Direct vapor phase growth and optoelectronic application of large band offset SnS2/MoS2 vertical bilayer heterostructures with high lattice mismatch. **Advanced Electronic Materials**, v. 2, n. 11, 2016. 100

LIANG, Y. *et al.* Quasiparticle band-edge energy and band offsets of monolayer of molybdenum and tungsten chalcogenides. **Applied Physics Letters**, v. 103, n. 4, p. 042106, 2013. 93

LIN, Y.-C. *et al.* Atomic mechanism of the semiconducting-to-metallic phase transition in single-layered MoS2. **Nature Nanotechnology**, v. 9, n. 5, p. 391–396, 2014. 54

LIU, H. *et al.* Phosphorene: an unexplored 2D semiconductor with a high hole mobility. **ACS Nano**, v. 8, n. 4, p. 4033–4041, 2014. 24, 63

LUO, H. *et al.* Polytypism, polymorphism, and superconductivity in TaSe2- xTex. **Proceedings of the National Academy of Sciences**, v. 112, n. 11, p. E1174–E1180, 2015. 54

IV-VI2 compounds, general tables crystal structure, lattice parameters, chemical bond of SnS2, SnSe2, SnS(x)Se(2-x). In: MADELUNG, O.; RÖSSLER, U.; SCHULZ, M. (Ed.). **Non-Tetrahedrally Bonded Elements and Binary Compounds I**. Berlin: Springer Berlin Heidelberg, 1998, (Landolt-Börnstein - Group III Condensed Matter, v. 41C). p. 1–3. xv, 55

MAS-BALLESTE, R. *et al.* 2D materials: to graphene and beyond. **Nanoscale**, v. 3, n. 1, p. 20–30, 2011. 23

MAYOROV, A. S. *et al.* Micrometer-scale ballistic transport in encapsulated graphene at room temperature. **Nano Letters**, v. 11, n. 6, p. 2396–2399, 2011. 23

MÖNCH, W. **Electronic properties of semiconductor interfaces**. Berlin: Springer Science & Business Media, 2004. v. 43. 69

MONKHORST, H. J.; PACK, J. D. Special points for Brillouin-zone integrations. **Physical Review B**, v. 13, n. 12, p. 5188, 1976. 51

MOROZOV, S. V. *et al.* Giant intrinsic carrier mobilities in graphene and its bilayer. **Physical Review Letters**, v. 100, n. 1, 2008. 23

NOVOSELOV, K. *et al.* Electric field effect in atomically thin carbon films. **Science**, v. 306, n. 5696, p. 666–669, 2004. 23

OSHIMA, C.; NAGASHIMA, A. Ultra-thin epitaxial films of graphite and hexagonal boron nitride on solid surfaces. **Journal of Physics: Condensed Matter**, v. 9, n. 1, p. 1, 1997. 93

PADILHA, J.; FAZZIO, A.; SILVA, A. J. da. Van der Waals heterostructure of phosphorene and graphene: Tuning the Schottky barrier and doping by electrostatic gating. **Physical Review Letters**, v. 114, n. 6, p. 066803, 2015. 71, 82, 86

PAIER, J. *et al.* Erratum:“screened hybrid density functionals applied to solids”[J. Chem. Phys. 124, 154709 (2006)]. **Journal of Chemical Physics**, v. 125, n. 24, p. 9901, 2006. 86

PAIER, J. *et al.* Screened hybrid density functionals applied to solids. **The Journal of Chemical Physics**, v. 124, n. 15, p. 154709, 2006. 86

PAKDEL, A.; BANDO, Y.; GOLBERG, D. Nano boron nitride flatland. **Chemical Society Reviews**, v. 43, n. 3, p. 934–959, 2014. 23

PAN, M. *et al.* Modification of the electronic properties of hexagonal boron-nitride in bn/graphene vertical heterostructures. **2D Materials**, v. 3, n. 4, p. 045002, 2016. 99

PARR, R. G. **Density functional theory of atoms and molecules**. New York: Springer, 1980. 5–15 p. 32, 40

PENG, X.; WEI, Q.; COPPLE, A. Strain-engineered direct-indirect band gap transition and its mechanism in two-dimensional phosphorene. **Physical Review B**, v. 90, n. 8, p. 085402, 2014. 86

PERDEW, J. P.; BURKE, K.; ERNZERHOF, M. Generalized gradient approximation made simple. **Physical Review Letters**, v. 77, n. 18, p. 3865, 1996. 40, 51

PERDEW, J. P.; BURKE, K.; ERNZERHOF, M. Erratum: Generalized gradient approximation made simple. **Physical Review Letters**, v. 78, p. 1396, 1997. 40, 51

PERDEW, J. P.; ERNZERHOF, M.; BURKE, K. Rationale for mixing exact exchange with density functional approximations. **The Journal of Chemical Physics**, v. 105, n. 22, p. 9982–9985, 1996. 41

PERDEW, J. P.; YUE, W. Accurate and simple density functional for the electronic exchange energy: Generalized gradient approximation. **Physical Review B**, v. 33, n. 12, p. 8800, 1986. 40

PERDEW, J. P.; ZUNGER, A. Self-interaction correction to density-functional approximations for many-electron systems. **Physical Review B**, v. 23, n. 10, p. 5048, 1981. 39

PIZA, A. F. R. d. T. **Mecânica Quântica**. 2. ed. São Paulo: Editora da Universidade de São Paulo, 2009. 27

QIAO, J. *et al.* High-mobility transport anisotropy and linear dichroism in few-layer black phosphorus. **Nature Communications**, v. 5, 2014. 24

QIU, D. Y.; FELIPE, H.; LOUIE, S. G. Optical spectrum of MoS2: many-body effects and diversity of exciton states. **Physical Review Letters**, v. 111, n. 21, p. 216805, 2013. 54

RADISAVLJEVIC, B. *et al.* Single-layer MoS2 transistors. **Nature Nanotechnology**, v. 6, n. 3, p. 147–150, 2011. 24

ROBERTSON, J. Electronic structure of SnS2, SnSe2, CdI2 and PbI2. **Journal of Physics C: Solid State Physics**, v. 12, n. 22, p. 4753, 1979. 93

RODRIGUES, G. da C. *et al.* Strong piezoelectricity in single-layer graphene deposited on SiO2 grating substrates. **Nature Communications**, Nature Publishing Group, v. 6, 2015. 88

ROUT, C. S. *et al.* Enhanced field emission properties of doped graphene nanosheets with layered SnS2. **Applied Physics Letters**, v. 105, n. 4, 2014. 93, 99

ROY, T. *et al.* 2D-2D tunneling field-effect transistors using WSe ₂ /SnSe ₂ heterostructures. **Applied Physics Letters**, v. 108, n. 8, p. 083111, feb 2016. 92, 93, 100

SAKURAI, J. J.; NAPOLITANO, J. **Mecânica Quântica Moderna**. 2. ed. Porto Alegre: Bookman, 2013. 27

SCHLAF, R. *et al.* Experimental determination of quantum dipoles at semiconductor heterojunctions prepared by van der waals epitaxy: Linear correction term for the electron affinity rule. **Journal of Vacuum Science & Technology A: Vacuum, Surfaces, and Films**, v. 15, n. 3, p. 1365–1370, 1997. 82, 92

SCHWIERZ, F. Graphene transistors. **Nature Nanotechnology**, v. 5, n. 7, p. 487–496, 2010. 23

SCHWIERZ, F. Graphene transistors: Status, prospects, and problems. **Proceedings of the IEEE**, v. 101, n. 7, p. 1567–1584, 2013. 23

SHI, Y. *et al.* van der Waals epitaxy of MoS2 layers using graphene as growth templates. **Nano Letters**, v. 12, n. 6, p. 2784–2791, 2012. 65

SINGH, D. J.; NORDSTROM, L. **Planewaves, Pseudopotentials, and the LAPW method**. 2. ed. New York: Springer Science & Business Media, 2006. 43

SLOTMAN, G. *et al.* Effect of structural relaxation on the electronic structure of graphene on hexagonal boron nitride. **Physical Review Letters**, v. 115, n. 18, p. 186801, 2015. 59, 61

SONG, Y. J. *et al.* Influence of defects and band offsets on carrier transport mechanisms in amorphous silicon/crystalline silicon heterojunction solar cells. **Solar Energy Materials and Solar Cells**, v. 64, n. 3, p. 225–240, 2000. 24

SU, S. *et al.* Graphene contacts to a HfSe2/SnS2 heterostructure. **Journal of Chemical Physics**, v. 146, n. 6, 2017. 101

SUN, B.-Z. *et al.* Anisotropic thermoelectric properties of layered compounds in SnX2 (X= S, Se): a promising thermoelectric material. **Physical Chemistry Chemical Physics**, v. 17, n. 44, p. 29844–29853, 2015. 93

TANG, S. *et al.* Precisely aligned graphene grown on hexagonal boron nitride by catalyst free chemical vapor deposition. **Scientific Reports**, v. 3, 2013. 59

TERSOFF, J. Theory of semiconductor heterojunctions: The role of quantum dipoles. **Physical Review B**, v. 30, n. 8, p. 4874, 1984. 82, 92

TONGAY, S. *et al.* Thermally driven crossover from indirect toward direct bandgap in 2D semiconductors: Mose2 versus MoS2. **Nano Letters**, v. 12, n. 11, p. 5576–5580, 2012. 24

TSAI, M.-L. *et al.* Monolayer MoS2 heterojunction solar cells. **ACS Nano**, v. 8, n. 8, p. 8317–8322, 2014. 24

VERBITSKIY, N. *et al.* Atomically precise semiconductor–graphene and hBN interfaces by ge intercalation. **Scientific Reports**, v. 5, 2015. 23

WALTEREIT, P. *et al.* Nitride semiconductors free of electrostatic fields for efficient white light-emitting diodes. **Nature**, v. 406, n. 6798, p. 865, 2000. 24

WANG, D. *et al.* Thermally induced graphene rotation on hexagonal boron nitride. **Physical Review Letters**, v. 116, n. 12, p. 126101, 2016. 59

WANG, G. *et al.* Out-of-plane structural flexibility of phosphorene. **Nanotechnology**, v. 27, n. 5, p. 055701, 2016. 83

WANG, Q. H. *et al.* Electronics and optoelectronics of two-dimensional transition metal dichalcogenides. **Nature Nanotechnology**, v. 7, n. 11, p. 699–712, 2012. 24

WANG, Z.; CHEN, Q.; WANG, J. Electronic structure of twisted bilayers of Graphene/MoS2 and MoS2/MoS2. **The Journal of Physical Chemistry C**, v. 119, n. 9, p. 4752–4758, 2015. xv, 60, 61, 65

WECKBECKER, D. *et al.* Low-energy theory for the graphene twist bilayer. **Physical Review B**, v. 93, n. 3, p. 035452, 2016. 46

WEI, Q.; PENG, X. Superior mechanical flexibility of phosphorene and few-layer black phosphorus. **Applied Physics Letters**, v. 104, n. 25, p. 251915, 2014. 85

WEI, W.; DAI, Y.; HUANG, B. Hybridization effects between silicene/silicene oxides and Ag(111). **Journal of Physical Chemistry C**, v. 120, n. 36, p. 20192–20198, 2016. 82

WEN, S.; PAN, H.; ZHENG, Y. Electronic properties of tin dichalcogenide monolayers and effects of hydrogenation and tension. **Journal of Materials Chemistry C**, v. 3, n. 15, p. 3714–3721, 2015. 54

WITHERS, F. *et al.* WSe2 light-emitting tunneling transistors with enhanced brightness at room temperature. **Nano Letters**, v. 15, n. 12, p. 8223–8228, 2015. 24

WOOD, E. A. Vocabulary of surface crystallography. **Journal of Applied Physics**, v. 35, n. 4, p. 1306–1312, 1964. xv, xvi, 47, 61, 95

WOODS, C. R. *et al.* Commensurate-incommensurate transition in graphene on hexagonal boron nitride. **Nature Physics**, v. 10, n. 6, p. 451–456, 2014. 65, 100

WU, W. *et al.* Piezoelectricity of single-atomic-layer MoS2 for energy conversion and piezotronics. **Nature**, v. 514, n. 7523, p. 470–474, 2014. 101

XU, M. *et al.* Graphene-like two-dimensional materials. **Chemical Reviews**, v. 113, n. 5, p. 3766–3798, 2013. 23

YAN, R. *et al.* Esaki diodes in van der Waals heterojunctions with broken-gap energy band alignment. **Nano Letters**, v. 15, n. 9, p. 5791–5798, 2015. 24

YANKOWITZ, M. *et al.* Pressure-induced commensurate stacking of graphene on boron nitride. **Nature Communications**, v. 7, p. 13168, 2016. 101

YIN, Z. *et al.* Single-layer MoS2 phototransistors. **ACS Nano**, v. 6, n. 1, p. 74–80, 2011. 24

YOU, B. *et al.* Black phosphorene/monolayer transition-metal dichalcogenides as two dimensional van der Waals heterostructures: a first-principles study. **Physical Chemistry Chemical Physics**, v. 18, n. 10, p. 7381–7388, 2016. 86

ZANDE, A. M. van der *et al.* Tailoring the electronic structure in bilayer molybdenum disulfide via interlayer twist. **Nano Letters**, v. 14, n. 7, p. 3869–3875, 2014. 65

ZHANG, X. *et al.* Vertical heterostructures of layered metal chalcogenides by van der waals epitaxy. **Nano Letters**, v. 14, n. 6, p. 3047–3054, 2014. 99, 100

ZHOU, S.; ZHAO, J. Electronic structures of germanene on MoS2: Effect of substrate and molecular adsorption. **Journal of Physical Chemistry C**, v. 120, n. 38, p. 21691–21698, 2016. 82

ZHOU, X. *et al.* Ultrathin SnSe2 flakes grown by chemical vapor deposition for high-performance photodetectors. **Advanced Materials**, v. 27, n. 48, p. 8035–8041, 2015. 93

ZHU, H. *et al.* Observation of piezoelectricity in free-standing monolayer MoS2. **Nature Nanotechnology**, v. 10, n. 2, p. 151–155, 2014. 88, 101

ZHU, X. *et al.* Charge transfer excitons at van der Waals interfaces. **Journal of the American Chemical Society**, v. 137, n. 26, p. 8313–8320, 2015. 92

ZHUANG, H. L.; HENNIG, R. G. Computational search for single-layer transition-metal dichalcogenide photocatalysts. **The Journal of Physical Chemistry C**, v. 117, n. 40, p. 20440–20445, 2013. xv, 54, 55

Annex A - Published works

1. KODA, D. S.; BECHSTEDT, F.; MARQUES, M.; TELES, L. K. Coincidence Lattices of 2D Crystals: Heterostructure Predictions and Applications. **The Journal of Physical Chemistry C**, v. 120, n. 20, p. 10895–10908, 2016.

2. KODA, D. S.; BECHSTEDT, F.; MARQUES, M.; TELES, L. K. Tuning Electronic Properties and Band Alignments of Phosphorene Combined With MoSe2 and WSe2. **The Journal of Physical Chemistry C**, v. 121, n. 7, p. 3862–3869, 2017.

3. KODA, D. S.; BECHSTEDT, F.; MARQUES, M.; TELES, L. K. Coincidence Lattices and Interlayer Twist in van der Waals Heterostructures: Application of the Coincidence Lattice Method on hBN/MoSe2 Heterobilayer Systems. **Journal of Electronic Materials**, v. 46, n. 7, p. 3910–3916, 2017.

4. MATUSALÉM, F.; KODA, D. S.; BECHSTEDT, F.; MARQUES, M.; TELES, L. K. Deposition of topological silicene, germanene and stanene on graphene-covered SiC substrates. **Scientific Reports**, v. 7, n. 1, p. 15700, 2017.

5. GUILHON, I.; KODA, D. S.; MARQUES, M.; TELES, L. K. A new perspective for approximate quasiparticle correction for 2D materials energy gap calculations. **Physical Review B**, in press, 2017.

6. KODA, D. S.; BECHSTEDT, F.; MARQUES, M.; TELES, L. K. Trends on band alignments: Validity of Anderson rule in SnS_2- and $SnSe_2$-based van der Waals heterostrutures. Submitted to **Physical Review B**, 2017.

Annex B - Participations in conferences

1. KODA, D. S.; BECHSTEDT, F.; MARQUES, M.; TELES, L. K. Coincidence Lattices of 2D Crystals for Optimal van der Waals Heterostructures. *Poster presentation.* In: INTERNATIONAL CONFERENCE ON SUPERLATTICES, NANOSTRUCTURES AND NANODEVICES, 19., Hong Kong, 2016. *Winner of the Outstanding Poster Award.*

2. KODA, D. S.; BECHSTEDT, F.; MARQUES, M.; TELES, L. K. Coincidence Lattices and Interlayer Twist for Optimal van der Waals Heterostructures. *Poster presentation.* In: INTERNATIONAL CONFERENCE ON SOLID FILMS AND SURFACES, 18., Chemnitz, 2016.

3. TELES, L. K; BECHSTEDT, F.; MARQUES, M.; GUILHON, I.; KODA, D. S.; PELA, R. R.; MATUSALEM, F. Deposition, alloying and stacking of 2D honeycomb materials: a view from first principles. *Invited talk.* In: INTERNATIONAL CONFERENCE ON SOLID FILMS AND SURFACES, 18., Chemnitz, 2016.

4. KODA, D. S.; BECHSTEDT, F.; MARQUES, M.; TELES, L. K. Band Offsets Engineering for van der Waals Heterostructure Devices. *Contributed talk.* In: APS MARCH MEETING, New Orleans, 2017. **Bulletin of the American Physical Society**, v. 62, 4. ed.

5. KODA, D. S.; BECHSTEDT, F.; MARQUES, M.; TELES, L. K. Interfaces between two atomically thin layers: structure and electronic properties. *Contributed talk.* In: INTERNATIONAL CONFERENCE ON THE FORMATION OF SEMICONDUCTOR INTERFACES, 16., Hannover, 2017.

6. KODA, D. S.; TELES, L. K. Propriedades Eletrônicas de Materiais Bidimensionais e suas Heteroestruturas. *Poster presentation.* In: REUNIÃO ANUAL DA SOCIEDADE BRASILEIRA PARA O PROGRESSO DA CIÊNCIA, 69., Belo Horizonte, 2017.

FOLHA DE REGISTRO DO DOCUMENTO

1. CLASSIFICAÇÃO/TIPO	2. DATA	3. REGISTRO N°	4. N° DE PÁGINAS
DM	26 de dezembro de 2017	DCTA/ITA/DM-121/2017	119

5. TÍTULO E SUBTÍTULO:

Electronic properties and band alignments of 2D crystals and their van der Waals heterostructures.

6. AUTOR(ES):

Daniel Schwalbe Koda

7. INSTITUIÇÃO(ÕES)/ÓRGÃO(S) INTERNO(S)/DIVISÃO(ÕES):

Instituto Tecnológico de Aeronáutica – ITA

8. PALAVRAS-CHAVE SUGERIDAS PELO AUTOR:

Grafeno; Materiais 2D; DFT; Heteroestruturas de van der Waals.

9.PALAVRAS-CHAVE RESULTANTES DE INDEXAÇÃO:

Grafeno; Semicondutores; Estruturas bidimensionais; Teoria de densidade funcional; Heteroestruturas de van der Waals; Física.

10. APRESENTAÇÃO: **(X) Nacional** **( ) Internacional**

ITA, São José dos Campos. Curso de Mestrado. Programa de Pós-Graduação em Física. Área de Física Atômica e Molecular. Orientadora: Profa. Dra. Lara Kühl Teles. Defesa em 19/12/2017. Publicado em 2017.

11. RESUMO:

The scientific advance of two-dimensional (2D) crystals such as graphene and its analogous has developed a new paradigm in solid state physics. By combining their properties in van der Waals heterostructures, not only technological applications are possible, but also the study of physical phenomena in 2D interfaces. Unique properties arise in these stackings by rotation, pressure, hybridization and deformations. Accompanying the growing experiments of these systems, this masters dissertation is theoretically-based to model and simulate the contact of 2D materials in vertical heterostructures by employing quantum mechanics and density functional theory. First of all, a method was developed to predict and perform simulations of 2D stacks, taking into account computational cost and the creation of realistic systems. The technique, named “coincidence lattice method”, is in agreement with other theoretical and experimental data. When applied to a database of 30 2D crystals, more than 700 low-computational cost combinations are found. The application of the method presents a series of interesting systems for ab initio simulations. The first examples are systems with HfS2 , ZrS2 and MoS2 , whose stabilities and electronic properties in the interfacial contact are studied. Then, interlayer twists are imposed to hBN/MoSe2 heterobilayers and their effects in the heterostructure electronic properties are analyzed. Interfaces with phosphorene, MoSe2 and WSe2 are also investigated. Effects of van der Waals interaction on structural and electronic properties of the bilayers are significant, opening the phosphorene gap and leading to hybridization between layers. Band alignments and gaps are modulated by contact, external pressure and electric field. Finally, the validity of the Anderson rule is questioned by a comprehensive analysis of ten bilayer systems. Cases in which this rule fails are analyzed, and a theory is proposed to explain these discrepancies. This work is important in the investigation of band alignments and physical phenomena in 2D interfaces with applications to electronic and optoelectronic devices.

12. GRAU DE SIGILO:

(X) OSTENSIVO **( ) RESERVADO** **( ) SECRETO**